

**PHOTON DOSE CALCULATIONS IN  
INHOMOGENEOUS MEDIA**

by

**BILAL HAIDAR SHAHINE**

B.Sc., American University of Beirut, 1993  
M.Sc., Carleton University, 1995

A THESIS SUBMITTED IN PARTIAL FULFILLMENT OF  
THE REQUIREMENTS FOR THE DEGREE OF

**DOCTOR OF PHILOSOPHY**

in

THE FACULTY OF GRADUATE STUDIES

DEPARTMENT OF PHYSICS AND ASTRONOMY

We accept this thesis as conforming  
to the required standard

THE UNIVERSITY OF BRITISH COLUMBIA

June 2000

© BILAL HAIDAR SHAHINE, 2000

**PHOTON DOSE CALCULATIONS IN  
INHOMOGENEOUS MEDIA**

by

**BILAL HAIDAR SHAHINE**

B.Sc., American University of Beirut, 1993  
M.Sc., Carleton University, 1995

A THESIS SUBMITTED IN PARTIAL FULFILLMENT OF  
THE REQUIREMENTS FOR THE DEGREE OF

**DOCTOR OF PHILOSOPHY**

in

THE FACULTY OF GRADUATE STUDIES

DEPARTMENT OF PHYSICS AND ASTRONOMY

We accept this thesis as conforming  
to the required standard

THE UNIVERSITY OF BRITISH COLUMBIA

June 2000

© BILAL HAIDAR SHAHINE, 2000

In presenting this thesis in partial fulfilment of the requirements for an advanced degree at the University of British Columbia, I agree that the Library shall make it freely available for reference and study. I further agree that permission for extensive copying of this thesis for scholarly purposes may be granted by the head of my department or by his or her representatives. It is understood that copying or publication of this thesis for financial gain shall not be allowed without my written permission.

Department of Physics and Astronomy  
The University of British Columbia  
Vancouver, Canada

Date Sept. 1, 2000

## Abstract

A series of experiments were carried out to simulate air cavities in a polystyrene phantom. Results of experiments were compared to calculations done using three treatment planning systems employing Batho, modified Batho and the equivalent tissue-air-ratio (ETAR) methods for inhomogeneity corrections. The measured interface dose decreased by 55% for a  $5\text{ cm}$  air gap,  $5\times 5\text{ cm}^2$  field size and  $6\text{ MV}$  photons while only a 10% decrease was calculated by these methods. This points to the need for proper inclusion of electronic disequilibrium effects caused by the air cavities. In an attempt to account for electron transport, an inhomogeneity correction factor model is proposed based on separating the primary and scatter photon interaction effect with matter. The primary inhomogeneity correction factor was evaluated in phantoms containing air cavities following Klein-Nishina formalism and detailed electron transport. The Fermi-Eyges theory was adopted to transport recoil electrons based on multiple Coulomb scattering formalism. The scatter inhomogeneity correction factor is proposed as a semi-empirical model based on ratios of tissue-maximum-ratio with scaled effective beam radius. A total correction factor was derived by weighting the primary and scatter components and Monte Carlo simulation was used to verify these results. A calculation code was written and an optimization technique was devised reducing the computa-

tion time to a practical limit while maintaining accuracy. An additional topic on the subject of Monte Carlo treatment planning was discussed. The two Monte Carlo codes EGS4 and GEANT3 have been compared for calculations of photon and electron depth doses in water. Good agreement was seen for radiation beams relevant to radiation therapy. To conclude the comparison, a timing study was performed. GEANT3 was seen to be two times slower than EGS4 in one of its electron transport modes and up to three times faster when using its energy straggling mode of electron transport.

# Contents

<b>Abstract</b>	<b>ii</b>
<b>List of Tables</b>	<b>viii</b>
<b>List of Figures</b>	<b>x</b>
<b>Chapter 1 Background</b>	<b>1</b>
1.1 Introduction . . . . .	1
1.2 Clinical Motivation . . . . .	2
1.3 Radiation Dosimetry . . . . .	2
1.3.1 Physical interactions . . . . .	3
1.4 Production and measurement of Radiation from Linear Accelerators . . . . .	9

1.4.1	Dose measurement . . . . .	11
1.4.2	Dose distribution . . . . .	13
1.5	Treatment planning . . . . .	15
1.5.1	Treatment planning algorithm . . . . .	15
1.6	Radiation dose calculation . . . . .	17
1.6.1	Implicit modelling of particle transport . . . . .	18
1.6.2	Explicit modelling of particle interaction and transport	23
1.7	Thesis objectives and highlights . . . . .	29
<b>Chapter 2</b>	<b>Experiments and treatment planning calculations in phantoms with air cavities</b>	<b>31</b>
2.1	Introduction . . . . .	31
2.2	Experimental Procedure . . . . .	33
2.3	Treatment Planning Systems . . . . .	35
2.4	Results and Discussion . . . . .	36
2.5	Summary . . . . .	44

<b>Chapter 3 Inhomogeneity correction factor incorporating explicit electron transport</b>	<b>46</b>
3.1 Introduction . . . . .	46
3.2 Theory and Methods . . . . .	49
3.2.1 Theory . . . . .	50
3.2.2 Monte Carlo simulation . . . . .	62
3.2.3 Experiments . . . . .	62
3.3 Results and Discussion . . . . .	63
3.3.1 Calculated primary Compton dose compared to Monte Carlo simulation . . . . .	63
3.3.2 Scatter and total inhomogeneity correction factor and comparison with Monte Carlo simulation and experiments	71
3.3.3 Computation time . . . . .	82
3.4 Summary . . . . .	89
<b>Chapter 4 Comparison of GEANT3 and EGS4 Monte Carlo codes for photon and electron beams</b>	<b>92</b>
4.1 Introduction . . . . .	92

4.1.1	Description of electron transport methods . . . . .	93
4.1.2	Parameters for particle tracking in a medium . . . . .	95
4.2	Materials and methods . . . . .	96
4.3	Results and discussion . . . . .	98
4.3.1	Photons . . . . .	98
4.3.2	Electrons . . . . .	101
4.3.3	Calculation time comparison . . . . .	105
4.4	Summary . . . . .	107
<b>Chapter 5</b>	<b>Conclusions and future directions</b>	<b>109</b>
5.1	Summary of work . . . . .	110
5.2	Future directions . . . . .	113
<b>Appendix A</b>		<b>128</b>
<b>Appendix B</b>		<b>131</b>
<b>Appendix C</b>		<b>152</b>

## List of Tables

3.1	The mass attenuation coefficient for polyenergetic photon beams ( $\mu/\rho$ ) is shown evaluated at the average photon energy of spectra. . . . .	55
3.2	Cadplan <i>TMR</i> table for 6 <i>MV</i> beam is shown as a function of depth and field size. The 0x0 <i>cm</i> <sup>2</sup> <i>TMR</i> are extrapolation from higher field size values. . . . .	61
3.3	$\lambda$ is determined as a function of energy for both monoenergetic and polyenergetic beams. . . . .	71
3.4	Computation time for 3D dose distribution for high and low photon energies for different choices of <i>dE</i> . <i>dz</i> was chosen to be 0.2 <i>cm</i> which corresponds to the voxel size dimension. The first column ( <i>N<sub>E</sub></i> ) indicates the number of intervals into which the range of integration is divided. The % error is relative to "small" values of <i>dE</i> in which <i>N<sub>E</sub></i> is set to 2000. . . . .	85

3.5 Best estimate of parameters in Equations 3.31 and 3.32 was derived based on the Least-squares fitting method. . . . .	89
4.1 Calculation time comparison between EGS4 and GEANT3 per event history. ESTEPE and DEEMAX were set to 0.01, ECUT and CUTELE were set to 10 <i>keV</i> , and AE was set to 521 <i>keV</i> while DCUTE is given below. . . . .	107
4.2 Calculation time comparison between EGS4 and GEANT3 per electron event history. STMIN is set as recommended in GEANT3 manual. . . . .	108

## List of Figures

1.1	Differential cross section per unit solid angle per electron as a function of ejected electron angle $\theta$ for 1, 10 and 20 MeV incident photon. . . . .	6
1.2	Relative importance of the three main photon interactions for different atomic numbers of the absorbing material and different initial photon energies (Adapted from [34]). . . . .	8
1.3	A linac head assembly in photon beam mode is shown. Also shown is water phantom used for measurement. (Adapted from [60] with permission) . . . . .	10
1.4	A typical x-ray spectrum for a nominal 18 MV linac. . . . .	11
1.5	The geometry used in the definition of the tissue air ratio (TAR) at a fixed source to axis distance (SAD) with a field size $r$ is shown. (Adapted from [60] with permission) . . . . .	15

1.6 The geometry used in the definition of the tissue maximum ratio (TMR) at a fixed source to axis distance (SAD) with a field size $r$ is shown. $d_{max}$ is the distance from surface to maximum depth. (Adapted from [60] with permission)	16
2.1 The experimental setup used for the three experiments is shown. The black rectangle represents the position of the Markus Chamber.	34
2.2 Comparison of calculated and measured relative dose ( $D_i/D_h$ ) for 6 MV photons is shown for (a) 10x10 cm <sup>2</sup> and (b) 5x5 cm <sup>2</sup> field sizes. Calculations of relative dose using the Batho, modified Batho and ETAR correction methods as implemented on Cadplan lie between 1 and 0.9 while measurements with the Markus chamber show a decrease down to 0.45. Results are normalized to unity at depth 3 cm in the homogeneous polystyrene phantom.	37
2.3 Relative dose calculation is shown as a function of air gap thickness using the Batho correction method as implemented on the Cadplan, GE Target 2 and Xplan treatment planning systems. A 6 MV beam and two field sizes, (a) 10x10 cm <sup>2</sup> and (b) 5x5 cm <sup>2</sup> were used.	39

2.4 Measurements of the relative dose as a function of air gap side for a $5 \times 5 \text{ cm}^2$ field size are shown. Sides were varied from 0x0 (no gap) $\text{cm}^2$ to 20x20 $\text{cm}^2$ for two different air gap thicknesses (3 and 5 $\text{cm}$ ): (a) 6 $MV$ photons and (b) 18 $MV$ photons. The dose was normalized to the dose in homogeneous phantom with 6 $\text{cm}$ ( $t = 3 \text{ cm}$ ) and 8 $\text{cm}$ ( $t = 5 \text{ cm}$ ) of polystyrene over the detector. . . . .	41
2.5 Measurements of the relative dose as a function of depth in a phantom with a 5 $\text{cm}$ air gap thickness for 6 $MV$ photons are shown, (a) for a $10 \times 10 \text{ cm}^2$ field size and (b) for a $5 \times 5 \text{ cm}^2$ field size. The dose was normalized to the dose in the homogeneous phantom at 8 $\text{cm}$ deep. The position of the air gap is indicated by the borded region. . . . .	42
2.6 Measurements of the relative dose as a function of depth in a phantom with a 5 $\text{cm}$ air gap thickness for 18 $MV$ photons are shown, (a) for a $10 \times 10 \text{ cm}^2$ field size and (b) for a $5 \times 5 \text{ cm}^2$ field size. The dose was normalized to the dose in the homogeneous phantom at 8 $\text{cm}$ deep. The position of the air gap is indicated by the borded region. . . . .	43
3.1 The multilayered geometry used in our calculations is shown. . .	50

3.2 The Klein-Nishina differential energy cross sections are shown for 1, 6 and 10 <i>MeV</i> monoenergetic photons and the derived cross sections for the 6 and 10 <i>MV</i> photon spectrum are also included. . . . .	64
3.3 6 MeV photon primary dose calculated with forward directed electrons is compared to dose calculated including electron recoil in all directions. . . . .	65
3.4 Examining delta ray production effect using Monte Carlo simulation compared with analytical calculations. The upper two curves show that $\delta$ -ray production can be accounted for in our analytical calculations by using unrestricted stopping powers. . .	67
3.5 A comparison of primary Compton dose derived from theory and Monte Carlo simulations for a $5 \times 5 \text{ cm}^2$ parallel beam of 6 and 20 <i>MeV</i> monoenergetic photons incident on homogeneous and inhomogeneous phantoms: ( <i>a, c</i> ) variation of absolute dose with depth, ( <i>b, d</i> ) lateral absolute dose profiles at 4 <i>cm</i> depth. The absolute dose shown is per million photons. . . . .	68
3.6 A comparison of primary Compton dose derived from theory and Monte Carlo simulations for a $5 \times 5 \text{ cm}^2$ point source (100 <i>cm</i> SSD) of 6 and 18 <i>MV</i> photon spectra incident on homogeneous and inhomogeneous phantoms: ( <i>a, c</i> ) variation of absolute dose with depth, ( <i>b, d</i> ) lateral absolute dose profiles at 4 <i>cm</i> depth. The absolute dose shown is per million photons. . . . .	70

3.7 Total dose and primary Compton dose as determined by Monte Carlo simulation are shown for 6 MeV 2x2 cm <sup>2</sup> and 10x10 cm <sup>2</sup> irradiation field size in homogeneous and heterogeneous phantoms: (a, c) variation of absolute dose with depth, (b, d) Inhomogeneity Correction Factor derived from the 2 sets of curves of part (a) and (c) respectively. . . . .	73
3.8 Inhomogeneity Correction Factor as determined by Monte Carlo simulation are shown for 6 MV and 18 MV polyenergetic photons: (a, b, c) 6 MV photon beam, and (d, e, f) 18 MV photon beam using field sizes as indicated in the legend. . . . .	74
3.9 Cadplan TMR curves for 6 MV and 18 MV beams. Three field sizes, 0x0 cm <sup>2</sup> , 3x3 cm <sup>2</sup> and 10x10 cm <sup>2</sup> are shown as a function of depth. The 0x0 cm <sup>2</sup> TMRs are extrapolation from higher field size curves. . . . .	76
3.10 Scatter inhomogeneity correction factor ( $ICF_s$ ) and the corresponding effective beam radius derived for 6 MV and 18 MV beams using 5x5 cm <sup>2</sup> and 10x10 cm <sup>2</sup> irradiation field size in inhomogeneous phantoms: (a, c) variation of $ICF_s$ with depth, (b, d) effective beam radius used for calculating the 2 sets of curves of part (a) and (c) respectively. . . . .	77
3.11 Ratio of primary dose to total dose as derived from Monte Carlo simulation using 5x5 cm <sup>2</sup> and 10x10 cm <sup>2</sup> irradiation field size in homogeneous water phantom: (a) 6 MV, (b) 18 MV. . . .	79



4.2 Comparison of EGS4, GEANT3 Monte Carlo codes, and experiment for depth doses in water phantoms irradiated with 6 <i>MV</i> and 18 <i>MV</i> photon beams is shown in (a) and (b) respectively. A point source was used and SSD was set to 100 <i>cm</i> .	100
4.3 The comparison of EGS4, GEANT3 Monte Carlo codes for depth dose calculations in water phantoms irradiated with a range of monoenergetic electrons is shown. The electron transport option used in GEANT3 was the "no fluctuations". Dose was normalized to incident electron fluence.	102
4.4 The comparison of the three electron transport modes implemented in the GEANT3 Monte Carlo code for depth dose calculations in water phantoms is shown. Depth doses for 5 <i>MeV</i> and 20 <i>MeV</i> monoenergetic electrons are shown in (a) and (b) respectively. Dose was normalized to incident electron fluence.	104

## Acknowledgements

In the name of God ...

I am very greateful for having had the opportunity to work under the supervision of Dr. Ellen El-Khatib at UBC. Her guidance and assistance in this entire project have been invaluable. I also thank her for her review of research papers and this thesis. Thanks are also due to Dr. Matthew Al-Ghazi for his co-supervision in the first half of this project.

I wish to express my appreciation to Dr. Dave Axen for the knowledge that he offered me. He taught me the basics of the Monte Carlo method. The patience and time he gave me everytime I dropped by are greatefully acknowledged. Many thanks are due to the rest of the committee members for their constructive input.

I also wish to thank my fellow student Shevonne Ozard for many interesting discussions and helpful suggestions. Her interest in scatter dose and my interest in primary dose brought us together. Her modification of the DOSXYZ usercode for the calculation of primary Compton dose is warmly acknowledged.

Finally, I thank my parents for their patience and continuous encouragement throughout my life. Their prayers are always guiding me. Their faith is what keeps me going.

BILAL HAIDAR SHAHINE

*The University of British Columbia*

*June 2000*

## **Dedication**

*To very special people in my life:*

*my wife Samar and my daughter Batoul*

# **Chapter 1**

## **Background**

### **1.1 Introduction**

In radiation therapy, the aim is to eradicate cancer and preserve normal functioning of human organs. It is therefore important to have a method of accurate dose calculation and delivery [70]. One recommendation is to attain an accuracy for dose delivery of better than 5% [21], but this is difficult to achieve. Modern 3D planning systems operate with an estimated uncertainty in homogeneous material of 3% – 4% [30]. However, larger systematic errors (10% – 50%) may occur in the vicinity of tissue inhomogeneities, for example in the head and neck region [58, 106]. These errors result mainly from the approximations of empirical dose calculation algorithms [38]. The goals of the work described in this thesis are twofold. The first is to quantitatively assess of the accuracy of dose calculations with present treatment planning algorithms with relevance to head and neck radiotherapy. The second is to formulate an analytical model for inhomogeneity correction, providing improvement over

existing models. Additionally, the ultimate goal of radiation treatment planning using the Monte Carlo method will be discussed, and two different codes will be compared for radiation transport calculations.

## 1.2 Clinical Motivation

Head and neck cancers account for about 10 percent of all malignancies. They have a rather good cure rate if they are found early [29]. All three main treatment methods, surgery, radiotherapy and chemotherapy, are used. Tumors can grow in several areas including lip and oral cavity, paranasal sinuses and nasal cavity, salivary glands and the larynx. About a third are in the larynx, and often directly affect speech and other functions. Although most early lesions can be cured by radiotherapy or surgery, radiotherapy is usually the option of choice, because it is possible to preserve a better voice [37]. So our motivation is to come up with more accurate dose calculation algorithm and test it under cases of phantoms containing air cavities.

## 1.3 Radiation Dosimetry

The basic concepts in radiation dosimetry are well described in the literature [4, 34, 50, 56]. A brief description of some pertinent aspects will be presented in this section.

### **1.3.1 Physical interactions**

When an x-ray beam passes through a medium, interactions between photons and matter can take place with the result that energy is transferred to the medium. The initial step in the energy transfer involves the ejection of electrons from the atoms of the medium by the photo-electric or Compton effect. Another method of energy transfer is the production of an electron-positron pair via the interaction of photons with the Coulomb force field of a nucleus or that of an atomic electron (triplet production). These high-speed electrons or positrons transfer their energy by producing ionization (hard collisions) and excitation (soft collisions) of the atoms along their paths. They may also lose energy by radiating bremsstrahlung photons in the Coulomb field of the atom.

#### **A. Photon interactions**

The interactions of photons in matter is governed by five major effects: Rayleigh (coherent) scattering, photoelectric effect, Compton effect, pair production and photonuclear interactions. The Rayleigh scattering interaction consists of an electromagnetic wave passing near a bounded electron and setting it into oscillation. The oscillating electron reradiates the energy at the same frequency. Rayleigh scattering is elastic; there is no energy loss by the photon which is merely redirected through a small angle. Photonuclear interactions occur when a proton or neutron is set in motion by a photon entering and exciting a nucleus. These photonuclear interactions are only significant for photon energies greater than 10 about *MeV*. The other three most important interactions lead to energy deposition at the energies used in radiotherapy and are therefore discussed in detail.

*i) Photoelectric effect*

The photoelectric effect is the most important interaction for low-energy photons. In this process, the entire energy of the photon is transferred to the atomic electron. Electrons ejected (photoelectrons) will acquire a kinetic energy given by

$$KE = h\nu - E_B, \quad (1.1)$$

where  $h\nu$  is the energy of the incident photon and  $E_B$  is the binding energy of the electron.

Photoelectrons are ejected predominately sideways relative to the incident photon direction for low photon energies, because they tend to be emitted in the direction of the photon's electric field. With increasing photon energy they favor the initial direction of the incident photon but are still not perfectly aligned with it. Electron scattering at zero angle to the incident photon direction is forbidden because that is perpendicular to the electric vector ([4]).

*ii) Compton effect*

The incident photon interacts with the outer electrons, the electron is ejected and a photon is scattered. The description of the Compton effect can be most conveniently presented in two aspects: kinematics and cross section. The first relates to the energies and angles of the emerging particles after the interaction occurs, and the second predicts the probability that such an interaction will occur.

By applying the laws of conservation of energy and momentum, kinematic relationships between energy and momentum of the electron and photon

can be derived as

$$E = h\nu_0 \frac{\alpha(1 - \cos \phi)}{1 + \alpha(1 - \cos \phi)} \quad (1.2)$$

$$h\nu' = h\nu_0 \frac{1}{1 + \alpha(1 - \cos \phi)} \quad (1.3)$$

$$\cot \theta = (1 + \alpha) \tan \phi / 2 \quad (1.4)$$

where  $h\nu_0$ ,  $h\nu'$ , and  $E$  are the energies of the incident photon, scattered photon and electron,  $\phi$  is the angle of photon scattering relative to the incident photon direction,  $\theta$  is the recoil angle of the electron, and  $\alpha = h\nu_0/m_0c^2$ , where  $m_0c^2$  is the rest mass energy of the electron [56].

In 1928 Klein and Nishina (KN) applied Dirac's relativistic theory of the electron to the Compton effect to obtain interaction cross sections. The differential cross section for photon scattering at angle  $\phi$ , per unit solid angle and per electron may be written in the form

$$\frac{d_e\sigma}{d\Omega_\phi} = \frac{r_0^2}{2} \left( \frac{h\nu'}{h\nu} \right)^2 \left( \frac{h\nu}{h\nu'} + \frac{h\nu'}{h\nu} - \sin^2 \phi \right). \quad (1.5)$$

Another useful form of the K-N cross section is  $d_e\sigma/d\Omega_\theta$ , the differential cross section for electron scattering at angle  $\theta$ , per unit solid angle and per electron. The relationship between the two differential cross section is

$$\frac{d_e\sigma}{d\Omega_\theta} = \frac{d_e\sigma}{d\Omega_\phi} \cdot \frac{(1 + \alpha)^2(1 - \cos \phi)^2}{\cos^3 \theta} \quad (1.6)$$

and is shown in Figure 1.1.

A third form of the K-N cross section is  $d_e\sigma/dE$ . This is the probability that a single photon will have a Compton interaction in traversing a layer

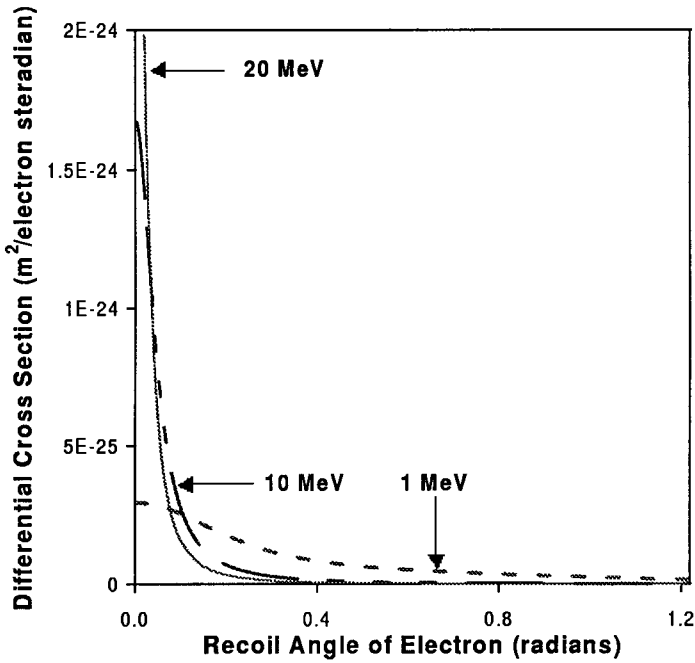


Figure 1.1: Differential cross section per unit solid angle per electron as a function of ejected electron angle  $\theta$  for 1, 10 and 20 MeV incident photon.

containing one  $e/cm^2$ , transferring to that electron a kinetic energy between  $E$  and  $E + dE$ . Thus  $d_e\sigma/dE$  is the energy distribution of the electrons, averaged over all scattering angles  $\theta$ . This relationship is discussed in Chapter 3 where it will form the basis for the calculation method being developed.

### *iii) Pair production*

Pair production is an interaction in which a photon disappears and gives rise to an electron and a positron pair. It can occur in a Coulomb force field near an atomic nucleus when the photon has an energy greater than the sum

of the rest mass of an electron and a positron, ie,  $1.022 \text{ MeV}$ . The electron-positron pair are created in a conversion of energy to mass. The excess incident photon energy greater than the sum of the rest mass energy of the two particles appears as kinetic energy of the positron and electron. The positron eventually annihilates with an electron, producing a pair of photons with energy of  $0.511 \text{ MeV}$  [4].

The relative importance of the photo-electric, Compton, and pair production interactions depend on both the photon energy and the atomic number  $Z$  of the medium. Figure 1.2 indicates the regions of  $Z$  and  $h\nu$  in which each interaction is dominant. The curves are isoeffect where two kinds of interactions are equally probable. As shown in this Figure the photoelectric effect is dominant at the lower photon energies, the Compton effect at medium energies, and pair production at the higher energies.

## B. Electron interactions

In matter, electrons lose energy predominantly by ionization and excitation. This results in deposition of energy or absorbed dose in the medium. Ionization occurs if the energy transferred to orbital electrons is greater than their binding energy, otherwise electrons are displaced from their stable position and then return to it causing excitation. In the process of ionization, some of the "freed" electrons receive sufficient energy to produce ionization tracks of their own. These are often called  $\delta - rays$ .

The electron may also interact with the Coulomb field of a nucleus and be decelerated so rapidly that a part of its energy is lost as bremsstrahlung (breaking radiation). The rate of energy loss due to bremsstrahlung increases

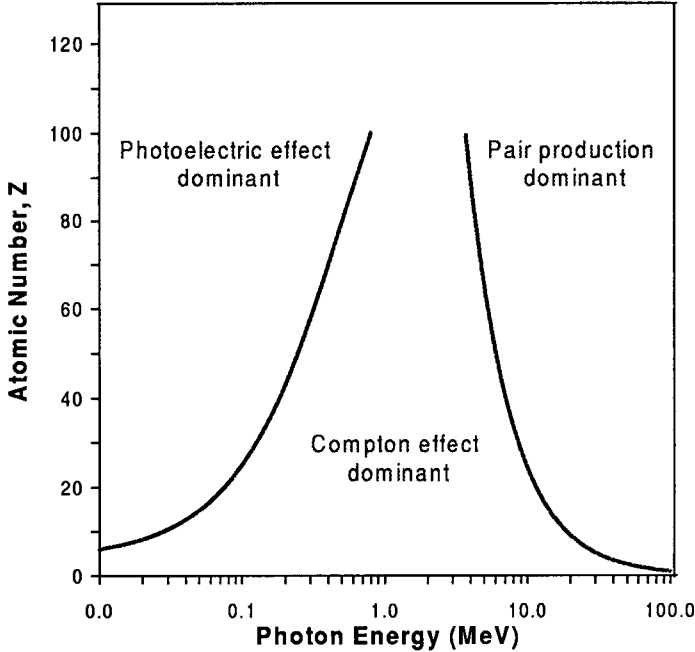


Figure 1.2: Relative importance of the three main photon interactions for different atomic numbers of the absorbing material and different initial photon energies (Adapted from [34]).

with electron energy and the atomic number of the medium.

An important concept which gives the rate of energy loss per unit of path length by a charged particle in a medium is the medium stopping power. Based on the main energy loss mechanisms, stopping power may be subdivided into an unrestricted "collision stopping power" and a "radiative stopping power". Finally the total stopping power is the sum of the collision and radiative contributions and is given as

$$S_{tot} = \frac{dE}{dx} = \left( \frac{dE}{dx} \right)_c + \left( \frac{dE}{dx} \right)_r, \quad (1.7)$$

where  $E$  is the electron energy and  $x$  is the pathlength.

In the description of the electron-electron collision, the outgoing electron with the smaller kinetic energy is defined as a delta ray ( $\delta$  – ray). Therefore, the energy of the  $\delta$  – ray is always smaller than half the energy of the incident electron. In many situations only those energy losses which lead to  $\delta$  – rays with energy below a cut-off energy,  $\Delta$ , are of interest. The restricted stopping power,  $L_\Delta$ , includes only such energy losses. Therefore, the restricted stopping power is smaller than the unrestricted collision stopping power and their ratio as a function of electron energy is given by ICRU35 [79].

## 1.4 Production and measurement of Radiation from Linear Accelerators

A linear accelerator (linac) is a device that uses high-frequency electromagnetic waves to accelerate charged particles (usually electrons) through evacuated waveguides. The high-energy electron beam itself can be used for treating superficial tumours, or it can be made to strike a target to produce x-rays which are used for treating deep-seated tumours [51]. To produce a uniform radiation beam in the plane of the patient several devices are required as illustrated in Figure 1.3 for the photon treatment mode. The x-ray beam emerging from the target is collimated by a fixed primary collimator. A typical x-ray spectrum is shown in Figure 1.4. Since for megavoltage energies the x-ray intensity emerging from the target is peaked in the forward direction a flattening filter is used to make the beam intensity uniform across the field.

Transmission ion chambers monitor beam output, flatness, and symmetry. A light and mirror produce a visible field corresponding to the position and size of the radiation beam and the secondary upper and lower orthogonal movable collimators shape the radiation beam into various rectangular sizes.

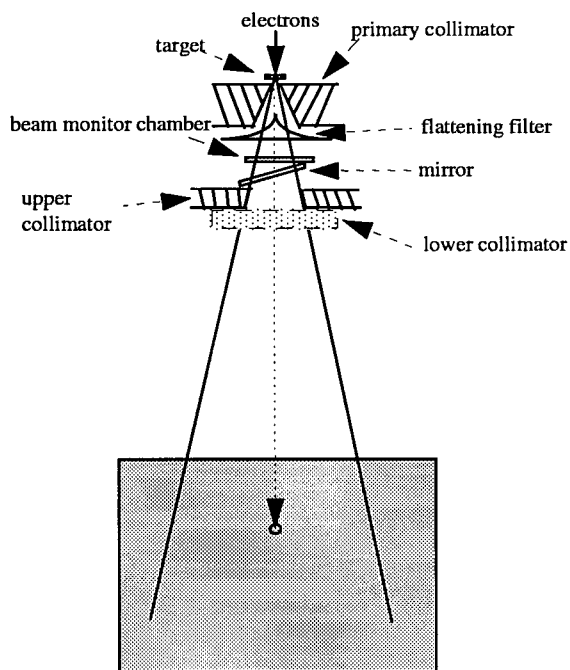


Figure 1.3: A linac head assembly in photon beam mode is shown. Also shown is water phantom used for measurement. (Adapted from [60] with permission)

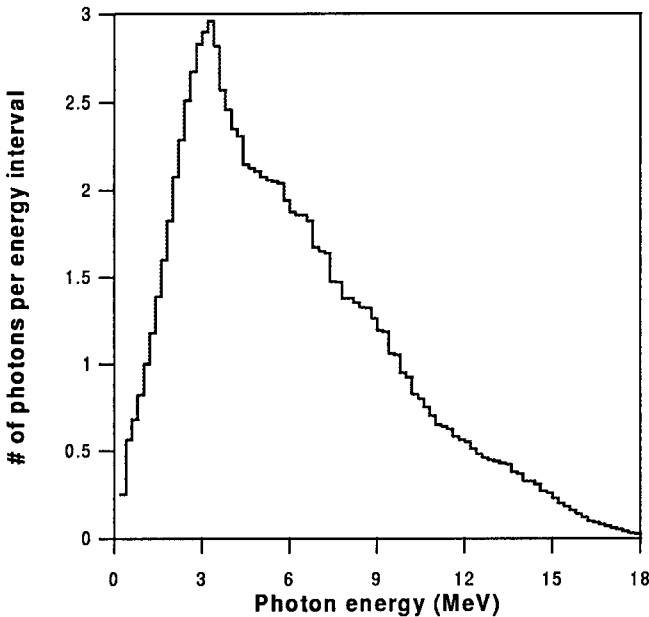


Figure 1.4: A typical x-ray spectrum for a nominal 18 MV linac.

#### 1.4.1 Dose measurement

Ionization chambers are one of the devices used for measuring radiation dose. There are many varieties of ion chambers used in clinical practice, but generally they are all composed of a gas-filled chamber containing electrodes that collect the ions produced in the gas by the ionizing radiation. These electrodes are connected to an electrometer which can be used to measure the charge or current. For air-filled chambers, the absorbed dose (energy deposited per unit mass) to air is given by

$$D_{air} = \frac{W}{e} \cdot \frac{Q}{m}, \quad (1.8)$$

where  $Q$  is the total charge of ions of one sign,  $m$  is the mass of air from which the ions are collected and  $\frac{W}{e}$  is the average energy required in air to produce a unit charge. For dry air,  $\frac{W}{e}$  is equal to  $33.97 \text{ J/C}$ .

The dose to water can then be calculated from the dose to air using cavity theory. For a given spectrum of photon energies the generated electron fluence can be determined as shown in section 1.3. When the electron fluence spectrum is known at the wall surrounding the gas, and the cavity is assumed to be so small that it does not affect the electron spectrum, the gas cavity will witness the same electron fluence as does the wall. Then, the ratio of the dose absorbed by water to that absorbed by the air in the ion chamber is equivalent to the ratio of the stopping powers for the two media. This statement summarized the Bragg-Gray cavity theory which can be represented as

$$\frac{D_{\text{water}}}{D_{\text{air}}} = \left( \frac{S}{\rho} \right)_{\text{air}}^{\text{water}}. \quad (1.9)$$

In practice, when the ion chamber is introduced into a phantom for dose measurements it perturbs the dose deposition. Correction factors are applied to account for three effects, 1) the ion collection efficiency of the chamber, 2) the change in photon fluence resulting from the replacement of the medium by the ion chamber wall and cavity, and 3) the differences in the composition of the medium and the chamber wall.

### **1.4.2 Dose distribution**

Basic dose distribution data are usually measured in a water phantom. Water closely approximates the radiation absorption and scattering properties of the human body at megavoltage energies. An essential step in the data preparation is to establish depth dose variation along the central axis of the beam. A number of quantities have been defined for this purpose, mainly percentage depth dose (PDD), tissue-air ratios (TAR), and tissue maximum ratios (TMR). These quantities are measured in a water phantom using an ion chamber.

#### **A. Percentage depth dose**

The PDD is the central axis dose distribution normalized to the maximum dose with the distance of the source to phantom surface kept constant at 100 *cm*. Important features of the depth dose is the initial buildup which becomes more pronounced as the energy is increased. The region between the surface and the point of maximum dose is called the buildup region.

The dose buildup may be explained as follows: as photons are incident on the phantom, electrons are ejected from the surface and the subsequent layers. These electrons may deposit a substantial portion of their energy some distance away the point of their creation. This results in an increase of electron fluence with depth up to a maximum level. This level of electron fluence would be maintained if the photon fluence were constant. At this point a charged particle equilibrium is achieved for a small volume  $v$  where each charged particle of a given type and energy leaving  $v$  is replaced by an identical particle of the same energy entering.

Beyond the depth of dose maximum the photon energy fluence continuously decreases with depth due to removal of photons from the beam and hence the production of electrons also decreases. The net effect is that beyond a certain depth the dose decreases with depth and only transient charged particle equilibrium exists in the descending portion of the depth dose curve.

### **B. Tissue-air ratio and tissue-maximum ratio**

TAR is defined as the ratio of the dose ( $D(d, r)$ ) at a given point in the phantom to the dose in free space ( $D_{air}(r)$ ) at the same point (Figure 1.5). TAR depends on depth  $d$  and field size  $r$  at that depth. The distance from radiation source to point of measurement (SAD) is kept constant and the field size  $r$  is defined at SAD. Hence,

$$TAR(d, r) = \frac{D(d, r)}{D_{air}(r)}, \quad (1.10)$$

which is independent of SAD.

Another similar quantity is the tissue-maximum ratio which is defined as the ratio of the dose at a given point in the phantom ( $D(d, r)$ ) to the maximum dose  $D(d_{max}, r)$  in the phantom keeping the distance from the source to the measurement point constant and varying the water level above the measurement point. The geometry adopted for measuring TMR is shown in Figure (1.6).

For megavoltage beam energies, measurements of *TARs* are not practical since they involve measurements of dose in air. This is mainly because it would be necessary to supply the dosimeter with such a large buildup cap that it would not be fully irradiated by small area beams [50].

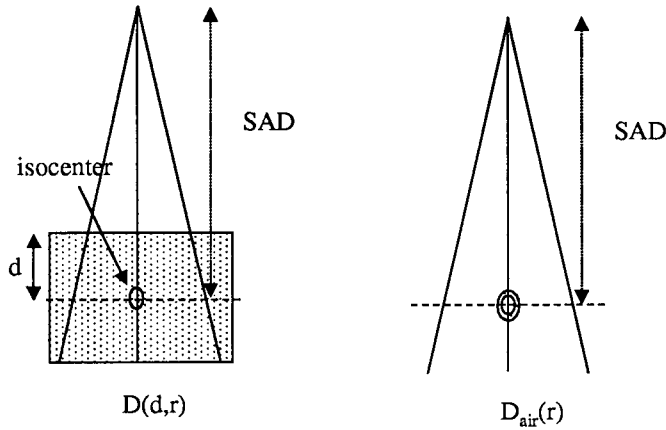


Figure 1.5: The geometry used in the definition of the tissue air ratio (TAR) at a fixed source to axis distance (SAD) with a field size  $r$  is shown. (Adapted from [60] with permission)

## 1.5 Treatment planning

Computerized treatment planning is a numerical calculation procedure in which absorbed dose distribution within a patient is predicted from models based on phantom measurements. These models would incorporate modifications of dose distributions measured in a water phantom to account for beam modifiers (irregularly shaped fields), surface contours, and tissue heterogeneities [56].

### 1.5.1 Treatment planning algorithm

The treatment planning algorithms investigated in this thesis include an in-house algorithm and a commercial one that is available in many centres.

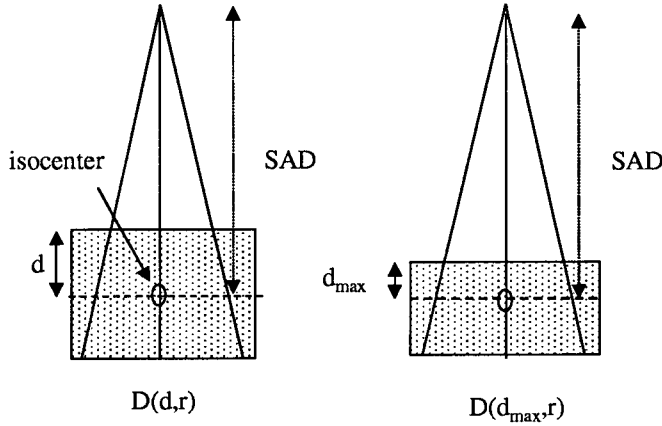


Figure 1.6: The geometry used in the definition of the tissue maximum ratio (TMR) at a fixed source to axis distance (SAD) with a field size  $r$  is shown.  $d_{max}$  is the distance from surface to maximum depth. (Adapted from [60] with permission)

### A. An in-house treatment planning algorithm

Our in-house treatment planning program is based on the work of Kornelsen and Young for the representation of depth dose data [59]. The absorbed dose is derived from the tissue maximum ratio (TMR) which is represented by a parametrized exponential function. The values of the parameters are determined empirically for a number of radiation beams and field size. These data curves are stored in the system and a numerical interpolation is employed for finding values in between. For tissue inhomogeneity correction, the Batho correction method is implemented [6].

### A. Commercial treatment planning algorithm

The Cadplan treatment planning system (Varian Oncology Systems, Varian/Dosetek, Zug, Switzerland) has two calculation models to calculate

the dose distribution in a patient. These are, 1) the photon beam reconstruction model which uses measured depth dose and profile curves and 2) an interpolation procedure is engaged to calculate the dose distribution in a water-equivalent material. Then, to apply the dose distribution to human anatomy the patient model handles the patient outline and inhomogeneities. The inhomogeneity correction factors are calculated by using either the generalized Batho [6, 94, 102], or modified Batho [97] or the "equivalent tissue-air ratio" (*ETAR*) method. The dose value calculated in a water-equivalent material is then multiplied by the inhomogeneity correction factor.

## 1.6 Radiation dose calculation

Most clinical photon dose calculation algorithms assume electron equilibrium in the patient. This approximation neglects electron transport, and does not take into account the range travelled by secondary electrons set in motion by photons. In fact, the path of electrons is greatly altered which results in appreciable errors in areas near the beam edges or near inhomogeneities in high-energy photon beams [110].

Inhomogeneity corrections are more complex than other patient corrections. The presence of tissue inhomogeneities may lead to two general effects, 1) changes in the absorption of the primary beam and the associated pattern of scattered photons and 2) changes in the secondary electron fluence [56]. To deal with these perturbations several methods have been devised and adopted which can be grouped into two categories: (I) implicit modelling of particle transport and (II) explicit modelling of particle interaction and transport.

### 1.6.1 Implicit modelling of particle transport

Implicit modelling of particle transport through scaling operations stem from the existence of two important theorems first presented by Fano [36] and O'Connor [78]. These theorems formulate density-scaling of data for water to "water-like media" with arbitrary densities.

Fano's theorem states that when an object of varying density but constant atomic composition is present in a radiation field having a constant fluence of primary particles (photons), then the fluence of secondary particles (electrons) is also constant and independent of the density variations [36]. The main assumption in Fano's theorem is that the interaction cross sections per unit mass are independent of the density of a medium of identical atomic composition. Hence, in order to apply Fano's theorem to external photon beams, one must assume that primary photon attenuation, density variations, and the production of scattered photons can be neglected [2].

Fano's theorem applies to situations of charged particle equilibrium. The density scaling theorem presented by O'Connor provides a bridge for the dose in two media of different density but equal atomic composition both irradiated by the same external beam. This theorem states that the ratio of the scattered photon fluence to that of primary photon fluence is constant in the two media provided all geometric distances, including field sizes, are scaled inversely with density [78].

It is often practical to describe the influence of a tissue heterogeneity as a perturbation of the dose to a homogeneous phantom exposed to an identical irradiation. Commonly, a correction factor is defined from the dose ratio

measured for the heterogeneous geometry versus the homogeneous,

$$CF = \frac{D_{\text{heterogeneous}}}{D_{\text{homogeneous}}}. \quad (1.11)$$

The two main approaches of photon inhomogeneity correction will be discussed and their limitations will be presented.

### A. Correction-based approach

#### i) Power-law (Batho) method

Batho [6] suggested this method as an empirical correction to account for both primary beam attenuation and scatter changes within water and below a single slab of inhomogeneity. It was extended later to include dose calculations within the inhomogeneity [94]. The correction factor which accounts for the density as well as the distance of the inhomogeneity from the point of calculation is given as

$$CF = \frac{TAR(z_1)^{\rho_1 - \rho_2}}{TAR(z_2)^{1-\rho_2}} \quad (1.12)$$

where  $z_1$  is the distance from the point of calculation to the anterior surface of the layer of density  $\rho_1$ , and  $z_2$  is the distance from the calculation point to the anterior surface of the next overlying layer of density  $\rho_2$ .

Later, this method was generalized to handle arbitrary densities and non-water like material [94]. Multiple regions of slab-like material were further accounted for [24, 102]. The most recent developments of this method were presented by El-Khatib and Battista [32] and Thomas [97] who showed that the correction factor should be based on build-up depth-shifted TMRs instead

of the initially proposed TARs to yield

$$CF(z) = \frac{(\mu_{en}/\rho)_N}{(\mu_{en}/\rho)_w} \prod_{m=1}^N (TMR(z - z_m + z_{max}))^{(\mu_m - \mu_{m-1})/\mu_w} \quad (1.13)$$

where  $\mu_m$  and  $\mu_w$  are the linear attenuation coefficients of the material in layer  $m$  and water respectively,  $(\mu_{en}/\rho)_N$  is the mass energy absorption coefficient of the material in layer  $N$ ,  $z_{max}$  is the buildup depth or depth of maximum dose,  $z_m$  is the distance along the beam from the surface to the layer  $m$  in the phantom and  $z$  is the depth to the point of calculation [2].

This method is based on theoretical considerations assuming Compton interactions only. Its original form does not apply to points inside the inhomogeneity or in the build-up regions [6]. The assumption of semi-infinite horizontal geometry renders the application of this method unsuitable in regions with inhomogeneities of finite extent such as near the edges of lungs [105].

### *ii) The equivalent tissue air ratio method (ETAR)*

The ETAR method [95] is modeled after O'Connor's density scaling theorem and applies rigorously for contributions from Compton scattering. It attempts to correct for the scattered radiation component by using multiple-slice CT pixel density information. This method is represented by a ratio of TARs given as

$$CF(z) = \frac{TAR(z', r')}{TAR(z, r)} \quad (1.14)$$

where  $z'$  is the radiological depth (scaled depth) of the calculation point and  $r'$  is the effective beam radius defined by

$$r' = r\rho' \quad (1.15)$$

$$\rho' = \sum_{i,j,k} W_{ijk} \rho_{ijk} / \sum W_{ijk} \quad (1.16)$$

$$\sum W_{ijk} = 1. \quad (1.17)$$

The weighting factors  $W_{ijk}$  are calculated using Compton scatter cross-sections and integrating scatter over the entire irradiated volume for each point of dose calculation. They provide an approximate description of the relative contribution of each volume element having  $\rho_{ijk}$  as an electron density relative to water [50, 56]. In practical cases the choice of weighting factors is empirical. There does not exist a unique set of weighting factors that can be applied to all inhomogeneities [105].

In general, when comparing the above two methods it is noted that the generalized Batho method is more accurate in the high-energy range ( $\geq 10MV$ ), and the ETAR is better suited for the lower energy beams ( $\leq 6MV$ ) [56], however, its accuracy depends entirely on the correct choice of weighting factors. Thus the accuracy of different methods depend on the irradiation conditions including energy, field size, location and extent of inhomogeneity and location of point of calculation.

## B. Model-based approach

The major operational differences between correction-based and model-based calculations is that the first corrects parametrized dose distributions obtained in a water phantom while the second computes dose from first principles. Model based methods such as the convolution/superposition method [1, 19, 20, 66, 72] still require precalculated parameters like the incident photon energy spectra and the primary and scatter dose deposition kernels which

are all derived from Monte Carlo simulation [66, 72].

The convolution method first computes the distribution of TERMA (total energy released per unit mass) in the patient and then convolves it with a kernel that accounts for the transport of charged particles as well as scattered photons [69]. The two most famous methods in this subcategory are the dose spread array [67] and the differential pencil beam methods [72].

*i) The dose spread array*

This method uses a direct summation of density scaled kernels in the dose calculation. The dose at a voxel labeled  $ijk$  is given as

$$D_{ijk} = \sum_{ijk} \Phi_0(i - \Delta i, j - \Delta j, k - \Delta k) \rho(i - \Delta i, j - \Delta j, k - \Delta k) \\ \left[ \frac{A_{0,1}(\rho_l l, \Delta i, \Delta j, \Delta k)}{\rho_l} + \frac{A_m(\rho_m l, \Delta i, \Delta j, \Delta k)}{\rho_m} \right], \quad (1.18)$$

where  $\Phi_0$  is the primary photon fluence incident at a given voxel  $(i - \Delta i, j - \Delta j, k - \Delta k)$ ,  $A_{0,1}$  is the combined dose spread array due to primary and proximal first scatter photon interactions,  $A_m$  is the dose spread array due to all other photon interactions,  $\rho_l$  is the average density along the ray path  $l$  connecting the primary interaction site to the dose point,  $\rho_m$  is the empirical average density of the medium [67, 105]. Dose spread arrays were generated for a range of densities to facilitate data lookup using O'Connor's density scaling method.

*ii) The differential pencil beam*

A differential pencil beam is an infinitesimal segment of a pencil beam directed along a ray line from the beam source, within which primary ph-

tons interact and give rise to a differential pencil beam dose distribution. The differential pencil beam dose distribution is equivalent to a convolution kernel except that it is dose deposited in water per number of primary photons interacting in a unit volume, instead of per unit energy imparted by primary photons [69, 72]. The dose at a point in the medium is given as

$$Dose = \sum \Phi_0 \rho_c DPB(r, \theta) \Delta V, \quad (1.19)$$

where  $DPB(r, \theta)$  is the differential pencil beam dose distribution in water as generated by Monte Carlo simulation and expressed in spherical coordinates  $(r, \theta)$ .  $r$  is the distance between the primary interaction site to the point of calculation and  $\theta$  is the angle with respect to the beam direction.  $\rho_c$  is the photon collision density at the volume  $\Delta V$  defined above, and  $\Phi_0$  is the primary photon fluence [72, 105].

In principle, the input data of the dose spread array and the differential pencil beams methods are identical. For dose calculation in a heterogeneous medium, the density information between the primary interaction site and the dose point is sampled using first-order scatter ray tracing. Density scaling using the O'Connor theorem is employed and a dose value in an equivalent homogeneous geometry is adopted.

### 1.6.2 Explicit modelling of particle interaction and transport

None of the current photon dose algorithms include the effects of atomic number changes in a heterogeneous phantom, which produce changes in electron

multiple scattering and pair production. Moreover, the presence of inhomogeneities with different scattering and stopping powers perturbs the transport of the secondary electrons differently compared to inhomogeneities of only density variations [110]. This leads to two important methods that are potentially able to handle these limitations.

### A. Random methods, Monte Carlo

Of all the possible methods of predicting a dose distribution due to an incident photon beam in a heterogeneous phantom, the one that is potentially the most accurate is Monte Carlo modeling. This modelling provides an alternative to the correction methods by calculating the distribution in an inhomogeneous medium from first principles, using the physics of photon and electron transport [69].

The transport of an incident particle, and of particles that are subsequently set in motion, is referred to as a particle history. Photons have a limited number of interactions before their histories terminate, which makes it easy to simulate all interactions directly. In electron transport, however, the number of Coulomb interactions with atomic nuclei is so large that a direct Monte Carlo simulation is impractical. Instead, multiple scattering theories are used to sample angular deflections and energy losses in successive short track segments. The length of these segments (step sizes) are chosen such that: 1) a sufficient number of collisions must occur within each segment, so that the application of multiple scattering theories is justified; 2) the cumulative deflections and energy losses in each segment must be small enough so that the "condensed" history model provides a sufficiently accurate simulation of electron-track generation, boundary crossings and the scoring of energy depo-

sition. In this way "condensed" history techniques have been developed where "microscopic" interactions are utilized to provide a "macroscopic" representation of the particle transport in heterogeneous media [3, 10, 15, 53, 85].

A dose distribution can be calculated by summing the energy deposition in each particle history. However, a large number of histories (depending on the beam field size) are required before the uncertainty in the distribution is small enough for it to be used in treatment planning [42, 64, 69]. Furthermore, long calculation times are a pronounced problem in conformal therapy. In such settings iterative algorithms are utilized for dose distribution optimization requiring the dose to be recomputed many times during the planning procedure. Monte Carlo simulation is currently used for beam characterization, benchmarking and other special studies. At present, a few centers [42, 64, 101] adopt Monte Carlo techniques for treatment planning, however it is unlikely that this practice will become routine in the next decade [2].

## B. Deterministic methods for particle transport

A radiation field can be most generally described by the phase space density, representing the number of particles per six-dimensions made up of the three spatial coordinates ( $x, y, z$ ), the particle energy ( $E$ ) and the direction  $\Omega = (\theta, \phi)$ . The phase space of radiation beam particles can be completely represented by the vectorial energy fluence differential in energy and directions for photons,  $\Phi_{E,\Omega}^{ph}$ , and for charged particles (electrons and positrons),  $\Phi_{E,\Omega}^{cp}$ . The dose at a point  $r$  can be derived from these fluences as [89]

$$D(r) = -\frac{1}{\rho(r)}(\nabla \cdot \Phi_{E,\Omega}^{ph}(r) + \nabla \cdot \Phi_{E,\Omega}^{cp} - q(r)) \quad (1.20)$$

where  $\rho$  is the mass density and  $q$  is the rest mass energy change per unit

volume. The main problem with this method lies in the evaluation of the resulting fluence distribution.

*i) Boltzmann transport equation*

The Boltzmann transport equation can be the starting point for describing radiation transport [9, 14]. It ensures conservation of energy and can govern the production and loss of particles. The linear time-independent integral form of the Boltzmann equation is given as

$$\Phi(r, v) = \int \left[ \int \Phi(r', v') I(v' \rightarrow v; r') dv' + Q(r', v) \right] T(r' \rightarrow r; v) dr' \quad (1.21)$$

where phase space is described by  $r$ , a position vector, and  $v$ , velocity vector.  $\Phi$  is the energy fluence and  $Q$  is the source distribution of primary particles. The interaction kernel  $I(v' \rightarrow v; r')$  takes into account the interactions that change the particle velocity, whether due to energy loss (absorption or inelastic scattering) or direction changes (elastic scattering) and production of secondary particles. The transport kernel  $T(r' \rightarrow r; v)$  changes the primary and secondary particle positions by determining the path taken between collisions [52].

The scattering and absorption processes make the Boltzmann equation difficult to solve except for very simplified cases [9]. Making use of such a complete deterministic approach would probably exceed the complexity and computational burden of the Monte Carlo method [2, 18].

*ii) Fermi-Eyges transport equation*

In his search for a cosmic-ray theory, Fermi proposed a model for particles diffusing in a medium in which the main interaction is due to multiple

Coulomb scattering [88]. A charged particle initially traveling along the  $z$  axis undergoes angular deflection  $\theta$  with an azimuthal angle  $\phi$  (direction coordinates) after interacting with the Coulomb field of nuclei in the medium. Due to cylindrical symmetry around the  $z$  axis, calculations can be simplified by working in a two dimensional plane ( $x - z$  plane) and later generalizing the results to three dimensional space. The charged particle projected angular deflection onto the  $x - z$  plane is given by  $\theta_x$  where

$$\tan \theta_x = \tan \theta \cos \phi, \quad (1.22)$$

and its position coordinates are  $x$  and  $z$ .

A distribution function  $P_x(x, \theta_x, z)$  is defined such that  $P_x(x, \theta_x, z)\Delta x \Delta \theta_x$  is the probability that the electron will be located between  $x$  and  $x + \Delta x$  and have direction between  $\theta_x$  and  $\theta_x + \Delta \theta_x$ , when it is at depth  $z$ . It was demonstrated that  $P_x$  must satisfy the following equation:

$$\frac{\partial P_x}{\partial z} = -\theta_x \frac{\partial P_x}{\partial x} + \frac{k}{4} \frac{\partial^2 P_x}{\partial \theta_x^2}, \quad (1.23)$$

in which a small angle approximation was invoked by setting  $\sin \theta \approx \theta$ .

Fermi provided a solution for the above partial differential equation for a special case of constant  $k$ . Eyges [35] solved the above equation for a depth dependent  $k$  ( $k(z)$ ).  $k(z)$  is interpreted as the linear scattering power of a medium and is given as [79]

$$k(z) = \frac{d\theta^2}{dz}. \quad (1.24)$$

The depth dependence of the scattering power of a medium arises because some particles lose an appreciable amount of energy through hard and

soft collisions while traversing that medium. The degree of this dependence is related to the type of incident particle and the nature of the medium. An example are electrons entering a water phantom where approximately 2 MeV of their kinetic energy is lost per 1 cm of penetration depth.

The solution to Equation 1.23 can be expressed as

$$P_x(x, \theta_x, z) = \frac{1}{\pi \sqrt{A_0 A_2 - A_1^2}} \exp \frac{-(A_0 x^2 - 2A_1 z \theta_x + A_2 \theta_x^2)}{(A_0 A_2 - A_1^2)}, \quad (1.25)$$

where the parameters  $A_n$  are called the "scattering moments" of the medium and are given as

$$A_n(z) = \int_0^z k(z') (z - z')^n dz'. \quad (1.26)$$

Then, according to Equation 1.20, finding the dose at a given depth  $z$  for electrons passing between  $x$  and  $x + \Delta x$  requires finding the fluence or the number of electrons irrespective of direction. Thus the location probability density is defined as [47, 48]

$$G_x(x, z) = \int_{-\infty}^{+\infty} P_x(x, \theta_x, z) d\theta_x, \quad (1.27)$$

which after evaluation yields a Gaussian of the form:

$$G_x(x, z) = \frac{1}{\sqrt{\pi A_2(z)}} \exp -\frac{x^2}{A_2(z)}. \quad (1.28)$$

The solution to the Fermi-Eyges equation in  $y$  and  $\theta_y$  is identical to the above, and the three dimensional form of the location probability (Equation 1.28) is finally given as

$$G(x, y, z) = \frac{1}{\sqrt{\pi A_2(z)}} \exp -\frac{x^2 + y^2}{A_2(z)}. \quad (1.29)$$

Three important limitations of the Fermi-Eyges theory are: first the use of small angle approximation in the scattering of particles, second the neglect of bremss-trahlung energy losses which are important in high-z materials and most importantly third is the absence of delta ray ( $\delta$ -ray) production. The third limitation has restricted the use of this theory in electron dose calculation as in its original form. However, the incorporation of measured electron beam data made the Fermi-Eyges theory a successful approach for electron beam treatment planning [27, 44, 83, 104].

## 1.7 Thesis objectives and highlights

Two main objectives are pursued in this thesis.

The first is to quantitatively study the extent of the discrepancy between measurements and current dose calculation algorithms when applied to extreme inhomogeneities like air gaps. The implemented versions of these algorithms on commercial CT-based treatment planning systems were used.

The second is to devise an analytical model for inhomogeneity correction incorporating electron transport. We will introduce the concept of separating the inhomogeneity correction factor into primary and scatter factors. For primary calculation, a detailed electron transport is done using the Fermi-Eyges theory. For the scatter correction, a semi-empirical model based on ratios of TMRs is discussed. Important features of our approach are:

- Present models require Monte Carlo precalculated data in water and

density scaling operations to account for inhomogeneities. The aim of our method is to use basic physics to come up with an analytical method that is practicle when applied to radiation therapy treatment planning.

- Our approach is based on a knowledge of the physics of photon and electron interactions with matter. Calculations for primary Compton dose distribution are made from first principles and a comparison with EGS4 Monte Carlo simulation is conducted. Scatter correction is of less importance and it is presented along with the primary correction as a total correction factor model.

- Special attention is given to computation time. An optimization procedure is introduced to make the application of this method feasible in a clinical setting.

As an additional topic, the clinical applicattion of GEANT3, a Monte Carlo code based on CERN library, will be investigated. The main goals are to explore the different electron transport modes implemented in GEANT3 and make a direct comparison with EGS4 and phantom experiments.

Therefore, this thesis is composed of three main chapters, an introduction and conclusions. Some analytical derivations related to the third chapter were put in Appendix A. For reference, the computer code BATOUL.c, written in the 'C' language, which was used to implement our method is provided in Appendix B. Appendix C contains the computer routine DOSE.f, written in FORTRAN, which was the usercode driver for the GEANT3 simulations.

## **Chapter 2**

### **Experiments and treatment planning calculations in phantoms with air cavities**

#### **2.1 Introduction**

Simplistic radiation dose calculations at a point usually presuppose that the point is located in a region where electronic equilibrium exists. This assumption breaks down at interfaces of materials of different density and atomic number. A loss of both longitudinal and lateral electronic equilibrium occurs, the extent of which depends on the energy, radiation field size and the range of charged particles set in motion. As the x-ray energy is increased, the range of charged particles set in motion also increases. Therefore, as the beam energy is increased the region of electronic disequilibrium becomes significant particularly for low density tissues. These effects are clinically important in the thoracic region where the lung, a low density organ, occupies a large volume.

Accurate dosimetry is critical to reduce toxicity in radiation therapy.

Dose measurements and calculations both within and beyond inhomogeneities have been extensively reported [7, 26, 31]. The most commonly used dose correction methods for lung inhomogeneity correct the dose for changes in photon fluence but do not account for changes in charged particle transport and therefore may not accurately predict the dose in interface regions [7, 66, 68]. These methods are: the ratio of TAR's, the Batho or power law correction [6], the equivalent TAR (ETAR) method [94, 95] or variations thereof [105].

The introduction of a low density material alters the radiation transport in a complex manner. The primary transmitted radiation is increased because the lower density material attenuates the beam less. However, per  $mm^3$ , there are fewer photons scattered by the lower density material. This produces a decrease in dose. There are also fewer charged particles generated per  $mm^3$  of low density material but their ranges are larger. The result is that inhomogeneity corrections will be greater for smaller field sizes and lower x-ray energies [66, 68].

Besides the lung, other regions of low density are air cavities situated in the upper respiratory tract. These may be larger than  $1 \times 1 cm^2$  in cross section. The dose received by tissues situated at the interface of the air channel or beyond is of clinical significance and may influence outcome of treatments with curative intent. Several studies have reported underdosing at interfaces due to loss of electronic equilibrium [33, 80]. The degree of underdosing depends on the energy of the radiation beam, field size and geometry of the air cavity. Directly at the interface the dose is lower for higher energy and smaller field size [8, 57, 109]. Beyond the interface the dose becomes greater than its corresponding value in homogeneous tissue [57]. In an investigation of air cav-

ity interface dose in a humanoid phantom, the variation in dose with energy was found to be clinically insignificant, however, a strong dependence on the shape and geometry of the air cavity is reported [77].

The present study was initiated to quantify the extent of discrepancy between measurements and calculations using three treatment planning systems and to assess the dose in heterogeneous phantoms, at the air/polystyrene interface and at depths for varying air gap geometries.

## 2.2 Experimental Procedure

Irradiations were performed with 6 *MV* and 18 *MV* x-rays produced by a Philips SL20 linear accelerator (Elekta Oncology Systems/Philips Medical Systems, Sweden and U.K.). Field sizes of 5x5  $cm^2$  and 10x10  $cm^2$  at a source to chamber distance (SCD) of 100  $cm$  were used. The experimental setup is depicted in Figure 2.1. A parallel plate air ionization chamber (Markus PTW model 30-329, Victoreen Nuclear Associates, Carle Place, NY) was used for the measurements. This chamber has a polyethylene window of thickness 2.7  $mg/cm^2$ , a 5.4  $mm$  diameter circular collector, a nominal charge collection volume of 0.05  $cm^3$  and a 2  $mm$  electrode separation. The chamber is located at the air/polystyrene interface at a constant distance of 100  $cm$  from the source (SCD setup). In Figure 2.1(c), a constant distance of 100  $cm$  between the source and the distal the air/polystyrene interface was mantained (SAD setup) while the chamber was moved down the phantom. The effective point of measurement is the proximal surface of the chamber. The polarity effect was investigated and found to be less than 1%.

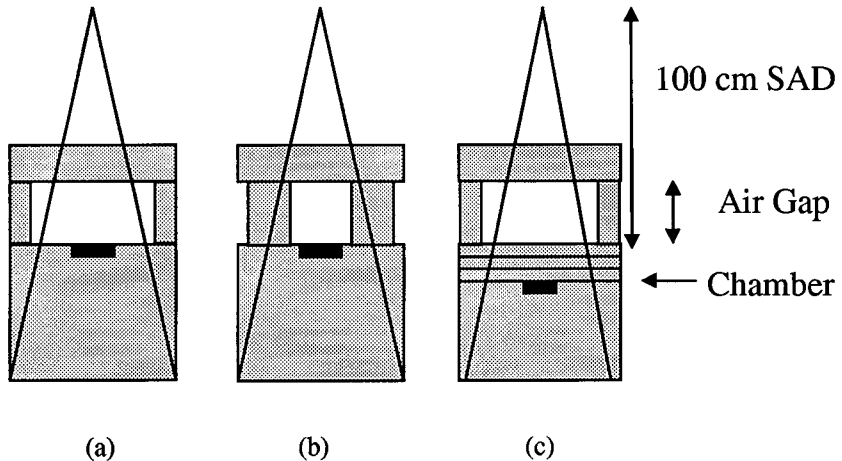


Figure 2.1: The experimental setup used for the three experiments is shown. The black rectangle represents the position of the Markus Chamber.

The air gap depth was varied from 1  $cm$  to 5  $cm$  while keeping a 3  $cm$  polystyrene buildup slab above it. The dose  $D_i$  was measured at the air/polystyrene interface and the dose  $D_h$  was measured at a depth of 3  $cm$  of homogenous phantom. The relative dose was then determined from  $D_i/D_h$ . In the first experiment, the lateral dimension of the air gap was made larger than the radiation field size (Figure 2.1a). In the second experiment the lateral dimension of the air gap was varied from 0x0  $cm^2$  (no air gap) to 20x20  $cm^2$  (Figure 2.1b). The width of the air cavity was altered to investigate the contribution of scattered radiation on the interface dose for the 5x5  $cm^2$  field size. The depth ( $t$ ) of the air gap used was 3 and 5  $cm$  for the second experiment. The dose normalization point was situated in a homogeneous polystyrene phantom at depths 3  $cm$  +  $t$  for the 0x0  $cm^2$  air gap. The effect

of primary photon attenuation was investigated by adding polystyrene layers on top of the point of measurement keeping the SAD (source to interface distance) constant at 100 *cm*. Measurements were carried out for air gaps of 5 *cm* depth. Polystyrene sheets were added to increase the depth of measurement up to 4 *cm* beyond the air/polystyrene interface (Figure 2.1c). Again dose normalization was at 8 *cm* deep in the homogeneous phantom.

In these experiments, relative ionization measurements read by the chamber are not exactly the same as relative dose measurements, but should be quite close because the mass stopping power ratio (Equation 1.9) changes little as a function of depth [66]. Therefore, the relative dose at a given depth was equated to the relative ionization. Furthermore, several ionization readings were taken per point and the results were averaged. Repeated measurement series taken on different days indicate that dose measurement at a given depth have a statistical uncertainty of the order of 1%. Hence, relative dose value have an uncertainty of the order of 2%.

## 2.3 Treatment Planning Systems

Three treatment planning systems were used for the relative dose calculation. These are: Cadplan (Varian Oncology Systems, Varian/Dosetek, Zug, Switzerland), General Electric Target 2 (General Electric, Milwaukee, WI), and an in-house developed treatment planning system (Xplan, Vancouver Cancer Centre, B.C., Canada). The Cadplan system employs three methods of inhomogeneity correction which are user selectable: the Batho, modified Batho and the equivalent TAR (ETAR) methods. The modified Batho method uses only

the descending portion of the TMR curve. This was suggested after imposing continuity of the correction factor at the interface between dissimilar media [97]. This calculation does not reflect build-down and re-buildup at interfaces.

Mathematically, the correction factor for the Batho method is given by Equation 1.13 evaluated at the depth  $z - z_m$  as defined in Chapter 1. In the modified Batho method the depth of  $z_{max}$  is added to the depth of calculation as given by Equation 1.13. Therefore the Batho and the modified Batho models differ only in the depth definition for the TAR/TMR value.

The second system studied is the GE Target 2. It uses the Batho method with the capability of doing 3D dose calculation. Finally, an in-house system (Xplan) implemented at the Vancouver Cancer Center was also assessed. This system uses the same Batho method as Cadplan with only 2D dose calculation capabilities for 6 MV photons.

## 2.4 Results and Discussion

Dose perturbations produced by air gaps are due to alterations in both photon and electron transport. As the air gap thickness increases electrons from the upper polystyrene layer no longer reach the point of measurement giving rise to a second build up region. Thus the point of measurement effectively represents another surface.

Figure 2.2 shows results of experimental measurements and calculations of the relative dose ( $D_i/D_h$ ) for 6 MV photons using the Batho, modified

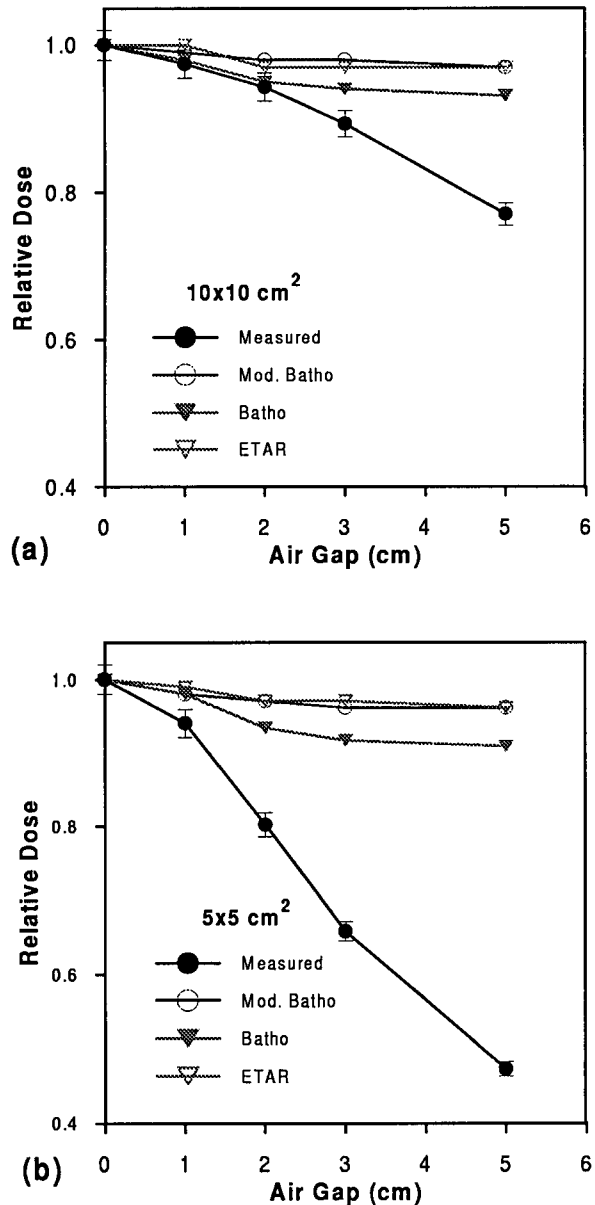


Figure 2.2: Comparison of calculated and measured relative dose ( $D_i/D_h$ ) for 6 MV photons is shown for (a)  $10 \times 10 \text{ cm}^2$  and (b)  $5 \times 5 \text{ cm}^2$  field sizes. Calculations of relative dose using the Batho, modified Batho and ETAR correction methods as implemented on Cadplan lie between 1 and 0.9 while measurements with the Markus chamber show a decrease down to 0.45. Results are normalized to unity at depth 3 cm in the homogeneous polystyrene phantom.

Batho and equivalent TAR (ETAR) inhomogeneity correction methods on the Cadplan system for a  $10 \times 10 \text{ cm}^2$  (Figure 2.2a) and a  $5 \times 5 \text{ cm}^2$  (Figure 2.2b) field size. In this experiment the  $3 \text{ cm}$  polystyrene slab is moved away from the point of measurement and the air gap increases from 1 to  $5 \text{ cm}$ . The decrease in the measured relative dose is attributed to changes in electron transport and loss of electronic equilibrium. As the air gap increases less secondary electrons are seen by the detector since they are dispersed over a greater range. However, for larger field sizes an increase in the scatter component predominates, producing greater relative dose.

Calculation methods only account for changes in photon transport while assuming electronic equilibrium. The decrease in calculated relative dose is much less than that measured. In our experimental setup the primary beam attenuation is unaffected by the size of the air gap. Therefore, the decrease in relative dose is attributed to less scattered radiation reaching the point of calculation as the air gap increases up to  $3 \text{ cm}$  after which point the relative dose remains constant. However, the dose is significantly overpredicted in the calculation. For instance, the relative dose calculated using the Batho method for a  $5 \times 5 \text{ cm}^2$  field irradiated with a  $6 \text{ MV}$  beam behind a  $5 \text{ cm}$  air gap is 0.9 whereas the measured relative dose is 0.45. While air gaps in the head and neck region are typically less than  $3 \text{ cm}$  and larger air gaps are not encountered clinically, our experiments are designed to illustrate the limitations of the treatment planning algorithms. A similar trend of the relative dose as a function of air gap thickness was observed using the three methods with the Batho method differing by 5 percent from the modified Batho and ETAR methods.

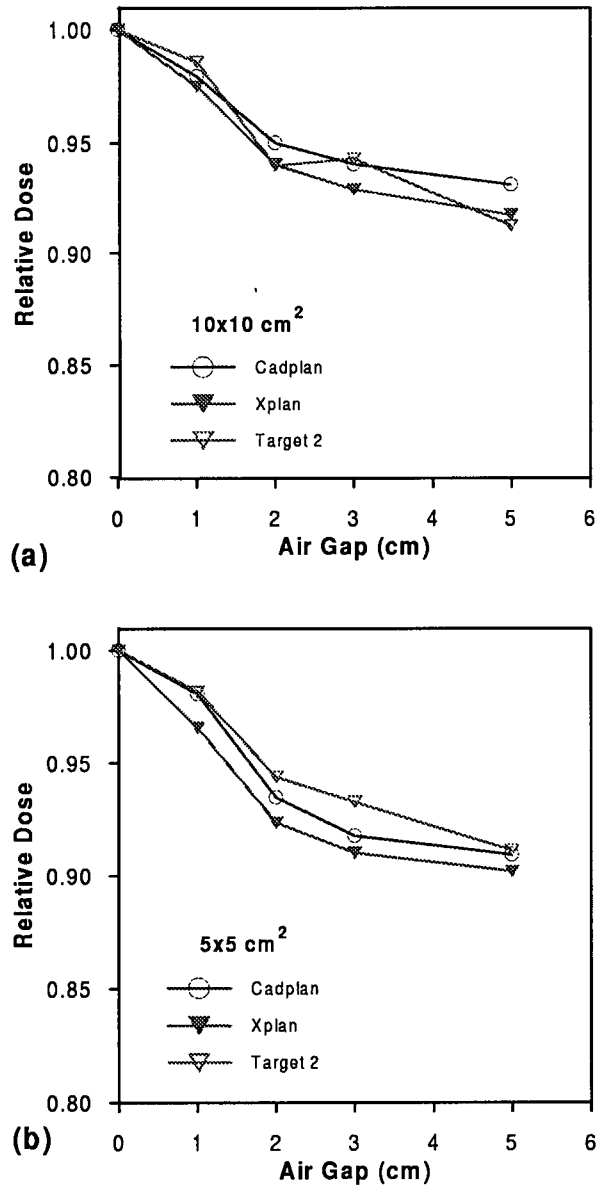


Figure 2.3: Relative dose calculation is shown as a function of air gap thickness using the Batho correction method as implemented on the Cadplan, GE Target 2 and Xplan treatment planning systems. A 6 MV beam and two field sizes, (a)  $10 \times 10 \text{ cm}^2$  and (b)  $5 \times 5 \text{ cm}^2$  were used.

To illustrate differences that may occur with the implementation of the Batho method on different treatment planning systems results based on three treatment planning systems are presented in Figure 2.3. Relative dose calculations for the 6 *MV* photon energy and two field sizes ( $10 \times 10 \text{ cm}^2$  and  $5 \times 5 \text{ cm}^2$ ) are shown. The field size dependence is insignificant in the case of the GE Target 2 system. All the results for the 3 treatment planning systems lie within a 5 percent range.

In the second experiment where the side walls are smaller than the radiation field size (Figure 2.1b), photons scattered from the walls of the cavity as well as electron transport, contribute to the overall behavior of the absolute dose with change in the air gap thickness. Variation in the lateral dimensions of the cavity will eventually influence this behaviour. As the lateral dimensions of the cavity were increased from  $0 \times 0 \text{ cm}^2$  (no cavity) to  $2 \times 2 \text{ cm}^2$  the relative dose increased since the primary photon fluence is no longer attenuated. For both 6 *MV* (Figure 2.4a) and 18 *MV* (Figure 2.4b) the dose reaches a maximum at lateral dimensions of  $2 \times 2 \text{ cm}^2$ . It decreases afterwards due to a smaller number of photons scattered by the walls reaching the detector. Furthermore, the increase in the air gap thickness resulted at first in a higher dose because of greater scatter from the thicker walls; but as the air gap dimension approaches the radiation field size dimension, thicker air gaps result in a lower dose. The latter is consistent with the results of the first experiment (Figure 2.2) where the phenomenon is attributed to a reduction in electron transport. Calculations are not presented at this point since their limitations at the interface was already shown in Figures 2.2 and 2.3.

Figure 2.5 (a, b) shows the variation of dose as a function of depth for

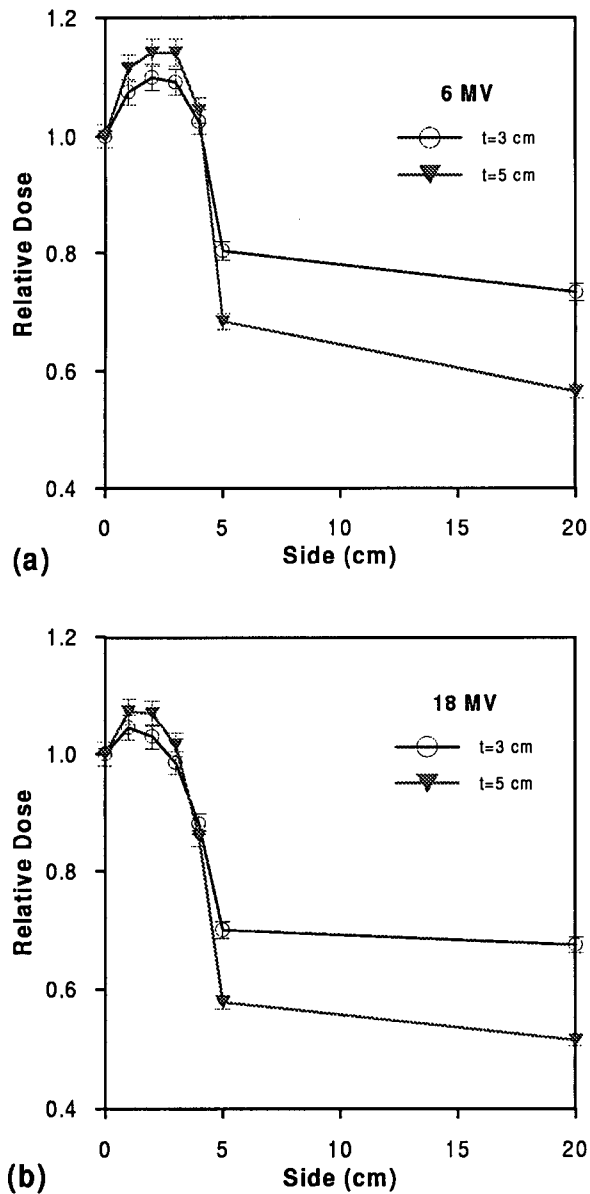


Figure 2.4: Measurements of the relative dose as a function of air gap side for a  $5 \times 5 \text{ cm}^2$  field size are shown. Sides were varied from  $0 \times 0$  (no gap)  $\text{cm}^2$  to  $20 \times 20 \text{ cm}^2$  for two different air gap thicknesses (3 and 5 cm): (a) 6 MV photons and (b) 18 MV photons. The dose was normalized to the dose in homogeneous phantom with 6 cm ( $t = 3 \text{ cm}$ ) and 8 cm ( $t = 5 \text{ cm}$ ) of polystyrene over the detector.

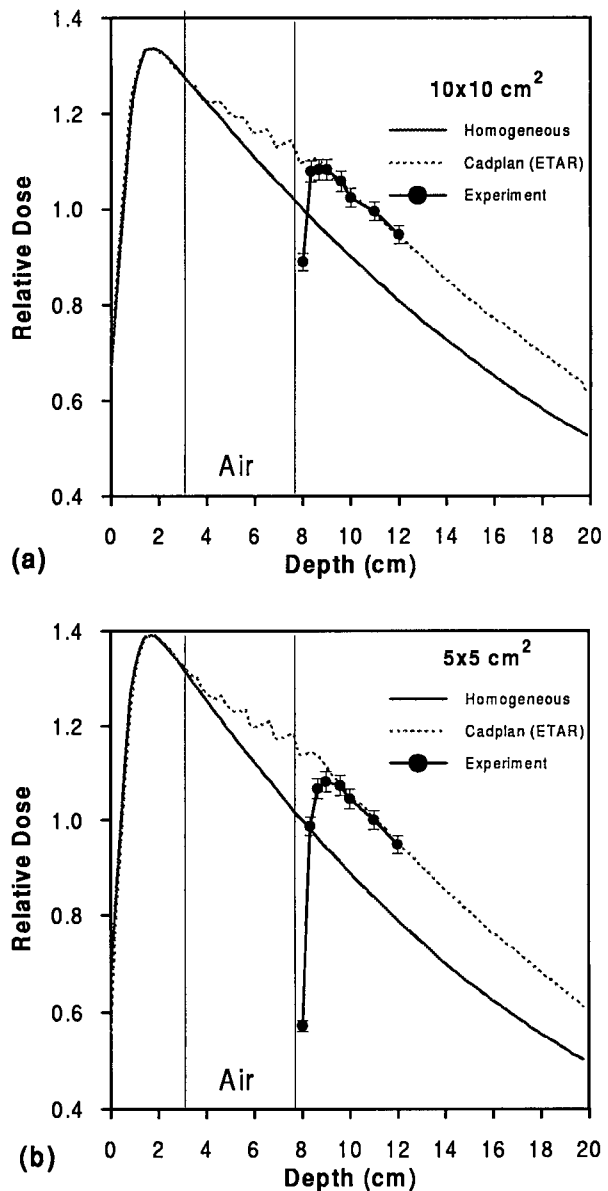


Figure 2.5: Measurements of the relative dose as a function of depth in a phantom with a 5 cm air gap thickness for 6 MV photons are shown, (a) for a  $10 \times 10 \text{ cm}^2$  field size and (b) for a  $5 \times 5 \text{ cm}^2$  field size. The dose was normalized to the dose in the homogeneous phantom at 8 cm deep. The position of the air gap is indicated by the bordered region.

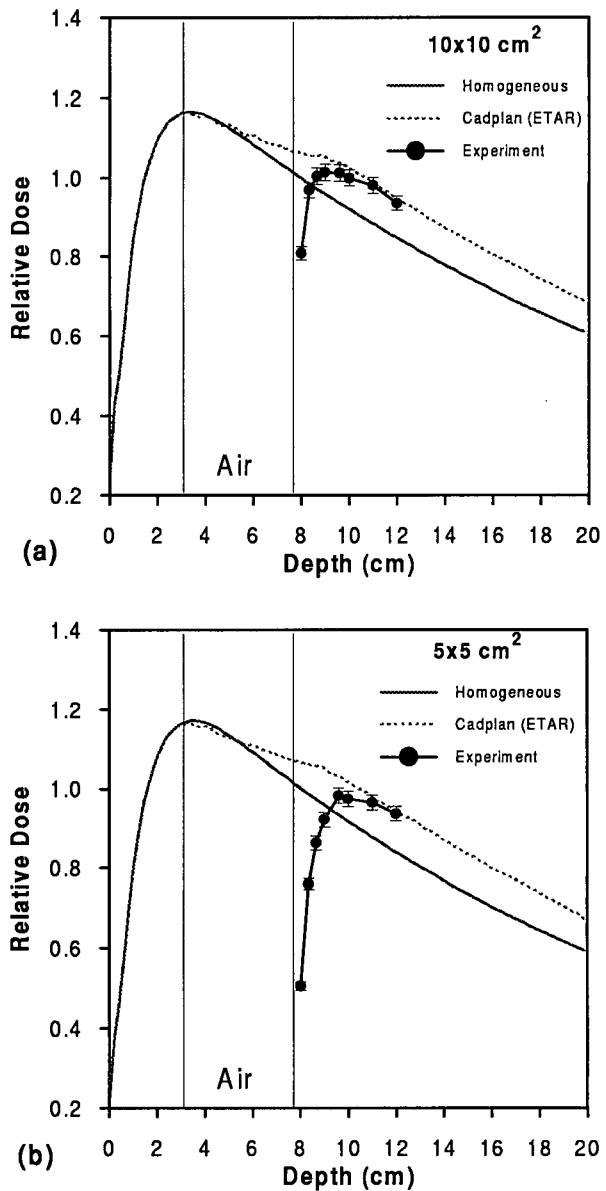


Figure 2.6: Measurements of the relative dose as a function of depth in a phantom with a 5 cm air gap thickness for 18 MV photons are shown, (a) for a  $10 \times 10 \text{ cm}^2$  field size and (b) for a  $5 \times 5 \text{ cm}^2$  field size. The dose was normalized to the dose in the homogeneous phantom at 8 cm deep. The position of the air gap is indicated by the bordered region.

(a)  $10 \times 10 \text{ cm}^2$  and (b)  $5 \times 5 \text{ cm}^2$  fields irradiated with  $6 \text{ MV}$  photons using an air gap thickness of  $5 \text{ cm}$ . Figure 2.6 (a, b) shows the results of the same irradiation conditions for  $18 \text{ MV}$  photons. The position of the air gap is indicated by the bordered area. There was a build up in the dose after the air/polystyrene interface which was more significant for the smaller field size. The maximum dose occurs when the thickness of polystyrene approaches the maximum range of primary electrons for the respective energies investigated ( $6$  and  $18 \text{ MV}$ ) in this second buildup region. Furthermore, the application of the ETAR method as implemented in CADPLAN did not predict this second buildup. There was good agreement at greater depths, beyond the maximum dose ( $1.5 \text{ cm}$  for  $6 \text{ MV}$  and  $2.5 \text{ cm}$  for  $18 \text{ MV}$ ) where electronic equilibrium was re-established.

## 2.5 Summary

A series of experiments were carried out to simulate air cavities in a polystyrene phantom. Dose was measured at an air/polystyrene interface and as a function of depth. Results of experiments were compared to calculations done using three treatment planning systems. These systems employ Batho, modified Batho and the equivalent tissue-air-ratio (ETAR) methods for inhomogeneity corrections. The measured interface dose decreased by 55% for a  $5 \text{ cm}$  air gap,  $5 \times 5 \text{ cm}^2$  field size and  $6 \text{ MV}$  photons. This has been attributed to lack of electronic equilibrium and dispersion of secondary particles transported through the air gap. These results are at variance with predictions of calculations using three treatment planning systems, for which only a 10% decrease

was calculated. This is because the calculation algorithms employed do not incorporate electron transport. Further experiments were conducted to study the contribution of scatter from the sides of the walls of the cavities. Dose measurements as a function of depth were also performed to investigate the effect of primary fluence attenuation. The Batho algorithm did not show any sensitivity to the position of air gap side walls. This points to the need for proper inclusion of disequilibrium effects and shape of inhomogeneity.

# **Chapter 3**

## **Inhomogeneity correction factor incorporating explicit electron transport**

### **3.1 Introduction**

Although most of the radiation treatment planning algorithms accurately predict dose in homogeneous tissues there are differences in accuracy for dose calculations within and beyond heterogeneous tissues especially in the interface region of dissimilar media [2, 26, 31, 66, 68, 93]. In inhomogeneous media the radiation dose to homogeneous water equivalent tissue is calculated and modified by an inhomogeneity correction factor (ICF). The ICF is defined as the ratio of the dose beyond or within inhomogeneous tissue to that in homogeneous tissue at the same geometries point [2, 6, 94].

The most accurate calculation methods currently available for radiation dose calculations in inhomogeneous tissues are Monte Carlo based techniques [28, 42, 43, 64]. However, these techniques are too computationally intensive to

use for routine clinical treatment planning with currently available computer hardware. The next most physically rigorous x-ray dose calculation methods are the convolution/superposition algorithms [1, 19, 67].

The convolution/superposition method was developed with particular intent to handle the condition of electronic disequilibrium in high-energy photon beams. For these beams the electrons set in motion have long tracks of the order of a few centimeters. In this method, the Monte Carlo method is used to calculate the dose distribution resulting from photon interaction at a point referred to as the photon kernel. This kernel can be divided into two components [67, 107]: the primary kernel, defined as the spatial distribution of energy deposited by electrons and positrons emerging from the site of the primary photon interaction; the scatter kernel which represents the distribution of deposited energy resulting from the interaction of scattered photons. For this kernel, the electrons generated are generally lower in energy than the primary kernel and their energy can be assumed to be deposited locally.

In an inhomogeneous phantom, the convolution/superposition method attempts to correct for the effects of density variations by linearly scaling the primary and scatter kernels. The rectilinear scaling method is based on O'Connor's theorem [78] to account for secondary electron and scattered photon transport in inhomogeneous media [54, 67]. Woo and Cunningham [106] showed that rectilinear scaling leads to an overestimation in dose in a layer beyond a high to low-density interface due to primary interactions before the interface. This overestimation (up to 50% in the case of an air gap) is because the largest contribution to lateral electron spread at a plane is from scattering events furthest from the plane, and this effect is not accounted for by the

rectilinear scaling. This discrepancy increases with larger air gap thicknesses but decreases with larger field sizes [93].

Yu et al [110] calculated the primary photon dose inclusive of explicit electron transport, and also the scatter photon dose using the convolution/superposition method. In their work, Fermi-Eyges electron scattering theory is used to transport the electrons set in motion at the primary photon interaction site from which the dose deposited was subsequently calculated. The scatter photon component which contributes a portion of the total dose is calculated using the dose spread array method of Mackie et al [67]. Only aluminum inhomogeneities were considered in their study. However, the main emphasis of their model for predicting dose accurately in the vicinity of inhomogeneities is on the transport of the secondary electrons generated at the primary interaction site.

Yu et al's approach [?] has three major drawbacks, 1) the need to derive Monte Carlo simulated parameters (initial scattering moments) which make it similar to convolution algorithms, 2) the use of certain assumptions, and values of parameters in particle transport integrals, (e.g. all secondary electrons have the same mean angle need to be quantified), 3) high computational cost (i.e. routine clinical dose calculation using this method is impractical). The first drawback renders this model a Monte Carlo dependent method requiring precalculation of the parameters for all energies and materials encountered in radiation therapy. The second, using arbitrary numbers for parameters makes it subject to systematic errors. The third drawback remains an outstanding problem that needs to be addressed.

In this work, we present a method to calculate the inhomogeneity correc-

tion factor incorporating explicit electron transport. Up to now, the concept of primary and scatter dose separation has been applied to the calculation of total dose. In our method, we used this concept of separation to calculate a primary inhomogeneity correction factor ( $ICF_p$ ) and a scatter inhomogeneity correction factor ( $ICF_s$ ). An  $ICF$  is eventually calculated as a weighted sum of the primary and scatter  $ICF$ . This method will be described and tested in inhomogeneous phantoms containing air cavities in tissue. For the  $ICF_p$  calculation, secondary electrons emerging from primary Compton interactions are transported. The explicit electron transport will be based on the "photon-electron cascade model" approach [110] and a Gaussian multiple-scattering theory [48, 100]. For the scatter  $ICF$  calculation ( $ICF_s$ ), we present a semi-empirical method that is similar to the "equivalent tissue-air ratio" method and corrects for scatter dose in inhomogeneous phantoms. The result is a correction method that accounts for both photon and electron transport and can be calculated in a time appropriate for routine clinical implementation.

## 3.2 Theory and Methods

The theoretical development of our approach is presented which includes two subsections: primary dose correction and scatter dose correction. Furthermore, the description of Monte Carlo simulation and experiments used to verify our results are discussed in later sections.

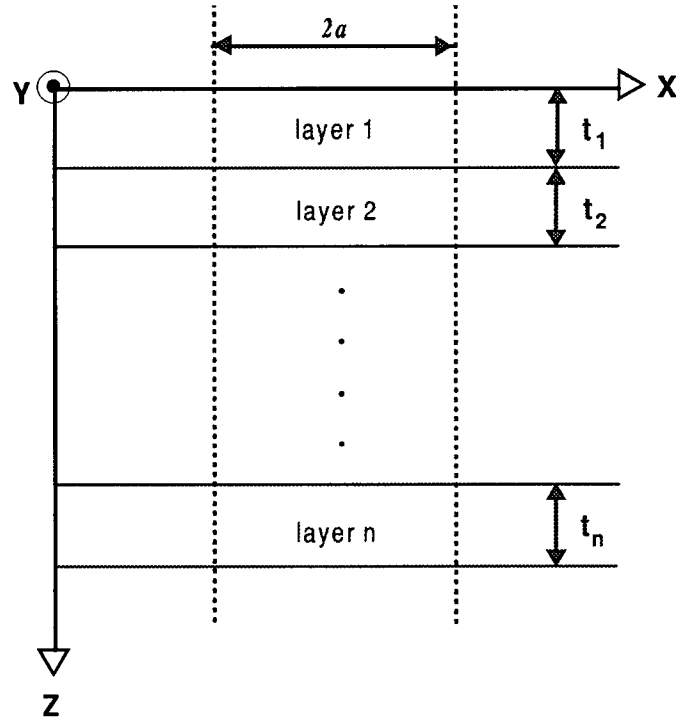


Figure 3.1: The multilayered geometry used in our calculations is shown.

### 3.2.1 Theory

The inhomogeneity correction factor (*ICF*) is defined as the ratio of dose in the inhomogeneous phantom to the dose in the homogeneous phantom at the same geometries point. Using the concept of primary and scatter separation, *ICF* will be given as

$$ICF = \frac{D_{p,inh} + D_{s,inh}}{D_{p,hom} + D_{s,hom}}, \quad (3.1)$$

where  $D_p$  and  $D_s$  are the corresponding primary and scatter components of dose in the inhomogeneous and homogeneous phantoms.

In fact, letting our correction factor for the primary dose be:

$$ICF_p = \frac{D_{p,inh}}{D_{p,hom}}, \quad (3.2)$$

and the correction factor for the scatter dose be:

$$ICF_s = \frac{D_{s,inh}}{D_{s,hom}}, \quad (3.3)$$

we can combine the two to come up with the total correction factor as follows:

$$ICF = \frac{D_{inh}}{D_{hom}} = ICF_p \cdot R + ICF_s \cdot (1 - R), \quad (3.4)$$

where  $R = D_{p,hom}/D_{total,hom}$  is the ratio of the primary dose over the total dose in the homogeneous phantom. The next two sections will be devoted to the derivation of  $ICF_p$  and  $ICF_s$ .

## I. Primary inhomogeneity correction factor

Two main aspects are considered in our  $ICF_p$  derivation: Electron production and electron transport. As was shown in Figure 1.2, the Compton process is dominant in the therapeutic energy range. Compton interactions will only be considered in this study and hence we assume that

$$ICF_p \simeq ICF_{p,Comp}, \quad (3.5)$$

and the primary Compton  $ICF$  will be the representative of the primary  $ICF$ . However,  $R$  given in Equation 3.4 remains the ratio of primary dose to the total dose resulting from all physical interactions.

### A. Electron production

- i) *Initial secondary electron fluence produced by monoenergetic photons*

Primary dose at a given point can be calculated by first estimating the fluence of secondary electrons at that point. Secondary electrons are the ones that emerge from the photon interaction site and their fluence is defined as the number of particles passing through a unit area perpendicular to the  $z$  direction (Figure 3.1). The energies of these electrons consist of a continuous spectrum and they can be grouped into discrete energy intervals. The product of electron fluence of a given energy interval with the corresponding stopping power yields the radiation dose deposited in that interval [56, 110, 100]. The primary dose is then the summation over all intervals and may be expressed as

$$D = \int_0^{E_{max}} \frac{S_c(E)}{\rho} \frac{d\phi_e(E)}{dE} dE \quad (3.6)$$

where  $S_c/\rho$  is the collisional mass stopping power and  $d\phi_e(E)/dE$  is the differential energy secondary electron fluence between  $E - \frac{dE}{2}$  and  $E + \frac{dE}{2}$  where  $E$  is a value in the range between  $E_{cut}$  and  $E_{max}$  (minimum kinetic energy cut-off value and maximum kinetic energy of secondary electrons).

Considering Compton interactions only, the amount of energy transferred to secondary electrons set in motion can be obtained from the Klein-Nishina differential energy cross sections [5, 50]. Given a photon fluence ( $\phi_p$ ) interacting in a layer of thickness  $dz$ , the initial differential electron fluence set in motion with energies between  $E - \frac{dE}{2}$  and  $E + \frac{dE}{2}$  (at the interaction site) is now calculated as

$$\frac{d\phi_{e,0}(z; E)}{dE} = \phi_p(z) \rho N_e \frac{d\sigma(h\nu, E)}{dE} dz \quad (3.7)$$

where  $\rho$  is the density of the medium and  $N_e$  is the corresponding number of electrons per unit mass. For primary dose calculation, the photon fluence

$\phi_p(z)$  decreases exponentially with depth and is given by

$$\phi_p(z) = \phi_p(0) \exp(-\rho N_e \sigma z) \quad (3.8)$$

where  $\phi_p(0)$  is the photon fluence entering the medium. If all types of photon interactions all allowed, the Compton cross section ( $\sigma$ ) should be replaced by the total cross section ( $\mu$ ) in Equation (3.7).

The Klein-Nishina term is given by [5, 50]

$$\frac{d\sigma(h\nu, E)}{dE} = \frac{3}{8} \frac{\sigma_0}{\alpha h\nu} \left\{ 2 - \frac{2E}{\alpha(h\nu - E)} + \frac{E^2}{\alpha^2(h\nu - E)^2} + \frac{E^2}{h\nu(h\nu - E)} \right\} \quad (3.9)$$

where  $\sigma_0 = 66.525 \times 10^{-30} m^2$  is the total cross-section for the Thomson classical scattering of a free electron. This expression is plotted in Figure 3.2 as dashed lines for monoenergetic photons of 1, 6 and 10 MeV where the electron kinetic energies range from  $E = 0$  to  $E = E_{max}$  where  $E_{max} = h\nu \cdot 2\alpha / (1 + 2\alpha)$  in which  $\alpha = h\nu / m_0 c^2$  ( $h\nu$  is the energy of the incident photons and  $m_0 c^2$  is the electron rest mass energy, 0.511 MeV).

### *ii) Initial secondary electron fluence produced by polyenergetic photons*

However, the photon beams produced by linacs are polyenergetic and to calculate the final dose one can follow two approaches. Assuming the photon spectrum emerging from the linac is known, we can calculate the dose response curve due to each photon energy interval in the spectrum and find the sum of all these curves weighted by the corresponding photon energy weight [49]. This approach is time consuming since accurate linac spectra contain a large number of photon energy intervals [71].

In our model, we propose to calculate a mean differential energy cross section for a photon spectrum. Given a photon distribution  $f(h\nu)$  and a differ-

ential energy cross section  $\frac{d\sigma(h\nu, E)}{dE}$ , the mean differential energy cross section for photon interaction resulting in electrons set into motion with energies between  $E - \frac{dE}{2}$  and  $E + \frac{dE}{2}$  is given by

$$\frac{d\bar{\sigma}(E)}{dE} = \frac{\int_0^{h\nu_{max}} f(h\nu) \frac{d\sigma(h\nu, E)}{dE} dh\nu}{\int_0^{h\nu_{max}} f(h\nu) dh\nu}. \quad (3.10)$$

For discrete photon spectra, the integration in Equation 3.9 is replaced by a weighted sum over all photon energy intervals of the spectrum.

On the other hand the attenuation of the polyenergetic photon fluence is still assumed exponential as in Equation 3.7. The linear attenuation coefficient resulting from Compton interactions of polyenergetic photons ( $\rho N_e \sigma(\bar{h\nu})$ ) is calculated at the mean energy of the photon spectrum ( $\bar{h\nu}$ ). These mean energies (along with the spectra) can be obtained from the literature [71] and  $\sigma$  is obtained by integrating Equation 3.9 over all electron energies to obtain

$$\sigma(\bar{h\nu}) = \frac{3}{4} \sigma_0 \left\{ \left( \frac{1+\alpha}{\alpha^2} \right) \left( \frac{2(1+\alpha)}{1+2\alpha} - \frac{\ln(1+2\alpha)}{\alpha} \right) + \frac{\ln(1+2\alpha)}{2\alpha} - \frac{1+3\alpha}{(1+2\alpha)^2} \right\}, \quad (3.11)$$

which is used in Equation 3.7. If in any given calculation primary Compton dose is to be evaluated while allowing all types of photon interactions,  $\sigma(\bar{h\nu})$  should be replaced by  $\mu(\bar{h\nu})$ . Tables for  $\mu(h\nu)$  are found in the litterature [50], and values for 6 MV and 18 MV spectra are listed in Table 3.1.

## B. Electron transport

### i) Pencil beam

The Fermi-Eyges equation [35] describes the lateral and angular distribution of charged particles undergoing multiple small angle elastic scattering

Table 3.1: The mass attenuation coefficient for polyenergetic photon beams ( $\mu/\rho$ ) is shown evaluated at the average photon energy of spectra.

	$\bar{h\nu}$ (MeV)	$\mu/\rho(\bar{h\nu})$ (cm <sup>2</sup> /g)	
		Water	Air
<b>6 MV</b>	1.92	0.051	0.046
<b>18 MV</b>	5.82	0.028	0.026

in passing through a layer of matter. The Fermi-Eyges theory is based on the assumption that the particles have not scattered to large angles, however, variations in the scattering properties of the medium with depth are accounted for.

First consider secondary electrons emerging from a photon interaction site with an angle  $\theta$  with respect to the incident photons. Then at the point  $(x, y, z)$  the location probability density is described as [48]

$$G(x, y, z; \theta, \phi) = \frac{1}{2\pi\sigma^2(z, \theta)} \exp - \frac{(x - \tan\theta_x z)^2 + (y - \tan\theta_y z)^2}{2\sigma^2(z, \theta)}, \quad (3.12)$$

where  $\sigma^2(z, \theta)$  is given by

$$\sigma^2(z) = \frac{1}{2} A_2(z) = \frac{1}{2} \int_0^z k(z')(z - z')^2 dz' \quad (3.13)$$

in which  $A_2(z)$  is the second moment of the linear scattering power and  $k(z)$  is the linear angular scattering power at depth  $z$  in the medium, and  $\theta_x$  and  $\theta_y$  are the projections of the polar angle  $\theta$  onto the X-Z and Y-Z planes. More

specifically these projections can be written as [48]

$$\begin{aligned} \tan\theta_x &= \tan\theta \cos\phi \\ \tan\theta_y &= \tan\theta \sin\phi, \end{aligned} \quad (3.14)$$

where  $\phi$  is the azimuthal angle. The analytical derivation of the scattering moments in homogeneous and inhomogeneous phantoms is given in Appendix A. Yu et al [110] have derived a set of recursion relations for the *zeroeth*, *first*, and *second* moments of the linear scattering power for a two-layer phantom. Appendix A gives a generalization of the *i*th moment in a *n*-layer phantom.

The spatial distribution at  $(x, y, z)$  due to electrons recoiling with an angle  $\theta$  over all  $\phi$  is found as

$$G(x, y, z; \theta) = \frac{\int_0^{2\pi} G(x, y, z; \theta, \phi) d\phi}{\int_0^{2\pi} d\phi}. \quad (3.15)$$

The solution to this integral was given by Wang et al [100]. Using the present notation, the spatial probability will be

$$G(x, y, z; \theta) = \frac{1}{2\pi\sigma^2(z, \theta)} \exp - \frac{x^2 + y^2}{2\sigma^2(z, \theta)} \cdot I_0 \left( \frac{2\sqrt{x^2 + y^2} z \tan\theta}{2\pi\sigma^2(z, \theta)} \right), \quad (3.16)$$

where  $I_0$  is the modified Bessel function of the first kind, of zero order. To reduce the number of variables, the energy-angle relationship for Compton interaction (Equation 1.2) is employed. Therefore, the secondary electron fluence at depth  $z$  for electrons originating between  $-\frac{dx}{2}$  and  $\frac{dx}{2}$ , and  $-\frac{dy}{2}$  and  $\frac{dy}{2}$  having energies between  $E - \frac{dE}{2}$  and  $E + \frac{dE}{2}$  will be the convolution of the initial electron fluence with the Fermi-Eyges Gaussian location density:

$$\frac{d\phi_e(x, y, z, E)}{dE} = \int_0^z \phi_p(z - z') \rho N_e \frac{d\sigma(E)}{dE} G(x, y, z - z'; E) dx dy dz'. \quad (3.17)$$

*ii) Broad beam*

First, we consider the case of a broad parallel photon beam with a field size  $[(-a, +a), (-b + b)]$  (Figure 3.1). To account for photons interacting across the field, we extend the above convolution to the  $x$  and  $y$  dimensions. Mathematically the secondary electron fluence will be given as

$$\frac{d\phi_e(x, y, z; E)}{dE} = \int_{-a}^{+a} \int_{-b}^{+b} \int_0^z \phi_p(z - z') \rho N_e \frac{d\sigma(E)}{dE} G(x - x', y - y', z - z'; E) dz' dy' dx', \quad (3.18)$$

and hence the primary Compton dose can be written as

$$D(x, y, z) = \int_0^{E_{max}} \int_{-a}^{+a} \int_{-b}^{+b} \int_0^z \frac{S_c(E)}{\rho} \phi_p(z - z') \rho N_e \frac{d\sigma(E)}{dE} G(x - x', y - y', z - z'; E) dz' dy' dx' dE. \quad (3.19)$$

The evaluation of the above 4-dimentional integral in Equation 3.14 is a formidable task, and we have to resolve to making some approximations. First, based on Figure 1.1 it is safe to assume that secondary electrons emerge in the forward direction from the interaction site. This makes the angle  $\theta$  equal to *zero* in Equation 3.11 and the location density purely Gaussian. This approximation will be quantified in the Results Section. Second, if we only consider a layered phantom as in Figure 3.1 the initial secondary electron fluence at a depth  $z$  will be spatially invariant. Thus, the above integral can be evaluated explicitly over the lateral dimensions  $x'$  and  $y'$ , and this yields an error function (*erf*). The resulting form of the dose function is a 2-dimensional integral over the depth  $z$  and the initial secondary electron energy  $E$ :

$$D(x, y, z) = \int_0^{E_{max}} \int_0^z \frac{\lambda S_c(E)}{4 \rho} \left\{ \text{erf}\left(\frac{x - a}{\sigma^2(z - z')} + \text{erf}\left(\frac{x + a}{\sigma^2(z - z')}\right)\right) \right. \\ \left. \left\{ \text{erf}\left(\frac{x - b}{\sigma^2(z - z')}\right) + \text{erf}\left(\frac{x + b}{\sigma^2(z - z')}\right) \right\} \phi_p(z - z') \rho N_e \frac{d\sigma(E)}{dE} dz' dE. \quad (3.20) \right.$$

Following the "photon-electron cascade model" [110] in dealing with energy straggling, a parameter ( $\lambda$ ) was used in Equation 3.20 for electrons crossing an interface between dissimilar media.  $\lambda$  accounts for the loss of electrons and represents the ratio of the number of electrons exiting the layer of water to the number entering the air gap.

Equation 3.20 may be expressed in the form of a numerical summation over all energy intervals and over all depths to calculate the dose deposited at that point. Only secondary electrons which have kinetic energies greater than a cut-off energy ( $E_{cut} = 10keV$ ) are transported and below  $E_{cut}$  their energy is considered to be deposited at the spot.

The above derivation of Compton primary dose is specific to a parallel incident photon beam (infinite source to surface distance, SSD). To obtain the absorbed dose due to a diverging photon beam (finite source to surface distance), a converging factor involving inverse square law is applied [104]. This conversion can be stated as

$$D(x, y, z) = \left[ \frac{SSD}{z + SSD} \right]^2 \cdot D_\infty \left( \frac{x \cdot SSD}{z + SSD}, \frac{y \cdot SSD}{z + SSD}, z \right), \quad (3.21)$$

where  $D_\infty$  is the depth dose for the infinite SSD or broad parallel photon beam setup evaluated at the arguments inside the brackets. In our method we are not calculating the total dose but rather a correction factor to be applied to the dose in the equivalent homogeneous phantom. Hence, primary Compton dose in the homogeneous and inhomogeneous cases are calculated simultaneously to do the proper normalization.

## II. Scatter inhomogeneity correction factor

Because of the long range of secondary electrons emerging from the primary interaction site (several centimeters for megavoltage energies), a detailed electron transport model was included, as discussed in the previous section, to account for perturbations resulting from phantom inhomogeneities. Further interactions of scattered radiation result in secondary electrons of much smaller range which can be considered to deposit their energy at the point of creation. This allows the use of approximate methods to correct for the scatter dose distribution.

The "equivalent" tissue-air ratio method [95] attempts to correct for primary dose in a inhomogeneous medium through the use scaling to a water equivalent depth and the scatter dose through the scaling of the field size (Equation 1.14). For a scatter inhomogeneity correction factor, we propose the use of tissue-air ratios evaluated at the same depth in both homogeneous and inhomogeneous phantoms but using a scaled field size for the inhomogeneous phantom as follows:

$$ICF_s(z, r) = \frac{TAR(z, r')}{TAR(z, r)}, \quad (3.22)$$

where  $r'$  is the effective beam radius defined by

$$r' = r\rho' \quad (3.23)$$

$$\rho' = \sum_{i,j,k} W_{ijk} \rho_{ijk} / \sum_{i,j,k} W_{ijk}, \quad (3.24)$$

and the beam radius  $r$  of a circular field is equivalent to the side of a square field  $s$  by [56]

$$r = \frac{s}{\sqrt{\pi}}. \quad (3.25)$$

Instead of implementing Equations 3.22 and 3.23 for the calculation of the effective beam radius at every point, we used results given by the "equivalent" tissue-air ratio method (*ETAR*) to extract these values. Denoting the *ETAR* correction method as  $ICF_{ETAR}$  and following its definition in Section 1.4.1 Equation 1.14, we can state that

$$TAR(z', r') = ICF_{ETAR}(z, r).TAR(z, r). \quad (3.26)$$

$ICF_{ETAR}(z, r)$  is calculated from the treatment planning system (Figures 2.5 and 2.6). Then the effective beam radius ( $r'$ ) corresponding to  $TAR(z', r')$  at water equivalent depth ( $z'$ ) is found from the *TAR* tables. The use of tissue-maximum ratios (*TMRs*) instead of tissue-air ratios (*TARs*) is recommended in Equations 3.27 (see sections 1.4.2 and 1.6.1). *TMR* tables are generated by the treatment planning system based on measured percentage depth doses (*PDDs*) in water. The *TMRs* for our 6 *MV* beam are given in Table 3.2.

For example, for a water phantom containing an air cavity between 3 *cm* and 8 *cm* if one needs to calculate  $r'$  at 11 *cm* depth for a 6 *MV* beam and 10x10 *cm*<sup>2</sup> field size, the following procedure is recommended. First, the value of *TMR* in the inhomogeneous phantom at 11 *cm* depth is found from Equation 3.26 (0.867). The water equivalent depth ( $z'$ ) at 11 *cm* is  $\simeq 6$  *cm* (3 + 5x0.001+ 3). In order to extract the effective beam radius from the *TMR* table a search algorithm is invoked and interpolation between the data values is used. So, the search will be in the 6 *cm* depth row and a value for the equivalent beam radius is found for a *TMR* of 0.867. In this example, the effective beam radius is 2.42 *cm* or 4.3x4.3 *cm*<sup>2</sup> square field. This value is then used in Equation 3.22 and the scatter inhomogeneity correction factor ( $ICF_s$ ) is derived at that depth.

Table 3.2: Cadplan *TMR* table for 6 MV beam is shown as a function of depth and field size. The 0x0 cm<sup>2</sup> *TMR* are extrapolation from higher field size values.

Field size (cm <sup>2</sup> )	0x0	3x3	5x5	10x10	15x15	20x20
Depth (cm)						
0	0.111	0.146	0.169	0.225	0.279	0.324
1	0.963	0.960	0.959	0.962	0.968	0.979
1.5	1.000	1.000	1.000	1.000	1.000	1.000
2	0.996	0.999	1.000	1.000	0.997	0.999
3	0.950	0.965	0.972	0.978	0.978	0.982
4	0.930	0.933	0.939	0.952	0.957	0.962
5	0.872	0.894	0.907	0.925	0.933	0.939
6	0.837	0.858	0.873	0.898	0.911	0.918
8	0.754	0.785	0.806	0.842	0.860	0.871
10	0.675	0.717	0.743	0.786	0.808	0.822
12	0.615	0.657	0.684	0.729	0.756	0.773
14	0.551	0.598	0.627	0.676	0.706	0.726
16	0.513	0.550	0.575	0.625	0.659	0.679
18	0.462	0.503	0.530	0.577	0.611	0.633
20	0.422	0.461	0.486	0.534	0.567	0.590

As can be seen from the above formulation, the proposed scatter correction method resembles the *ETAR* method. In fact, a mathematical relationship can be drawn between the two which makes this method easily implemented on treatment planning systems that provide *ETAR* correction. Thus, the proposed  $ICF_s$  can be stated as

$$ICF_s(z, r) = ICF_{ETAR}(z, r) \cdot \frac{TAR(z, r')}{TAR(z', r')}, \quad (3.27)$$

where  $z'$  is the water equivalent depth (radiological depth) and  $r'$  is given as above (Equation 3.23).

### 3.2.2 Monte Carlo simulation

Monte Carlo simulation was performed using the *EGS4* [76] Monte Carlo code with default values for the Parameter Reduced Electron Step Algorithm (*PRESTA*) [15]. Primary Compton dose was scored after determining the interaction type and terminating the photon history [81]. Total dose was also simulated using the code *DOSXYZ* [65]. *AE* was set to  $0.521\text{ MeV}$ , *AP* to  $0.01\text{ MeV}$ , *ECUT* to  $0.521\text{ MeV}$  and *PCUT* to  $0.01\text{ MeV}$ . Restricted stopping powers were employed in these calculations, and delta-rays ( $\delta - rays$ ) were allowed to be produced above a  $10\text{ keV}$  threshold of kinetic energy. The use of unrestricted stopping powers with no account of  $\delta - rays$  in our calculation and restricted stopping powers and  $\delta - ray$  production in the Monte Carlo simulation needed to be tested. Monodirectional incident photons with energies ranging from  $1$  to  $20\text{ MeV}$  were transported through the water and the water-air-water phantoms, and the subsequent energy deposited was recorded in a Cartesian array of  $0.2 \times 0.2 \times 0.2\text{ cm}^3$  voxels. For photon beams, published spectra of  $6$  and  $18\text{ MV}$  were used [71, 99]. Radiation beam sizes considered were  $5 \times 5\text{ cm}^2$  and  $10 \times 10\text{ cm}^2$ . At least 100 million incident photons were used for simulation giving a relative error of less than  $2\%$  on the scored dose.

### 3.2.3 Experiments

Irradiations were performed with  $6\text{ MV}$  and  $18\text{ MV}$  x-rays as described in Chapter 2. Radiation field sizes of  $5 \times 5\text{ cm}^2$  and  $10 \times 10\text{ cm}^2$  at a source to axis distance (SAD) of  $100\text{ cm}$  was used. The air gap was set to  $5\text{ cm}$  with  $3\text{ cm}$  polystyrene supported by side walls (much larger than the field size) above

the air gap [93]. The *ICF* at a given depth was calculated as the ratio of the measured dose in the inhomogeneous phantom to the measured dose in the homogeneous phantom at the same corresponding depth.

### 3.3 Results and Discussion

#### 3.3.1 Calculated primary Compton dose compared to Monte Carlo simulation

In this section we present the effects of the different assumptions made in the development of our primary inhomogeneity correction factor method. Furthermore, we present a comparison of three-dimensional dose distributions calculated with our analytical method to those calculated with Monte Carlo simulation. In Figure 3.2 is shown the differential energy cross sections used in the calculation of monoenergetic primary Compton dose distributions. The differential energy cross sections for 6 and 10 *MV* spectra [71] that are also shown are based on Equation 3.9. As Figure 3.2 demonstrates, for polyenergetic photon beams the differential electron fluence decreases with increasing electron energy owing to the lower weight of high energy photons in these linac spectra [71, 99], and therefore less high energy electrons. Our method is very promising since the computation time for a given photon beam is equivalent to the one for monoenergetic photons having an energy of  $h\nu_{max}$  (maximum energy in the photon spectrum). For instance, the calculation of primary dose distribution due to 10 *MeV* photons takes exactly the same computation time as for a 10 *MV* photon beam.

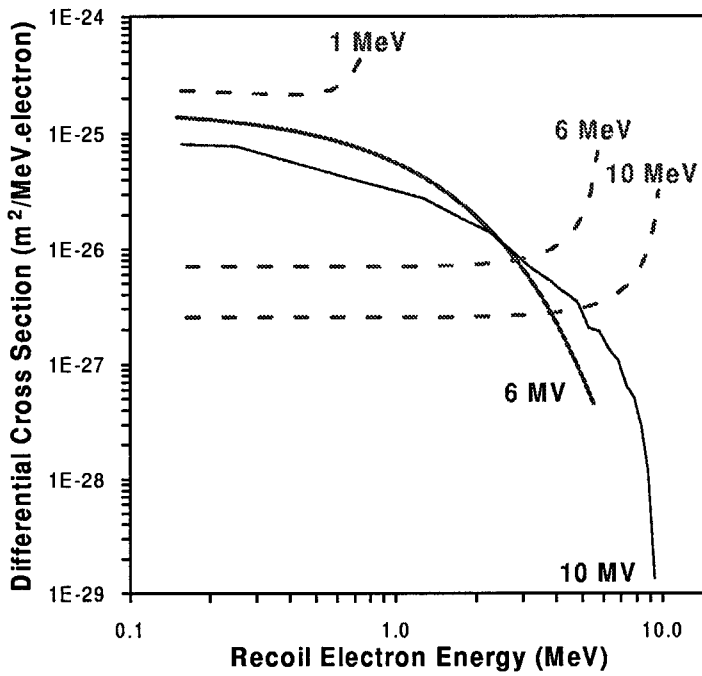


Figure 3.2: The Klein-Nishina differential energy cross sections are shown for 1, 6 and 10 MeV monoenergetic photons and the derived cross sections for the 6 and 10 MV photon spectrum are also included.

Absolute primary dose, derived according to Equation 3.18 in which secondary electron recoil in all directions based on Compton effect, is compared to absolute primary dose using forward directed electrons assumption. The results are shown in Figure 3.3 for 6 MeV photons. The dose distribution for forward directed electron assumption is achieved by setting  $\theta$  to *zero* in Equation 3.11. An agreement to within 2% is seen between the two dose distribution curves. The all-direction assumption curve is slightly higher in the buildup region and slightly lower beyond  $d_{max}$  which is expected due to smaller depth attained by secondary electrons travelling initially with an angle  $\theta$  with respect to the  $z$  direction. It is helpful to point out that the effect of *nonzero*  $\theta$  in the dose distribution is less seen with higher photon energies as

illustrated by Figure 1.1.

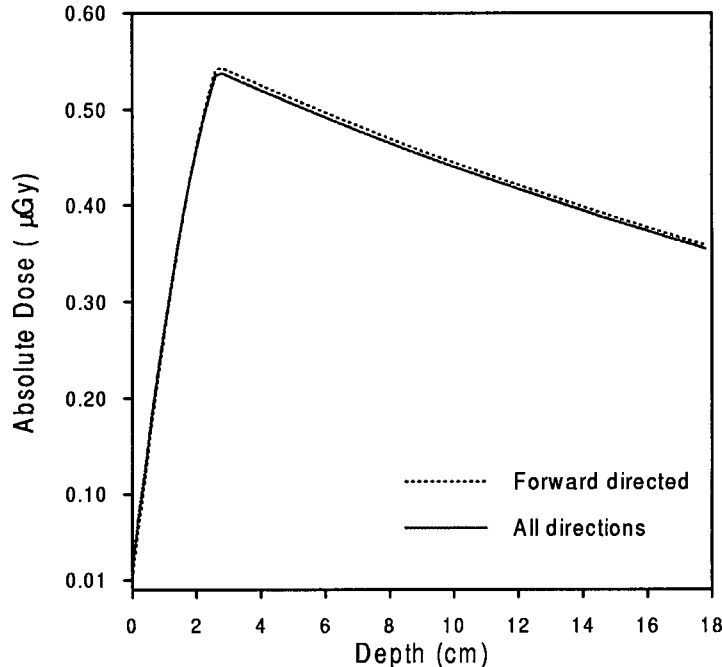


Figure 3.3: 6 MeV photon primary dose calculated with forward directed electrons is compared to dose calculated including electron recoil in all directions.

The use of unrestricted stopping powers without  $\delta - ray$  production in our calculations was investigated, and the results of comparison with Monte Carlo are depicted in Figure 3.4. In this Figure, the dose curve of 20 MeV photons calculated using Monte Carlo simulation is shown under two conditions; using restricted stopping powers with and without  $\delta - ray$  production. Similarly, in our analytical calculations, restricted and unrestricted stopping powers, taken from ICRU35 [79], were used and compared to Monte Carlo results. As can be seen, there is good agreement between the analytical primary dose calculation and Monte Carlo simulation when considering restricted stopping powers without  $\delta - ray$  production. Meaning that if we remove the

*delta-ray* production assumption, our theoretical calculations were successful in accounting for dose distribution. Furthermore, allowing  $\delta$ -ray production to take place in the Monte Carlo simulation can be accounted for by the use of unrestricted stopping powers in our theoretical calculation and still good agreement is maintained. The discrepancy between theory and Monte Carlo seen in the maximum depth region is due to the energy loss model employed in our calculation which is based on Harder's equation [41] (see Appendix A). This equation, which gives a linear relationship between the mean energy of electrons and depth of penetration, is only accurate in the two third range of electrons [79]. Beyond this depth this linear relationship is known to underestimate the mean energy [40, 79], and hence a lower dose is expected to be seen near the end of the electron range. It is worth to point out that the 20 MeV monoenergetic photon case chosen to illustrate the effect of  $\delta$ -rays is an extreme case; however, the validity of using the unrestricted stopping powers was well demonstrated.

Making the above assumptions in our calculations, analytically calculated primary Compton dose distribution are compared to Monte Carlo simulation for mono- and polyenergetic photon beams. Homogeneous and inhomogeneous phantoms were considered with a 5 cm air gap situated between 3 cm and 8 cm depth. The primary Compton dose was calculated according to Equations 3.6 and 3.19. Figures 3.5(a) and (c) show good agreement between the analytically calculated and the Monte Carlo simulated homogeneous and inhomogeneous *absolute* primary Compton dose for both 6 MeV and 20 MeV monoenergetic photon beams with a 5x5 cm<sup>2</sup> field size as a function of depth. The 20 MeV curve deserves special attention; it shows the primary dose distribution in the presence of an air cavity right in the middle of the build up

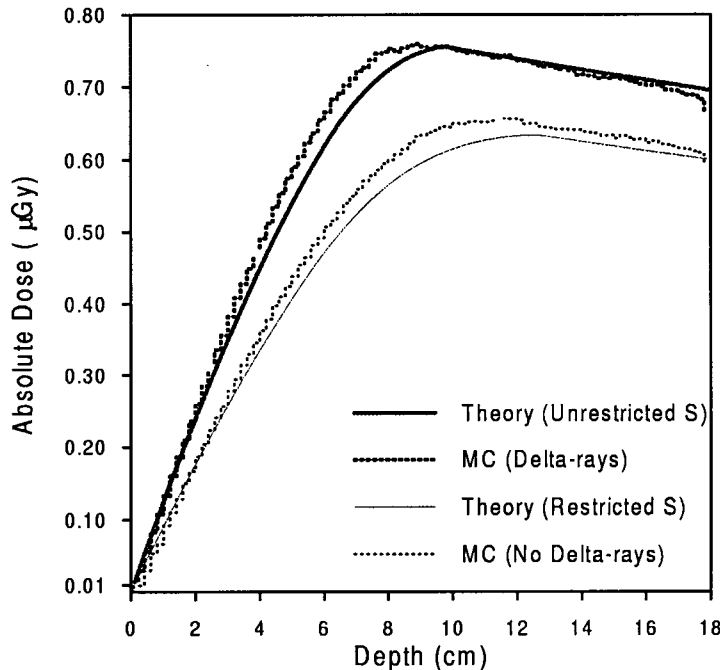


Figure 3.4: Examining delta ray production effect using Monte Carlo simulation compared with analytical calculations. The upper two curves show that  $\delta$ -ray production can be accounted for in our analytical calculations by using unrestricted stopping powers.

region. The usefulness of our model can be seen in this difficult case. No normalization has been made in this case and the values are per million photons entering the medium. Accurate estimation of the interface dose requires such an agreement especially at the distal end of the air gap. At the distal end of the air gap the second interface acts as another surface and the buildup curve repeats itself starting from a background level that is dependent on the air gap depth and beam energy.

Lateral dose profiles taken at a depth of 4 cm (inside the air gap in the inhomogeneous phantom) are compared with Monte Carlo simulations and

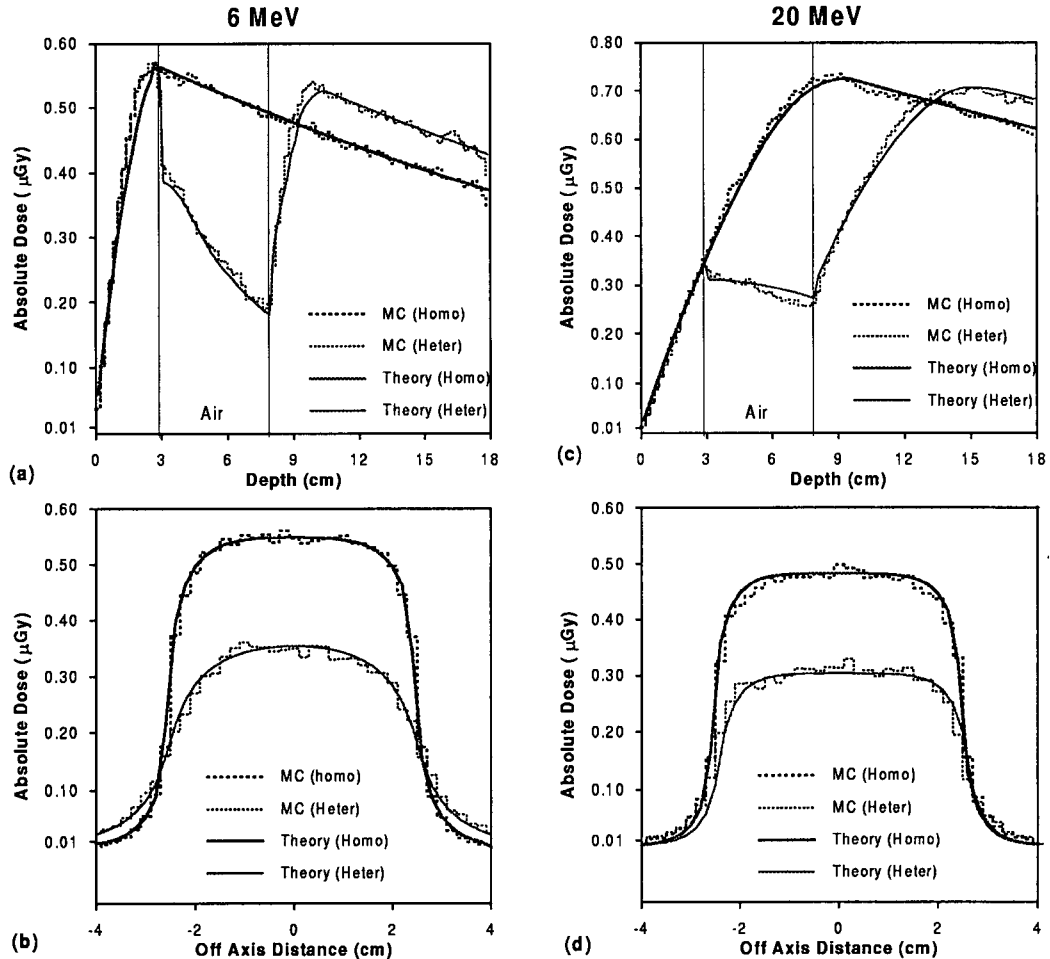


Figure 3.5: A comparison of primary Compton dose derived from theory and Monte Carlo simulations for a  $5 \times 5 \text{ cm}^2$  parallel beam of 6 and 20 MeV monoenergetic photons incident on homogeneous and inhomogeneous phantoms: (a, c) variation of absolute dose with depth, (b, d) lateral absolute dose profiles at 4 cm depth. The absolute dose shown is per million photons.

excellent agreement was seen even in the penumbral regions (Figures 3.5(*b*) and (*d*)). The Fermi-Eyges theory is derived from the Boltzmann-Fokker-Plank equation using a small angle scattering approximation. It is known to underestimate scattering of electrons in the forward region and overestimate it at large angles [79]. The results presented in Figures 3.5 support the use of this simple theory to describe the secondary electron scattering distribution.

A similarly good agreement between primary Compton depth dose calculations and Monte Carlo simulation is demonstrated in Figures 3.6(*a*) and (*c*) for polyenergetic 6 *MV* and 18 *MV* photon beams. Profiles taken at 4 *cm* in both homogeneous and inhomogeneous phantoms were also compared and agree well as shown in Figures 3.6(*b*) and (*d*). This good agreement validates our approaches of weighting the differential energy spectra of electrons by the corresponding polyenergetic photon spectrum (Equation (3.10)).

For polyenergetic photon beams, a broad maximum dose region with a steep rise in the buildup region was as observed in the calculated depth dose. Furthermore, the descending portion of the primary Compton depth dose was well reproduced by our calculation showing that the use of a linear attenuation coefficient ( $\frac{\mu(\bar{h}\nu)}{\rho}$ ) evaluated at the mean energy of the photon spectrum ( $\bar{h}\nu$ ) and used in Equation 3.7 is a good approximation.

In our calculations,  $\lambda$  representing the loss of electrons at interfaces had to be gradually changed empirically from 1 to 0.7 with increasing photon energies (1 *MeV* to 20 *MeV*). Table 3.2 shows the values of  $\lambda$  adopted for monoenergetic and polyenergetic cases in which good agreement with Monte Carlo simulation was observed. Using these values, we were able to explain the sudden drop in the dose value at the first dose bin inside the air cavity.

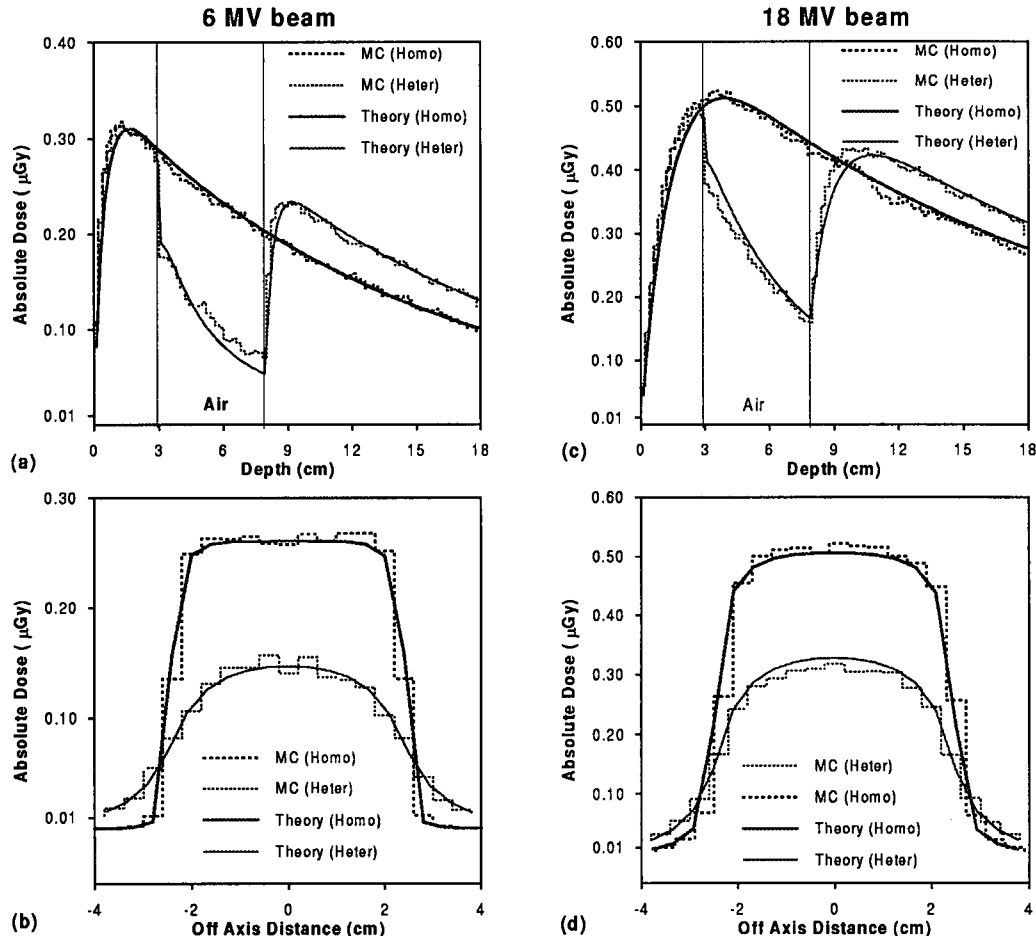


Figure 3.6: A comparison of primary Compton dose derived from theory and Monte Carlo simulations for a  $5 \times 5 \text{ cm}^2$  point source (100 cm SSD) of 6 and 18 MV photon spectra incident on homogeneous and inhomogeneous phantoms: (a, c) variation of absolute dose with depth, (b, d) lateral absolute dose profiles at 4 cm depth. The absolute dose shown is per million photons.

Moreover, these values were seen to be field size independent.

Table 3.3:  $\lambda$  is determined as a function of energy for both monoenergetic and polyenergetic beams.

	Monoenergetic		Polyenergetic	
	6 MeV	20 MeV	6 MV	18 MV
$\lambda$	0.80	0.90	0.75	0.85

Backscatter of electrons was not taken into account in our calculations although it can be characterized by a simple monoexponential function [110]. In the case of air gaps, backscatter is almost negligible as can be seen from the regions in the front and the distal end of gaps in the different Monte Carlo simulations. However, this effect may become more prominent for the case of high  $Z$  inhomogeneities which was discussed in the "photon-electron cascade model" [110] in which case more consideration is needed.

### 3.3.2 Scatter and total inhomogeneity correction factor and comparison with Monte Carlo simulation and experiments

It is well known that the magnitude of scatter dose is depth and field size dependent. For small field size ( $< 5 \times 5 \text{ cm}^2$ ), the scatter component is negli-

gible and it is safe to calculate the  $ICF$  based on primary dose only. In this Section, the effect of field size on the determination of  $ICF$  based on primary component will be studied, and solution to all field sizes encountered clinically will be presented.

#### A. Comparison of primary and total $ICF$ derived from Monte Carlo simulation

In Figure 3.7 is shown a comparison of the total dose deposited due to all types of interactions compared to the primary Compton dose of monoenergetic 6 MeV photon beams calculated by Monte Carlo simulation. The effect of varying the radiation field size from  $2 \times 2 \text{ cm}^2$  to  $10 \times 10 \text{ cm}^2$  is demonstrated. Also shown in this figure is the corresponding inhomogeneity correction factor ( $ICF$ ) derived from total dose and primary Compton dose scoring ((b) and (d)).

As can be seen from these figures the primary Compton dose constitutes a major component (up to 90 percent) of the total dose for small field size. The lower two panels in Figure 3.7 show that  $ICF$  and  $ICF_p$  are equivalent when the scatter dose over the primary dose ratio is negligible. In a sense, increasing the field size to  $10 \times 10 \text{ cm}^2$  however causes a maximum discrepancy in the order of 6.6% at 10.5 cm deep (Figure 3.7(d)). This results from the increase in magnitude of the scatter dose with respect to the  $2 \times 2 \text{ cm}^2$  irradiation field size.

For polyenergetic photon beams,  $ICF$  derived from primary Compton dose and total dose are presented in Figure 3.8 for the 6 MV and 18 MV photon beams. Figure 3.8 shows the effect of using  $2 \times 2 \text{ cm}^2$ ,  $4 \times 4 \text{ cm}^2$ , and

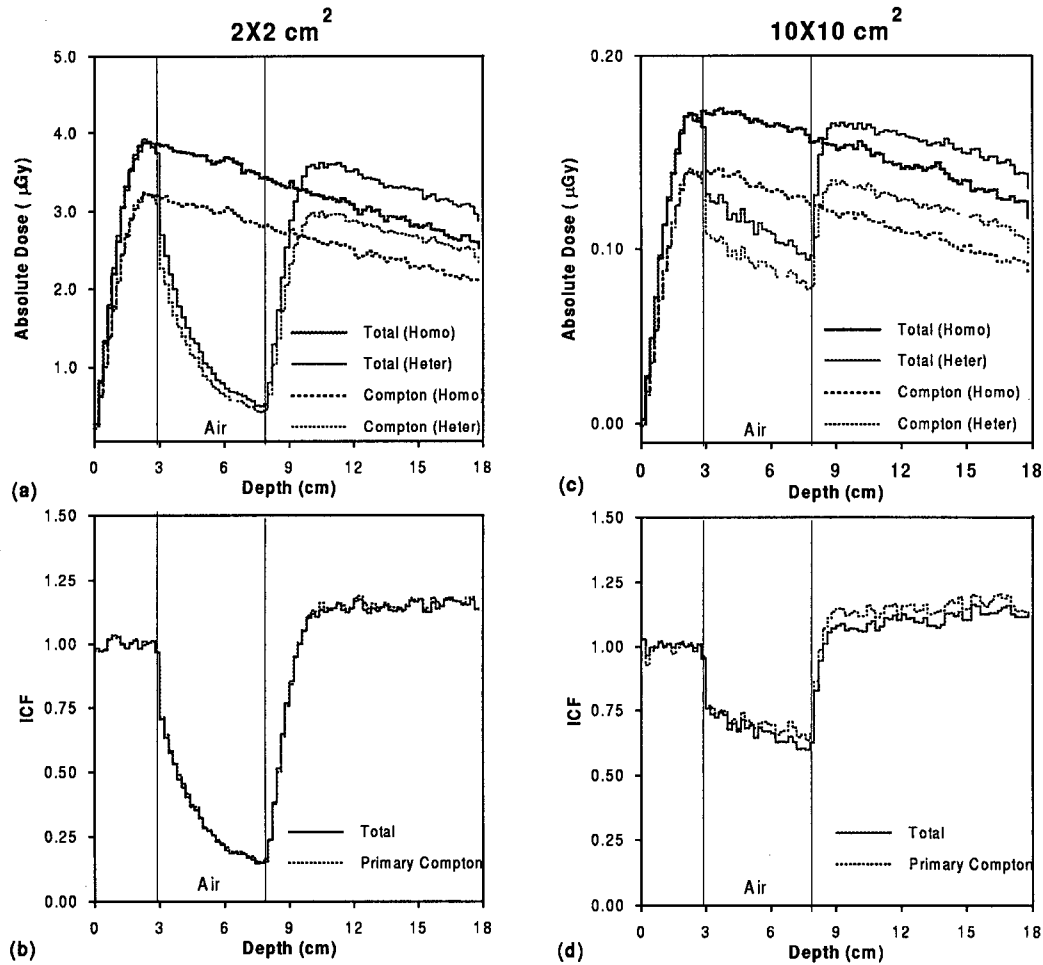


Figure 3.7: Total dose and primary Compton dose as determined by Monte Carlo simulation are shown for 6 MeV  $2 \times 2 \text{ cm}^2$  and  $10 \times 10 \text{ cm}^2$  irradiation field size in homogeneous and heterogeneous phantoms: (a, c) variation of absolute dose with depth, (b, d) Inhomogeneity Correction Factor derived from the 2 sets of curves of part (a) and (c) respectively.

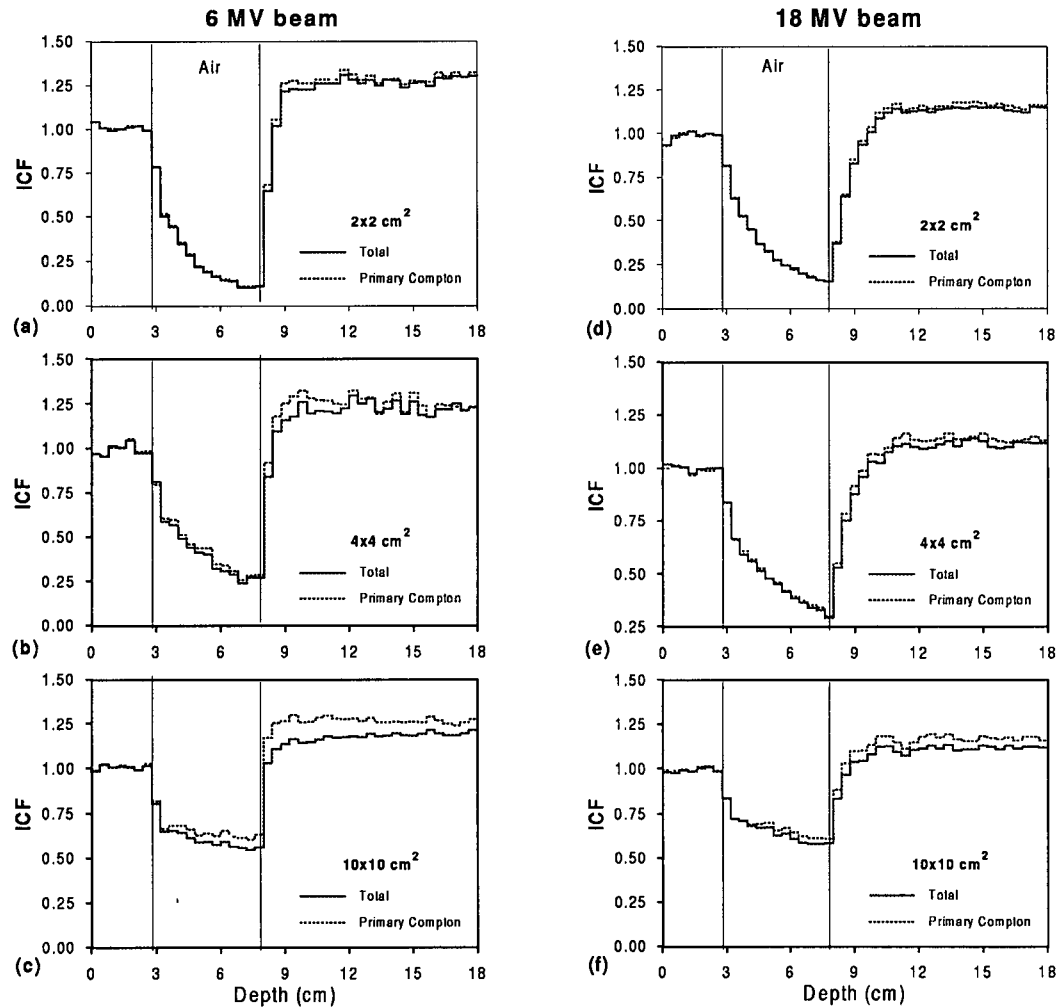


Figure 3.8: Inhomogeneity Correction Factor as determined by Monte Carlo simulation are shown for 6 MV and 18 MV polyenergetic photons: (a, b, c) 6 MV photon beam, and (d, e, f) 18 MV photon beam using field sizes as indicated in the legend.

$10 \times 10 \text{ cm}^2$  field sizes. This figure further demonstrates that primary Compton dose distribution gives a good approximation for the total dose distribution under certain conditions dictated by photon energy and field size (Figure 3.8(a,b,d,e)). Discrepancies of the order of 10% were seen between  $ICF_p$  and  $ICF$  for field size larger than  $5 \times 5 \text{ cm}^2$ . This points out to the need of including a scatter correction factor.

## B. Total inhomogeneity correction factor

To implement our scatter inhomogeneity correction factor method based on Equation 3.27,  $TMR$  curves as a function of depth were used for a number of field sizes and are shown in Figure 3.9. Curves of  $TMRs$  for field size smaller than  $3 \times 3 \text{ cm}^2$  are extrapolated by the treatment planning system.

Figure 3.10 shows the  $ICF_s$  for  $6 \text{ MV}$  and  $18 \text{ MV}$  beams in the presence of a  $5 \text{ cm}$  air cavity. Two field sizes were investigated ie  $5 \times 5 \text{ cm}^2$  and  $10 \times 10 \text{ cm}^2$ . The four curves in Figure 3.10 (a,c) predict a decrease in the scatter dose inside the air cavity and a buildup beyond the air/water interface as in the primary dose case. The lower two panels (Figure 3.10 (b,d)) depict the effective field radius  $r'$  as calculated by the treatment planning system, and extracted from the  $ICF_{ETAR}$  curve according to Equations 3.26. Based on Equation 3.25, the equivalent radius of a  $5 \times 5 \text{ cm}^2$  square field is  $2.8 \text{ cm}$ , and the equivalent radius for a  $10 \times 10 \text{ cm}^2$  square field is  $5.6 \text{ cm}$ . Considering the air cavity as being the inhomogeneity, we expect the effective field radius (Equation 3.23) to be smaller than the actual field radius. Indeed, this was seen in all cases studied in Figure 3.10. Inside the air cavity, the effective field radius was almost zero indicating a minimal contribution of scattered radiation to the dose in that region. Hence, a zero effective field radius is the limit of the current

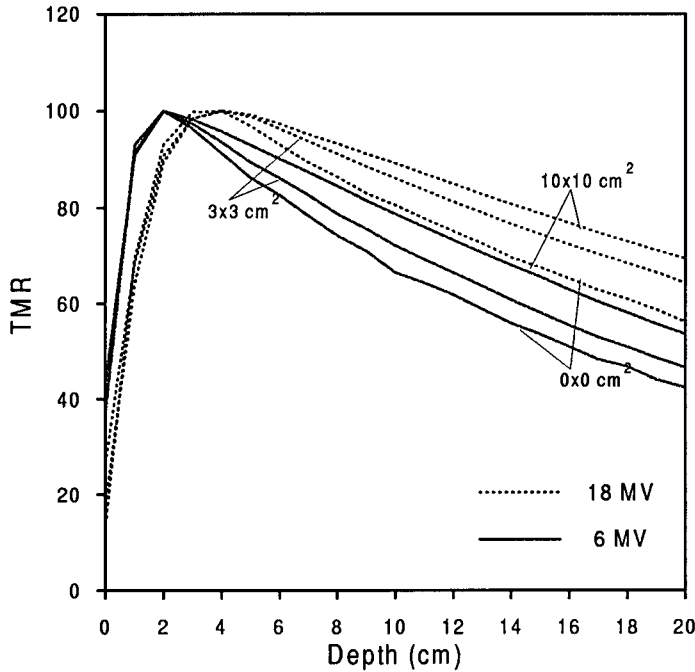


Figure 3.9: Cadplan TMR curves for 6 MV and 18 MV beams. Three field sizes,  $0 \times 0 \text{ cm}^2$ ,  $3 \times 3 \text{ cm}^2$  and  $10 \times 10 \text{ cm}^2$  are shown as a function of depth. The  $0 \times 0 \text{ cm}^2$  TMRs are extrapolation from higher field size curves.

scatter inhomogeneity correction factor method. Further improvement on the results requires an extensive scatter ray tracing calculations which lengthens considerably the computation time [105].

In combining the primary and scatter correction methods, it is required to know the relative dose contribution of the primary and scatter components (Equation 3.4). This ratio ( $R$ ) needs to be known in homogeneous water only and for each field size of interest. This made Monte Carlo simulation a perfect candidate since these simulations are to be done once and no further scaling is required. The ratio of primary dose (Compton and Pair production) over total dose ( $R$ ) is shown in Figure 3.9 for 6 MV and 18 MV using  $5 \times 5 \text{ cm}^2$

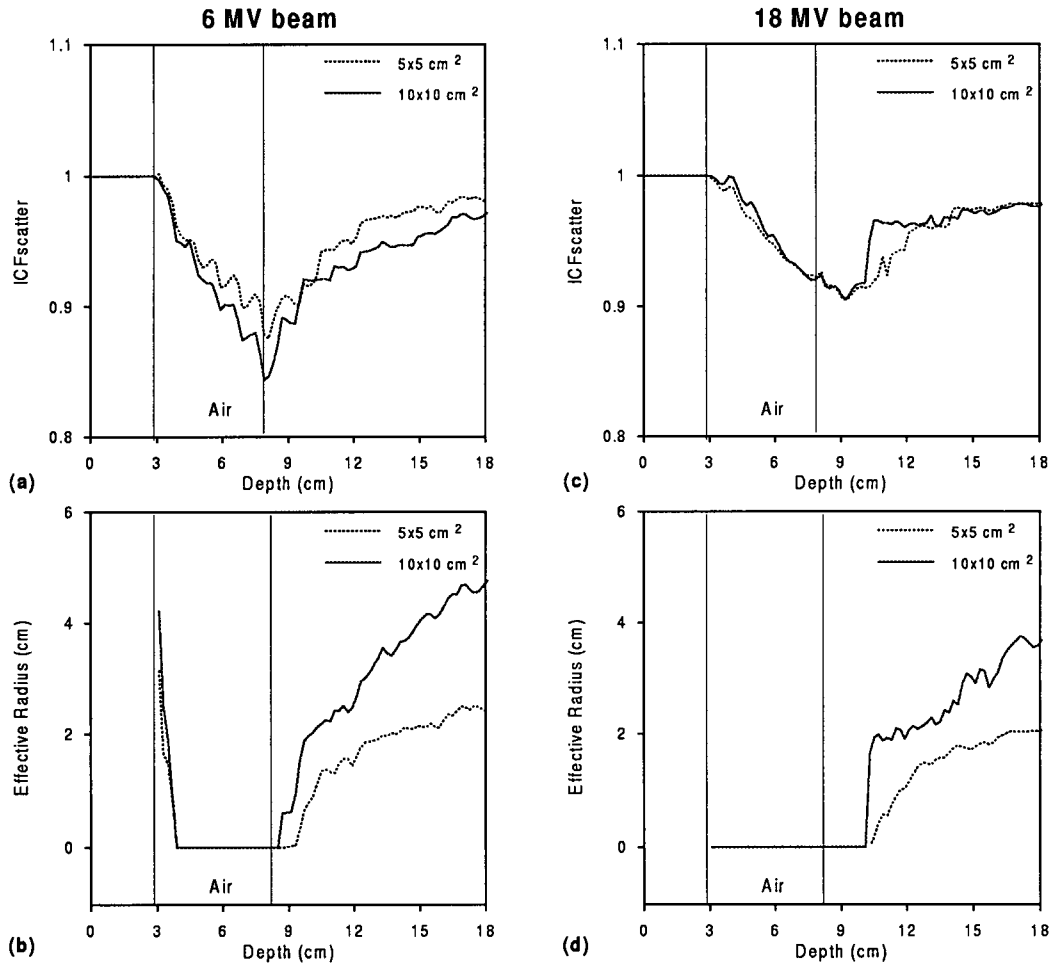


Figure 3.10: Scatter inhomogeneity correction factor ( $ICF_s$ ) and the corresponding effective beam radius derived for 6 MV and 18 MV beams using  $5 \times 5 \text{ cm}^2$  and  $10 \times 10 \text{ cm}^2$  irradiation field size in inhomogeneous phantoms: (a, c) variation of  $ICF_s$  with depth, (b, d) effective beam radius used for calculating the 2 sets of curves of part (a) and (c) respectively.

and  $10 \times 10 \text{ cm}^2$  field sizes. As it is expected, this ratio is higher in the smaller field cases.

An alternate method by which this ratio can be calculated is by using ratio of *TMRs*. *TMR* curve for  $0 \times 0 \text{ cm}^2$  has long been thought to represent the relative primary dose in water. However, obtaining this curve usually involves extrapolation which makes the  $0 \times 0 \text{ cm}^2$  field size *TMR* curve uncertain. Woo et al [107] has shown that for an  $18 \text{ MV}$  beam the extrapolated *zero* field *TMR* corresponds to the Monte Carlo calculated primary dose *TMR* for a field radius greater than  $2 \text{ cm}$ . Nevertheless, this validation remains to be conducted for each treatment planning system which might employ a different extrapolation technique. Thus, using Monte Carlo simulation to derive the ratio *R* is practical and sufficient.

In Figure 3.12 is shown the results of combining the primary and scatter correction factors based on Equation 3.4. The *ICF* is plotted as a function of depth for  $6 \text{ MV}$  and  $18 \text{ MV}$  beams using  $5 \times 5 \text{ cm}^2$  and  $10 \times 10 \text{ cm}^2$  field sizes. Measured *ICF* are plotted in the region beyond the air cavity. Monte Carlo results and their error bars are also shown which reflect the statistical fluctuation of these simulations. As stated above, the error achieved on the Monte Carlo dose distribution curve was within 2%. Hence, the error on the Monte Carlo derived *ICF* was within 4% (resulting from a ratio). *ICF*.

Therefore, our analytical calculations can predict the build up in the *ICF* curve seen by Monte Carlo simulation and experiments beyond a  $5 \text{ cm}$  air cavity. The agreement is within the statistical error or 4% of the Monte carlo results. This was shown for low and high energies ( $6 \text{ MV}$  and  $18 \text{ MV}$ ) and small and large field sizes ( $5 \times 5 \text{ cm}^2$  and  $10 \times 10 \text{ cm}^2$ ). Inside the air cavity

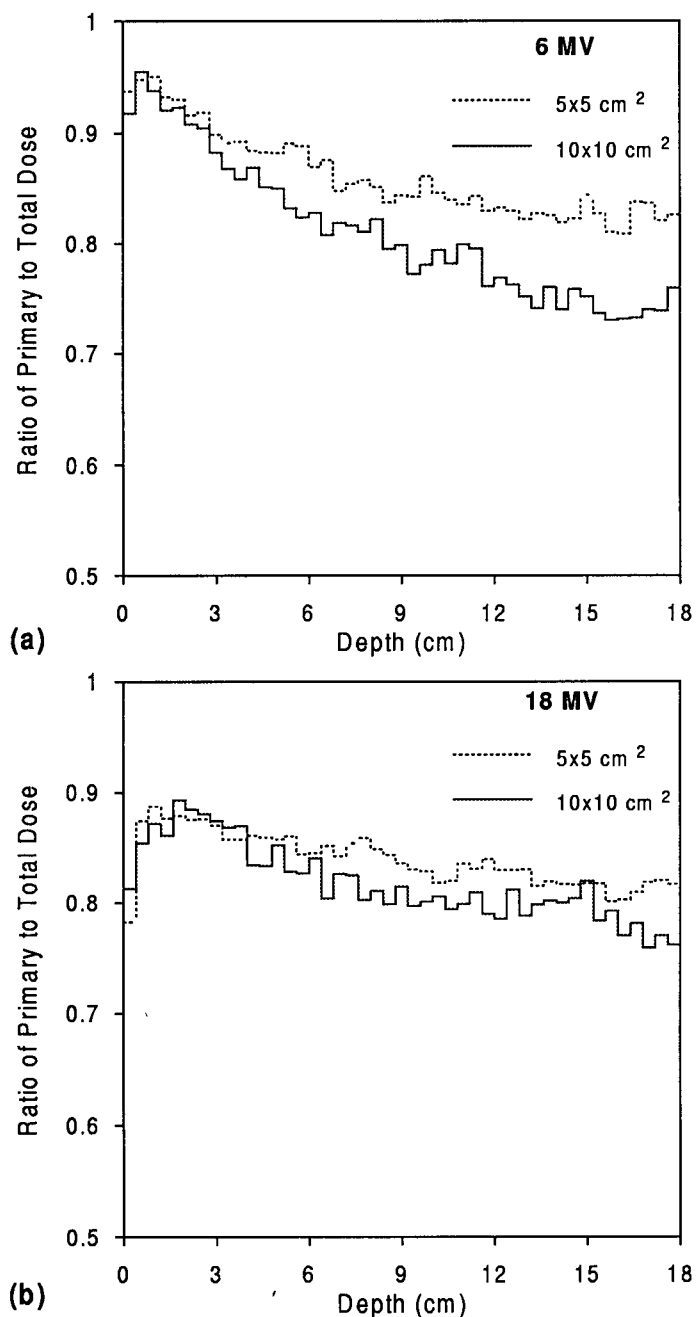


Figure 3.11: Ratio of primary dose to total dose as derived from Monte Carlo simulation using  $5 \times 5 \text{ cm}^2$  and  $10 \times 10 \text{ cm}^2$  irradiation field size in homogeneous water phantom: (a) 6 MV, (b) 18 MV.

there was good agreement seen in the case of the 6 MV beam; however, for the 18 MV beam the theoretical *ICF* was constantly higher than Monte Carlo results. Our primary dose comparisons (Section 3.3.1) indicated good agreement with Monte Carlo simulations. Therefore, the discrepancies inside the air cavity in Figure 3.12 (c and d) are due to the limitations of the proposed scatter inhomogeneity correction factor method. Hence, there is a need for modelling the transport of the secondary electrons set in motion by photons that have scattered at least once. Again, The region of interest lies beyond the air cavity, and the buildup effect shown by the Monte Carlo simulations and experiments was well reproduced by our analytical calculations. Although the calculation of *ICF* inside the air cavity represent extreme cases of clinical relevance, the physics behind our model and its limitations were demonstrated.

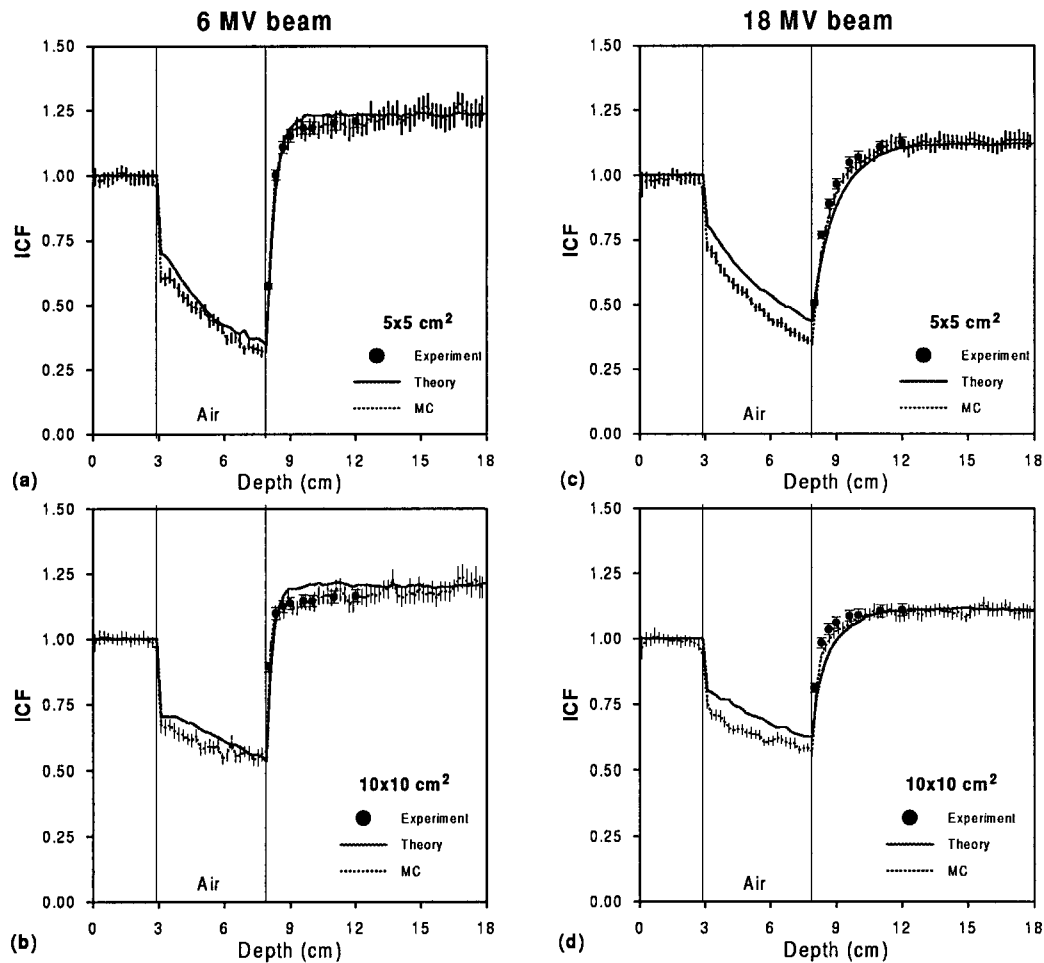


Figure 3.12: Inhomogeneity correction factor ( $ICF$ ) in the presence of 5 cm air cavity is derived from analytical calculation, Monte Carlo simulation and experiment as a function of depth. (a, b) 6 MV beam  $5 \times 5 \text{ cm}^2$  and  $10 \times 10 \text{ cm}^2$  irradiation field size, (c, d) 18 MV beam  $5 \times 5 \text{ cm}^2$  and  $10 \times 10 \text{ cm}^2$  irradiation field size.

### 3.3.3 Computation time

#### A. Inhomogeneity correction factor computation

In any given computational technique a general rule applies that the more accuracy required the more calculation time consumed. However, in the current approach due to the use of numerical evaluation of integrals, especially Equation 3.20, speed of calculation can be increased while accuracy is maintained. The use of the trapezoidal rule [84] in evaluating Equation 3.20 means dividing electrons into different energy intervals having width  $dE$  and origin depth interval  $dz$  and summing over all energies and depths. The time needed for such an integration depends on how large the intervals  $dE$  and  $dz$  are. To get an accurate answer,  $dE$  and  $dz$  should be as small as possible, however it turns out that the inhomogeneity correction factor or the ratio of primary Compton dose in the inhomogeneous phantom to the homogeneous case is independent of the choice of intervals.

Figure 3.13 depicts the depth dose for 20 MeV photons in water and in the inhomogeneous phantom containing 5 cm air cavity for two sets of values for  $dE$  and  $dz$  as explained in the legend. For "small" values of  $dE$  and  $dz$  we get an accurate absolute dose ditribution which compares well with Monte Carlo as seen in section 3.3.1. If these intervals were increased by a factor of hundred, an underestimation of dose in both phantoms is observed at all depths as shown in Figure 3.13(a). Nevertheless, if  $ICF_p$  is calculated for both sets of values, a remarkable argrreement is observed (Figure 3.13(b)). The calculation time for the "large" intervals were  $100^2$  shorter than the "small" intervals particular to this example.

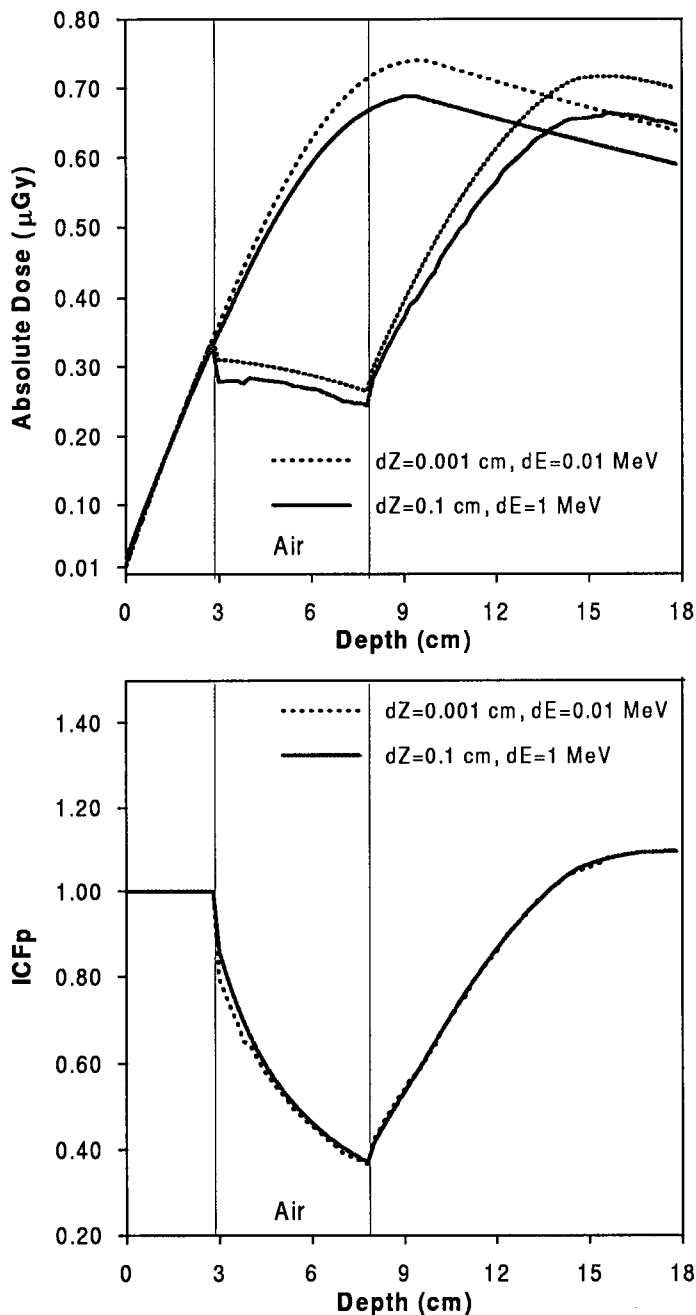


Figure 3.13: The effect of size of integration parameters ( $dE$  and  $dz$ ) on the primary dose and  $ICF_p$  distributions is shown. (a) Absolute primary dose for homogenous and inhomogenous case is plotted for "small" and "large" values of  $dE$  and  $dz$ . (b) the deduced  $ICF_p$  for both sets of values is shown.

Therefore, choosing the largest possible values for  $dE$  and  $dz$  gives the best time performance for primary dose calculation. In principle, the largest value for  $dE$  is  $E_{max}$ , and for  $dz$  is  $z$ , meaning that the limits of integration is divided into one interval for both variables. However, since there can exist inhomogeneities between the limits of integration of the  $z$  variable, the smallest dimensions of which is limited by the size of a voxel. Hence, the limiting value of  $dz$  is the  $z$  dimension of the voxel considered to be  $0.2\text{ cm}$  in our Monte Carlo simulation. For example, calculating the dose at a depth of  $4\text{ cm}$  requires dividing the range of integration into  $20\left(\frac{4}{0.2}\right)$  intervals. The size of intervals for the energy dimension ( $dE$ ) is not limited by the geometry of voxels, and the largest value that can be chosen is  $E_{max}$  indicating that the range of integration for the energy variable can be divided into one interval.

To find the error incurred from using "large" values of  $dz$  and  $dE$  an absolute percentage error is computed. The comparison is relative to  $ICF_p$  with "small"  $dz$  and  $dE$  ( $0.001\text{ cm}$  and  $0.01\text{ MeV}$ ). An average value for the percentage error over all points is calculated as

$$\bar{\epsilon} = \sum_z \frac{|ICF_{p,small} - ICF_p|}{ICF_{p,small}}. \quad (3.28)$$

Table 3.3 summarizes the calculation time needed to produce homogeneous and inhomogeneous three-dimentional dose grids based on the choice of  $dz$  and  $dE$ . As discussed earlier, the calculation time needed for a polyenergetic photon beam is the same as a monoenergetic beam having an energy equal to the maximum photon energy in the spectrum. As shown, the calculation times for the higher energy are considered to be practical in the clinic. It is recommended that the number of intervals of  $dE$  between the limits of

integration be kept equal or larger than 5 so the resulting error on the  $ICF_p$  (due to the evaluation of integrals) is within few percent.

Table 3.4: Computation time for 3D dose distribution for high and low photon energies for different choices of  $dE$ .  $dz$  was chosen to be  $0.2\text{ cm}$  which corresponds to the voxel size dimension. The first column ( $N_E$ ) indicates the number of intervals into which the range of integration is divided. The % error is relative to "small" values of  $dE$  in which  $N_E$  is set to 2000.

6 MeV or 6 MV				20 MeV or 20 MV		
<b><math>N_E</math></b>	<b><math>dE</math> (MeV)</b>	<b>Time (min)</b>	<b>% error</b>	<b><math>dE</math> (MeV)</b>	<b>Time (ms)</b>	<b>% error</b>
200	0.03	90.0	0.2	0.1	250.0	0.2
10	0.6	5.0	1.0	2.0	12.0	1.8
5	1.2	3.0	3.0	3.9	5.0	2.2

The above calculations are based on a  $5\times 5\text{ cm}^2$  field size, incident on a  $8\times 8\times 20\text{ cm}^3$  phantom with  $0.2\times 0.2\times 0.2\text{ cm}^3$  voxels. Technically, primary Compton dose was calculated at all centres of voxels ( $0.2\times 0.2\times 0.2\text{ cm}^3$ ) as considered in Monte Carlo simulation inside both phantoms. To cut down on computation time by a factor of two, calculations can be done every other voxel and interpolation can be employed between data points. Another approach is to increase frequency of calculation points in sensitive regions and decrease it in other places. It is worthwhile to point out that these timing studies were done on a  $266MHz$  Pentium PC running the *Linux* operating system. A faster CPU clock yields improved timing, and at least a factor of three (with a 700 MHz clock) can be achieved at the time of writing.

Yu et al [110] used a different approach in implementing his model. The calculation time on a VAX 8600 was estimated to be 12 *h* just for the primary dose component calculated in a similar phantom as above. On the other hand, a further advantage of the current model is due to the semi-empirical method proposed for calculating the scatter inhomogeneity correction factor ( $ICF_s$ ). The computation time for the scatter method is in the order of seconds on a UNIX platform. This outmatches the convolution/superposition method used by Yu et al for the calculation of the scatter component which requires considerably more execution time.

## B. Absolute primary Compton dose computation

In cases when there is an interest in calculating the absolute primary Compton dose with good accuracy rather than a correction factor, an optimization technique is proposed for the evaluation of the two-dimensional integral (Equation 3.20). Using again the trapezoidal rule, Equation 3.20 can be evaluated within 2% of accuracy when compared with the Monte Carlo method. This evaluation, as presented in Figure 3.5(c) and Figure 3.11(a) considering 20 *MeV* photons for example, was achieved using "small" values for  $dz$  and  $dE$ . This led to long computation times (on the order of hours) as can be extrapolated from Table 3.3.

To be able to see the effect of changing the value of  $dz$  or  $dE$  on the magnitude of dose, absolute primary Compton dose was evaluated at (0,0,4) (4 *cm* deep along the central axis) as a function of different combination values of  $dz$  and  $dE$ . In Figure 3.14 is shown the effect of varying  $dz$  while keeping  $dE$  "small" and varying  $dE$  while keeping  $dz$  "small". The behaviour of these curves can be anticipated since the trapezoidal rule gives an error to the order

of  $1/N^2$ , where  $N$  is the number of intervals considered between the limits of intergration [84]. Since the length of interval is inversely proportional to the number of intervals, for instance,

$$dz = \frac{z}{N_z} \quad (3.29)$$

$$dE = \frac{E_{max}}{N_E}, \quad (3.30)$$

it is clear that the error involved from increasing  $dz$  and  $dE$  will be to the order of  $dz^2$  and  $dE^2$  respectively. Hence, the absolute primary Compton dose varies as second order polynomial function of  $dE$  when  $dz$  is "small" or  $dE$  when  $dE$  is "small". Thus,

$$D(dz|_{dE}) = a_1 dz^2 + b_1 dz + c_1 \quad (3.31)$$

$$D(dE|_{dz}) = a_2 dE^2 + b_2 dE + c_2. \quad (3.32)$$

In Figure 3.14 is also shown Equations 3.31 and 3.32 fitted to the dose curves. The estimates of the paramaters  $a$ ,  $b$  and  $c$  are given in Table 3.4. One thing to note is that the error originating from increasing  $dz$  or  $dE$  is obviously  $D(dz|_{dE}) - c_1$  or  $D(dE|_{dz}) - c_2$ . The advantange seen from these errors is that they are of opposite signs and similar tendency. A fortunate situation is to be achieved when both errors cancel out and an accurate dose value can be found that is independent of the choice of intervals ( $dz$  and  $dE$ ). In fact, rearranging Equations 3.31 and 3.32 and setting the sum of errors to zero, a relationship between  $dz$  and  $dE$  can be obtained:

$$a_1 dz^2 + b_1 dz + a_2 dE^2 + b_2 dE = 0, \quad (3.33)$$

which is a quadratic equation, and  $dE$  solution can be given as

$$dE = \frac{-b_2 + \sqrt{b_2^2 - 4a_2(a_1 dz^2 + b_1 dz)}}{2a_2}. \quad (3.34)$$

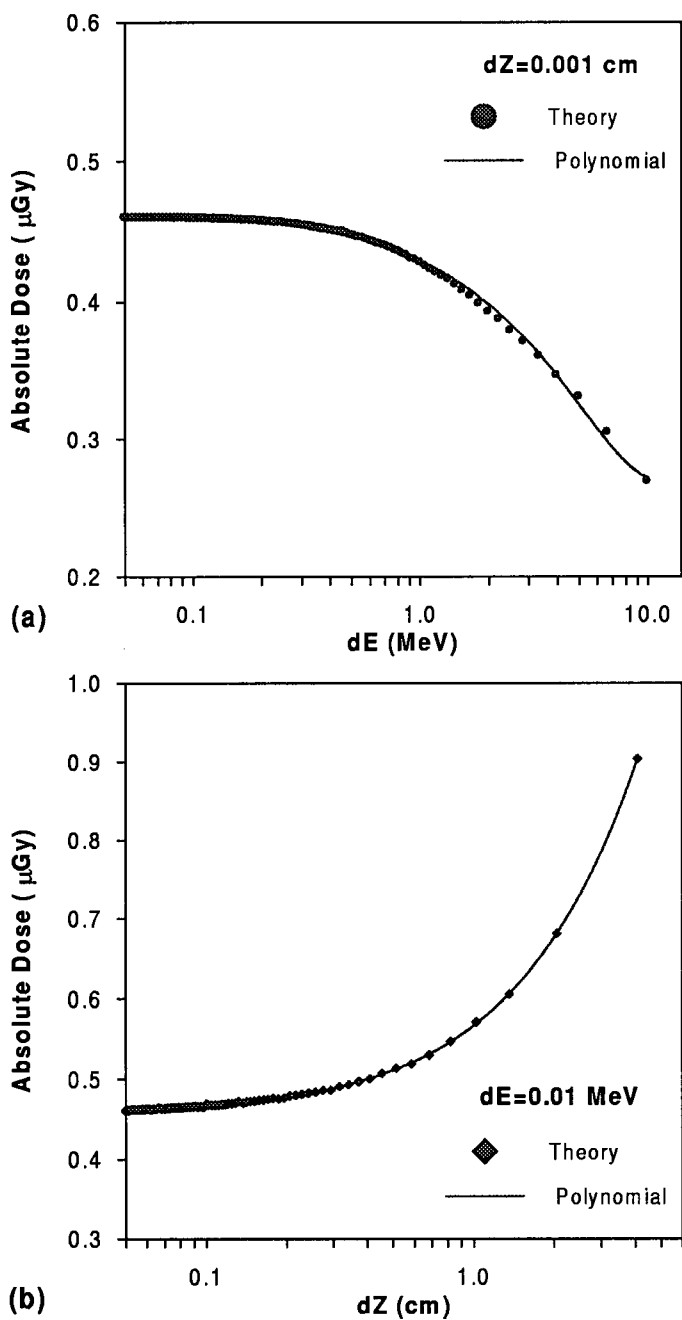


Figure 3.14: Variation of the primary Compton dose value at (0,0,4) is shown as a function of integration interval size. (a) Dose versus  $dE$  is plotted for a constant  $dZ$ , (b) Dose versus  $dZ$  for a constant  $dE$ .

Based on this optimized choice of  $dE$  (Equation 3.34) the primary Compton dose at (0,0,4) was evaluated as a function of  $dz$ . In Figure 3.15 is shown an almost flat curve that is independent of  $dz$  as long as  $dE$  follows Equation 3.34. This technique results in a saving in computation time as was seen in the previous section, however, accuracy is maintained not only for  $ICF_p$  distribution but also for absolute primary Compton dose distribution.

Table 3.5: Best estimate of parameters in Equations 3.31 and 3.32 was derived based on the Least-squares fitting method.

	<b>a</b>	<b>b</b>	<b>c</b>
$D(dZ)$	$-2.71 \times 10^{-10}$	$1.10 \times 10^{-7}$	$4.56 \times 10^{-7}$
$D(dE)$	$1.70 \times 10^{-9}$	$-3.61 \times 10^{-8}$	$4.64 \times 10^{-7}$

### 3.4 Summary

An inhomogeneity correction factor based on the concept of separating the primary and scatter dose is proposed. The primary inhomogeneity correction factor was formulated considering explicit secondary electron transport. The scatter inhomogeneity correction factor is proposed as a semi-empirical model based on the ratios of *TARs*. The results were compared with Monte Carlo simulation and experiments for extreme inhomogeneities such as air cavities. For primary calculation, Compton dose was derived on a purely theoretical

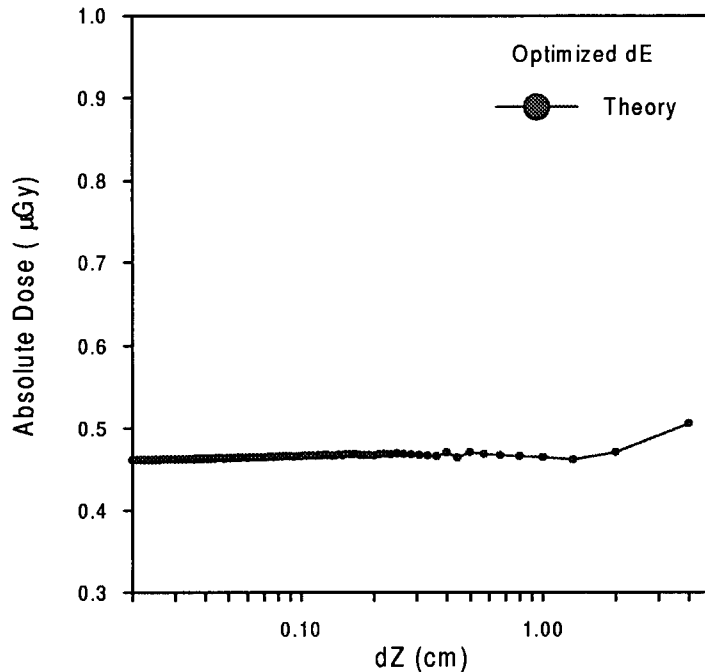


Figure 3.15: Primary Compton dose as calculated at 4 cm depth versus depth interval length for 20 MeV photons.  $dE$  was chosen following Equation 3.34.

ground. The steps taken to calculate the primary Compton dose involved determining the photon fluence distribution incident on every layer of the medium, calculating from the photon fluence the primary Compton electron distribution (based on Klein-Nishina formalism) exiting a given layer, transporting the electrons to the downstream layers to obtain the electron planar fluence distribution, converting it to dose, and summing the dose contributions by all the electrons to obtain the primary Compton dose. For scatter calculation, a ratio of tissue-air ratios employing scaled beam radius is proposed. Good agreement between the calculated and the Monte Carlo simulated absolute primary Compton dose was seen for monoenergetic photons (6 and 20

*MeV*) and polyenergetic photon beams (6 and 18 *MV*). *ICF* comparison between the three modalities gave results within 4% in regions beyond the air cavity. Parameters of integration were optimized such that a reduction in the computation time to a practical limit was observed while accuracy of calculation was maintained.

## **Chapter 4**

# **Comparison of GEANT3 and EGS4 Monte Carlo codes for photon and electron beams**

### **4.1 Introduction**

Monte Carlo calculations provide a benchmark for analytical calculations and a verification for experimental measurements [10]. The use of Monte Carlo codes in radiotherapy has become common [28, 42, 43, 64, 87, 101]. Comparisons between different Monte Carlo codes, for example EGS4 (Electron Gamma Shower version 4) [76] and MCNP4B (Monte Carlo N-Particle version 4B) [22], were recently reported for photons and electrons [63] and the codes were compared to experimental measurements for clinical electron beams [46].

Several differences were observed when the central axis depth dose curves calculated with EGS4 and MCNP4B were compared [46]. These stem from the use of different electron transport methods in accounting for the large energy loss events that occur due to the production of delta rays and

bremsstrahlung. EGS4 was found to agree better with the experimental values [46]. MCNP4B was seen to better account for electron backscattering for low and high Z materials but required longer computation times [46, 63].

Monte Carlo simulations can consume large amounts of computing time. Therefore, the efficiency of the calculations done by a particular code is of importance in a clinical setting. Simulation variables (for example, electron cutoff energy and maximum fractional energy loss) can influence the amount of time taken for any calculation [45].

The present study was initiated to investigate the GEANT3 (GEometry ANd Tracking version 3.21) Monte Carlo code developed at CERN (Centre European de la Recherche Nucleaire), Geneva, Switzerland [23] for calculations in radiotherapy physics. GEANT3 is able to simulate the dominant processes which occur in the energy range from 10 keV to 10 TeV for electromagnetic interactions. The use of GEANT3 has been mostly limited to high energy physics, though it has been used for dose calculation for radiochromic films [96], radiation protection problems [25, 62], and more recently for nuclear interactions of 160 MeV protons stopping in copper [39].

#### 4.1.1 Description of electron transport methods

GEANT3 is equipped with different user selectable electron transport modes. Being more versatile than most Monte Carlo codes concerning the production of  $\delta$ -rays, GEANT3 has three options for dealing with these rays. An important user controlled variable for these options is DCUTE below which the

delta ray energy losses are simulated as continuous energy loss by the incident electron, and above it they are explicitly generated. In the first option,  $\delta$ -ray are produced over the entire energy range: DCUTE to  $\frac{1}{2}E_{initial}$  for electron-electron scattering and DCUTE to  $E_{initial}$  for positron-electron scattering. This mode is termed as "no fluctuations". The second mode of energy loss is "full fluctuations", in which  $\delta$ -rays are not generated, and the energy loss straggling is sampled from a Landau [61], Vavilov [90, 98] or Gaussian [92] distribution each according to its validity limits [23]. The third is "restricted fluctuations", with generation of  $\delta$ -rays above DCUTE and restricted Landau fluctuations below DCUTE. In principle, choosing energy loss fluctuations carries an advantage if energy deposited is scored in voxel sizes larger than the range of  $\delta$ -rays. This results in great savings of computation time and avoids tracking a large number of  $\delta$ -rays generated below DCUTE. In all cases a continuous energy loss by the incident electron is assumed according to the Berger-Seltzer formulae [11, 17, 91].

When traversing matter, charged particles undergo deflection from their original trajectory because of their interactions with atoms. This deflection is rather large for (i) electrons that are deflected by the electric field of nuclei and (ii) electrons that undergo multiple small elastic collisions. Over the years, considerable effort has gone into the formulation of a theory of Coulomb multiple scattering. Multiple scattering is well described by Moliere theory [12, 73, 74].

Moliere multiple scattering theory is used by default in GEANT3. An important limiting factor in the Moliere theory is the average number of Coulomb scatters for a charged particle in a step,  $\Omega_0$ . When  $\Omega_0 \geq 20$ , the

Moliere theory is not applicable. The range  $1 < \Omega_0 \leq 20$  is called the plural scattering regime [55]. In this range a direct simulation method is used for the scattering angle in GEANT3 [23]. A simplification of the Moliere theory by a Gaussian form is also implemented in GEANT3. The Gaussian multiple scattering represents Moliere scattering to better than 2% for  $10 < \Omega_0 \leq 10^8$ .

On the other hand, EGS4 uses one mode of electron transport which includes generation of  $\delta$ -rays without fluctuations, which corresponds to the GEANT3 first mode of electron transport described above. Both codes use the same differential cross section for  $\delta$ -ray production for the electron-electron (Moller) scattering [75, 76] and for the positron-electron (Bhabha) scattering [13] above DCUTE in GEANT3 or AE in EGS4. For multiple Coulomb scattering both codes use the same Moliere theory, however, EGS4 does not take plural scattering into account.

#### 4.1.2 Parameters for particle tracking in a medium

Simulation results depend critically on the choice of parameters that control the transport and tracking of particles. In GEANT3, electron step sizes are limited by the smaller of the upper limits for the step imposed by the continuous energy loss and multiple Coulomb scattering. Continuous energy loss can introduce an upper limit on the step via the variable DEEMAX [23]. This parameter (maximum allowable fractional energy loss in an electron step) is also present in EGS4 (ESTEPE) which allows a fair comparison between the two codes.

A lower limitation on the tracking step is not generally imposed in

GEANT3. There is, however, a protection against the step being reduced to a very small value by continuous processes, especially multiple scattering. A variable (STMIN) is introduced which is compared with the stopping range of particles. If this range becomes smaller than STMIN, the constraint imposed by the multiple scattering is ignored and the minimum is taken between the reduced stopping range (the distance the particle has to travel to reach its threshold energy) and STMIN itself. In this sense, STMIN is no more than a "tracking accelerator" for stopping particles. Another limitation on the step size in GEANT3 is the STEMAX user controlled parameter which sets an absolute upper limit to the size of a step for each tracking medium [23].

The purpose of this study is to explore the potential of GEANT3 in modeling radiation absorbed dose for a variety of problems in medical physics. The two main issues considered are photon and electron showers interacting in a water-like material. The validity of using the different electron transport modes is to be assessed and a comprehensive timing benchmark is to be presented.

## 4.2 Materials and methods

Depth doses were calculated with both the EGS4 and GEANT3 Monte Carlo codes for monoenergetic and polyenergetic photons and monoenergetic electrons. The usercode DOSXYZ [65] was used in the EGS4 simulations with default values for the Parameter Reduced Electron Step Algorithm (PRESTA) [15]. For GEANT3, a usercode (DOSE) written in FORTRAN (Appendix C) which scores absorbed dose in cartesian coordinates was used. Monoenergetic

*6 MeV* and *20 MeV* photons incident on a water phantom were simulated. Radiation field size was set to  $5 \times 5 \text{ cm}^2$ . The water phantom formed a three dimensional dose scoring grid with  $0.5 \times 0.5 \times 0.2 \text{ cm}^2$  voxel size. For polyenergetic photons, the bremsstrahlung spectra that takes into account the structural components of the linac were for *6 MV* [71] and *18 MV* [99] Varian linacs and were derived from literature. Monoenergetic electron beams with energies *5 MeV*, *10 MeV*, *17 MeV* and *20 MeV* incident on a water phantom were also simulated in this study.

Experimental measurements are based on commissioning data using *6 MV* and *18 MV* x-rays produced by a CL 21EX linear accelerator (Varian Associates, Palo Alto, CA). Depth doses were measured in a water phantom. A radiation field size of  $5 \times 5 \text{ cm}^2$  at a source to surface distance (SSD) of  $100 \text{ cm}$  was used. The dose buildup region was measured with a parallel plate air ionization chamber (Markus PTW model 30-329, Victoreen Nuclear Associates, Carle Place, NY) as described in Chapter 2. Beyond  $d_{max}$  a cylindrical chamber (Ion chamber IC 10, Wellhofer Dosimetrie, Schwarzenbruck, Germany) was employed. This chamber has an active volume diameter of  $6 \text{ mm}$  and an active cylinder length of  $3.8 \text{ mm}$ . The central electrode has  $1 \text{ mm}$  diameter and a  $3.3 \text{ mm}$  active length. Measurements were normalized to the dose at  $10 \text{ cm}$  depth in a water phantom for both negative and positive potentials.

The usercode XYZDOS [16] supplied with the EGS4 distribution and recommended for timing studies was adopted for a timing study using a value of 0.01 for the parameters ESTEPE and DEEMAX. The electron cutoff energy in both codes (ECUT and CUTELE) was set to  $10 \text{ keV}$ . The timing study was performed on a water cube of  $20 \times 20 \times 20 \text{ cm}^3$  volume with a broad parallel

source of electrons in the range  $5 \text{ MeV}$  to  $20 \text{ MeV}$ . Furthermore, the different electron transport modes of GEANT3 were considered in this study, and in the case of "restricted fluctuations" values of  $500 \text{ keV}$ ,  $1 \text{ MeV}$ , and  $2 \text{ MeV}$  were set for DCUTE for all electron beams studied. The hardware was a 333 MHz PII PC running the *Linux* operating system.

## 4.3 Results and discussion

### 4.3.1 Photons

Comparisons of EGS4 and GEANT3 calculations of depth doses in water phantoms for the case of monoenergetic and polyenergetic photon beams are shown in Figures 4.1 and 4.2. Figures 4.1(a) and 4.1(b) show the comparison of EGS4 and GEANT3 calculations of depth doses for  $6 \text{ MeV}$  and  $20 \text{ MeV}$  monoenergetic photons respectively. Depth dose curves in Figure 4.1 are given per incident photon fluence. Results of the simulation with  $6 \text{ MV}$  and  $18 \text{ MV}$  photon spectra are given in Figures 4.2(a) and 4.2(b) respectively along with experimental results. In Figure 4.2 depth doses are normalized to the corresponding value of dose at  $10 \text{ cm}$  depth in the water phantom. This choice of depth normalization insures a minimal contribution to the scored dose at that depth due to contaminant electrons generated in the linac head.

Excellent agreement was obtained in all comparisons between EGS4 and GEANT3 (Figures 4.1 and 4.2). Also good agreement between simulation and measurements for  $6 \text{ MV}$  photon spectra was seen (Figure 4.2(a)). However,

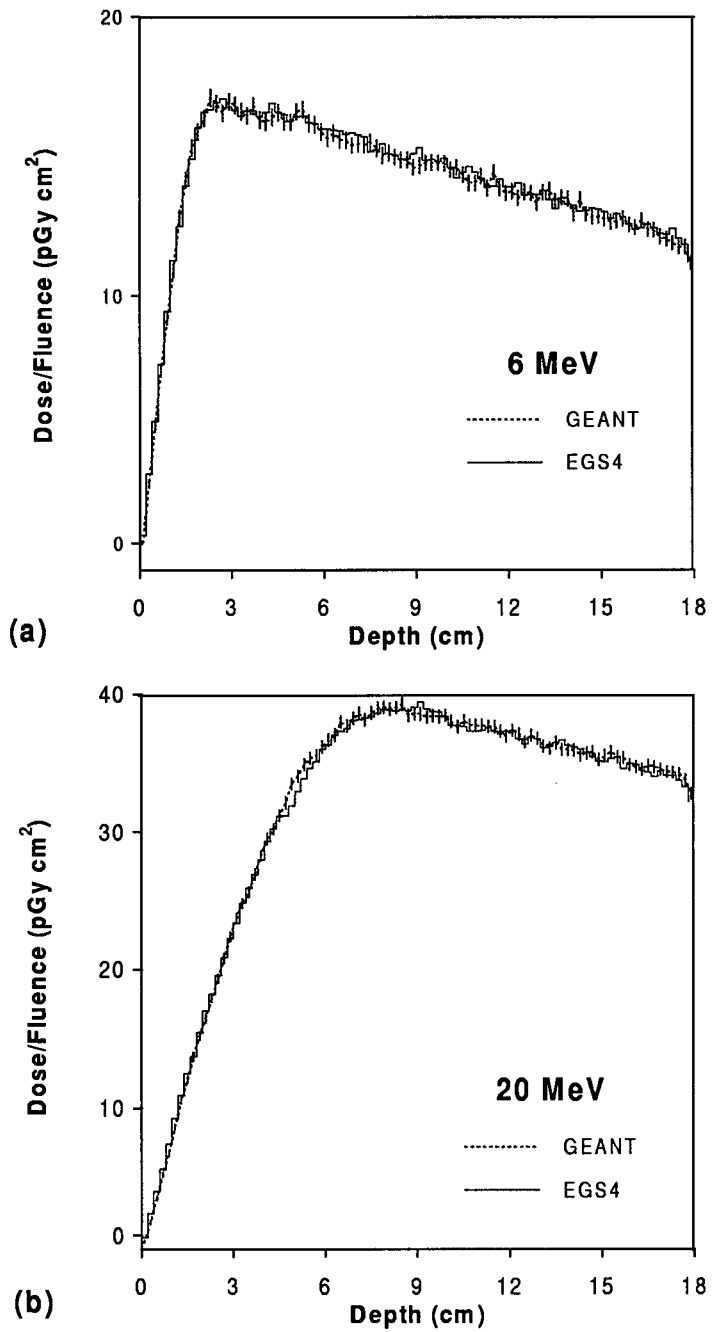


Figure 4.1: Comparison of EGS4 and GEANT3 Monte Carlo codes for depth dose calculations in water phantoms irradiated with monoenergetic  $6 \text{ MeV}$  and  $20 \text{ MeV}$  photons is shown in (a) and (b) respectively. Broad parallel beams were used.

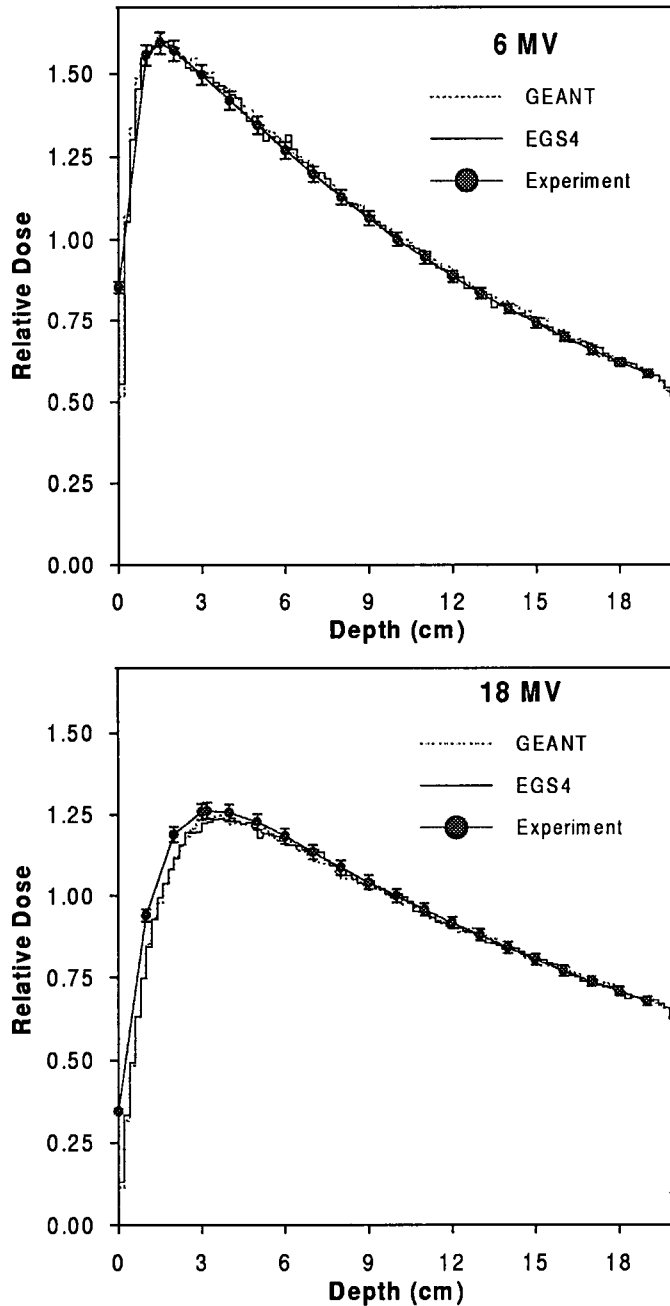


Figure 4.2: Comparison of EGS4, GEANT3 Monte Carlo codes, and experiment for depth doses in water phantoms irradiated with 6 MV and 18 MV photon beams is shown in (a) and (b) respectively. A point source was used and SSD was set to 100 cm.

a discrepancy of the order of 10% between the two Monte Carlo codes and experiment was observed at 1 *cm* depth in the water phantom as can be seen from Figure 4.2(b). This is in the buildup region of the 18 *MV* spectrum of photons where electron contamination from the linac head contributes to the absorbed dose more significantly than with the 6 *MV* spectrum. This problem of electron contamination is accounted for in the code BEAM [87] which is able to generate a phase space file of contaminant electrons that can be transported in the water phantom. The radiation transport in the current simulations using both EGS4 and GEANT3 was started at the water phantom entrance and it is assumed the discrepancy is due to this difference. The electron transport option used in GEANT3 for these simulations is the "no fluctuations" option.

The GEANT3 code used in this study was the 96a version of the CERN Library. Later versions of the CERN Library were also used, however, all of them showed artifacts in depth doses at the phantom entrance. All the simulations were based on 100 million events taking between 50 to 100 hours of computation time.

### 4.3.2 Electrons

A comparison of depth doses (normalized to incident electron fluence) calculated by EGS4 and GEANT3 for monoenergetic electrons of 5 *MeV*, 10 *MeV*, 17 *MeV*, and 20 *MeV* are shown in Figure 4.3. The electron transport option used in GEANT3 for these simulations was "no fluctuations".

Good agreement was also seen in all of these cases. However, EGS4

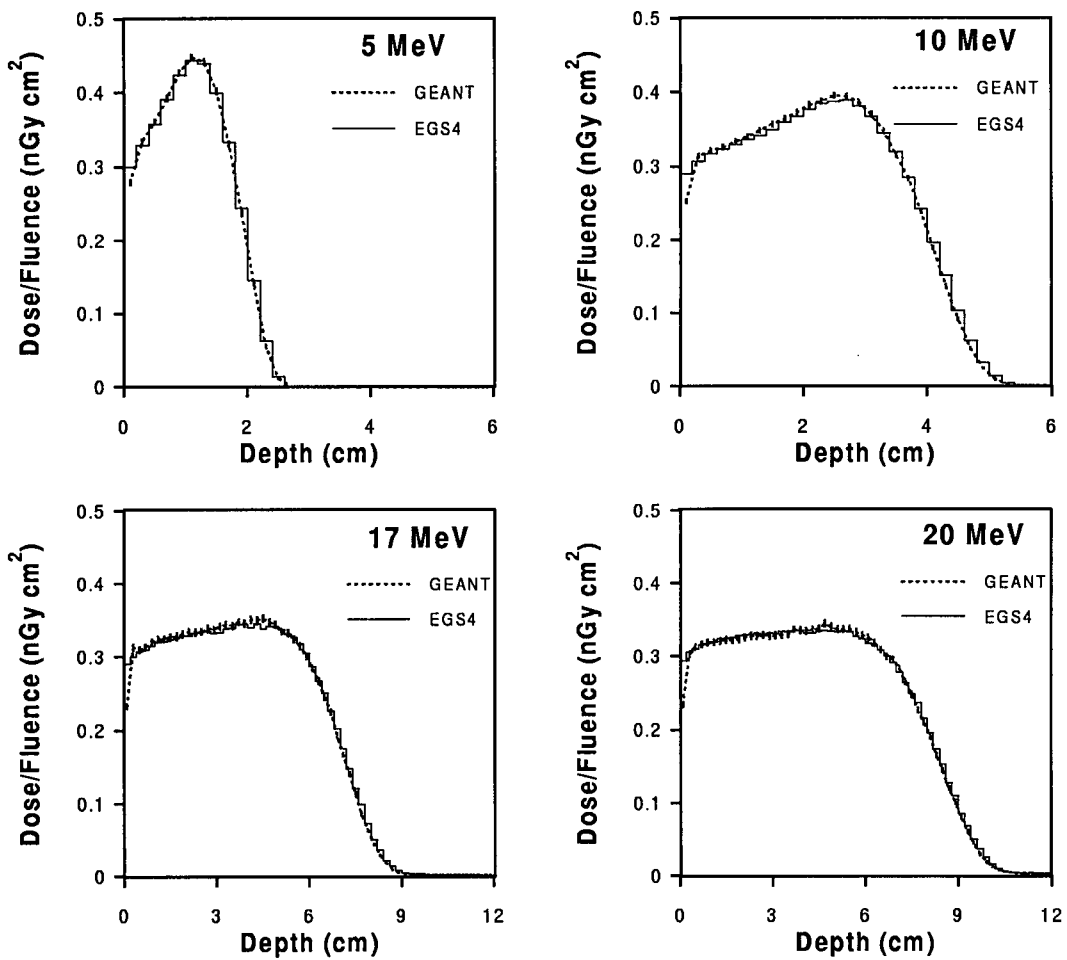


Figure 4.3: The comparison of EGS4, GEANT3 Monte Carlo codes for depth dose calculations in water phantoms irradiated with a range of monoenergetic electrons is shown. The electron transport option used in GEANT3 was the "no fluctuations". Dose was normalized to incident electron fluence.

comes with the very important step size algorithm (PRESTA) which makes it more accurate at the beam entrance where very short electron steps are needed. A clear underestimation of the GEANT3 calculations was seen in the first voxel due to this effect.

To assess the validity of using the other electron transport modes in GEANT3 a comparison was carried out using all three modes with a range of values for DCUTE in the case of "restricted fluctuations". Results using 5 MeV and 20 MeV electrons are shown in Figure 4.4(a) and 4.4(b) respectively. The values chosen for DCUTE were 1 MeV and 2 MeV for the 5 MeV and 20 MeV electron energies respectively. This choice covers the energy range for the majority of  $\delta$ -rays produced.

As can be seen from Figure 4.4, using energy loss fluctuations results in underestimating the value of dose in the buildup region and overestimating it past the buildup region. The maximum discrepancy was within 2% for the 5 MeV electron beam. This effect was seen with other Monte Carlo codes which account for energy loss straggling based on the Landau theory [61, 63, 86]. The "restricted fluctuations" option for the 5 MeV electrons gave depth dose curves in between the "no fluctuations" and the "full fluctuations" curves. For small values of DCUTE (100 keV) the depth dose curve matched the "no fluctuations" option and for large values of DCUTE (2 MeV) the depth dose curve matched the "full fluctuations" results as it is expected (data not shown).

For the 20 MeV beam statistical fluctuations in the absorbed dose in the buildup region are observed for the two fluctuation modes available in GEANT3 (Figure 4.4(b)). This shows the inaccuracy of using fluctuation

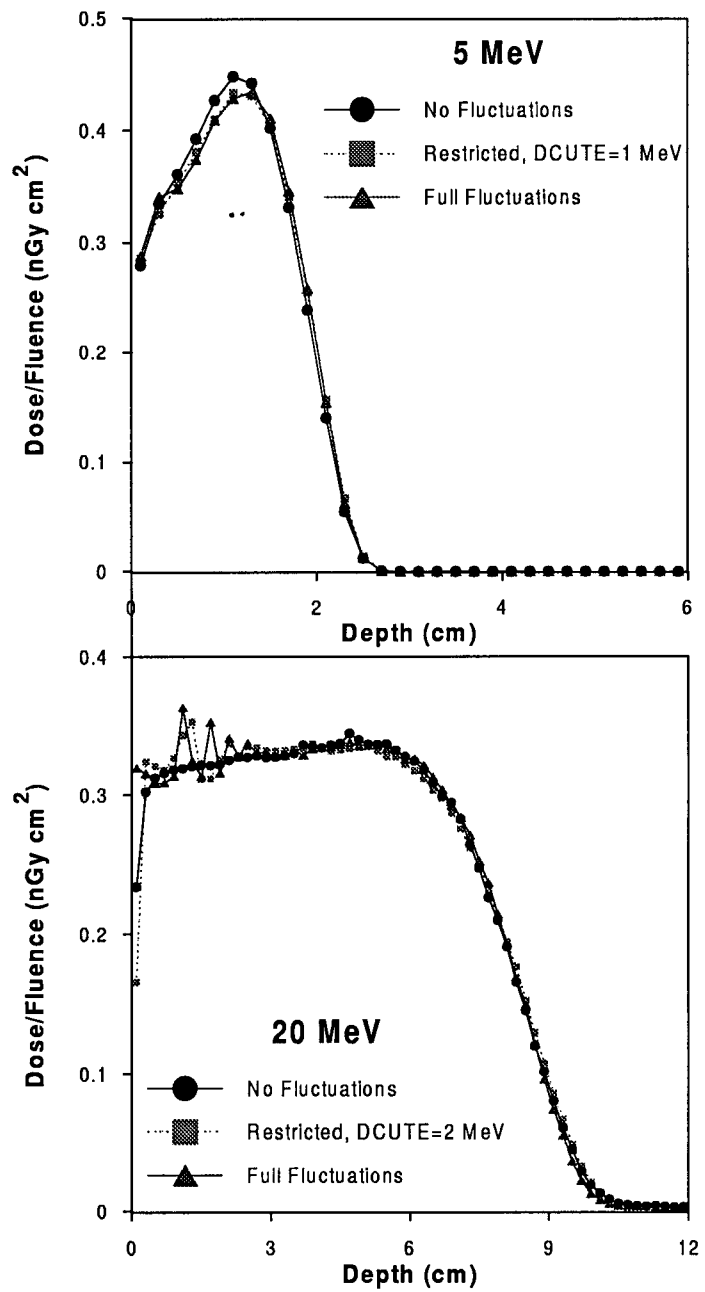


Figure 4.4: The comparison of the three electron transport modes implemented in the GEANT3 Monte Carlo code for depth dose calculations in water phantoms is shown. Depth doses for 5 MeV and 20 MeV monoenergetic electrons are shown in (a) and (b) respectively. Dose was normalized to incident electron fluence.

modes for electron energies greater than 10  $MeV$  under small scoring voxel ( $0.5 \times 0.5 \times 0.2 \text{ cm}^3$ ) conditions. This is attributed mainly to the absence of  $\delta$ -ray production below DCUTE and the deposition of energy local to the current voxel. A large number of delta rays produced by incident electrons in the energy range considered are below 1  $MeV$ . This corresponds to a maximum electron range of 0.53  $cm$  in water (derived using DOSXYZ simulation). Increasing the scoring voxel size (for example, increasing the dimension along the beam direction to 0.5  $cm$ ) leads to an improvement of the 20  $MeV$  electron beam results (data not shown).

The main advantage of using "restricted fluctuations" is one can control the accuracy of the simulation via the parameter DCUTE. A small value of DCUTE (< 500keV for 5  $MeV$  electrons) improves the agreement between the "restricted fluctuations" and the "no fluctuations" simulations. A large value for DCUTE (2.5  $MeV$  for 5  $MeV$  electrons) gives an exact match between the "restricted fluctuations" and the "full fluctuations" simulations. However, decreasing DCUTE comes at the expense of increasing computation time as we shall see in the next section.

### 4.3.3 Calculation time comparison

A comparison of the time of calculation of the GEANT3 and EGS4 codes for electron beams is shown in Table 4.1. The numbers shown are the amount of time in milli-seconds (ms) for one history event of an incident electron when transported until its kinetic energy falls below a predefined cutoff value (ECUT or CUTELE). This comparison was carried out for four different elec-

tron beams.

The EGS4 time values appear to be half of the "No fluctuations" GEANT3 values consistently for all energies investigated. However, this trend is reversed when "restricted fluctuations" is chosen, and an improvement in GEANT3 calculation speed is noticed. Under this mode the parameter DCUTE was set to 500 *keV*, 1 *MeV*, and 2 *MeV* for all four electron energies. As DCUTE approaches the maximum energy range of  $\delta$ -rays, the computation time decreases and tends to the values of the "full fluctuations" mode. This can be seen from the last two columns of Table 4.1. The time values under the "full fluctuations" mode in GEANT3 are consistently lower than those of EGS4. For instance, in case of 20 *MeV* electrons, GEANT3 is three times faster than EGS4. Therefore, the fastest mode under which GEANT3 can operate is the "full fluctuations" mode.

The tracking medium parameter (STMIN, discussed in section 4.2) was set to zero in the timing study. An attempt to increase this parameter to 0.007 *cm* for water as recommended [23] yielded an increase in speed by a factor of 10 for all energies considered (Table 4.2). This parameter is implemented in the GEANT3 code itself not in the usercode DOSE and it is regarded as a variance reduction tool. Furthermore, increasing STMIN to 0.007 *cm* gave an accuracy to better than 2% when compared with STMIN zero setting. This shows the crucial role of this parameter when calculation time is of practical importance.

Table 4.1: Calculation time comparison between EGS4 and GEANT3 per event history. ESTEPE and DEEMAX were set to 0.01, ECUT and CUTELE were set to 10  $keV$ , and AE was set to 521  $keV$  while DCUTE is given below.

Energy (MeV)	EGS4		GEANT			
	XYZDOS (ms)	NO Fluctuations (ms)	Restricted Fluctuations (ms)			Full Fluctuations (ms)
		AE= 10 keV	DCUTE= 10 keV	DCUTE= 0.5 MeV	DCUTE= 1.0 MeV	DCUTE= 2.0 MeV
5	28.0	53.8	26.5	23.8	23.0	23.1
10	51.6	97.7	38.7	33.1	30.1	28.9
17	83.7	157.2	53.7	44.3	38.9	33.6
20	95.6	175.0	59.9	45.8	40.8	35.3

## 4.4 Summary

The Monte Carlo codes EGS4 and GEANT3 have been compared for calculations of photon and electron depth doses in water. For photons, monoenergetic (6  $MeV$  and 20  $MeV$ ) and polyenergetic (6  $MV$  and 18  $MV$ ) beams were considered and experimental results from a CL 21EX Varian linac were used for comparisons. In all cases excellent agreement was found between the two codes. For electron beams, energies ranging from 5  $MeV$  to 20  $MeV$  were chosen and again good agreement was found except for the interface dose where GEANT3 underestimates the dose, especially for the higher energies compared to EGS4. The discrepancy in the interface dose is attributed to the role of PRESTA in EGS4 in choosing appropriate electron step size at

Table 4.2: Calculation time comparison between EGS4 and GEANT3 per electron event history. STMIN is set as recommended in GEANT3 manual.

Energy (MeV)	EGS4	GEANT3
	XYZDOS (ms)	NO Fluctuations (ms)
	AE=10 keV	DCUTE=10 keV
5	28.0	4.3
10	51.6	6.6
17	83.7	9.3
20	95.6	10.4

interfaces in small scoring voxels. The three electron transport modes implemented in GEANT3 were used for the above electron beams and their accuracy correlated with increasing computation time. To conclude the comparison, a timing study was performed. GEANT3 was seen to be two times slower than EGS4 in one of its electron transport modes and up to three times faster when adapting its energy straggling mode which accounts for the energy loss using the Landau/Vavilov/Gaussian models each being used according to its validity limits.

## **Chapter 5**

### **Conclusions and future directions**

In this thesis, we have investigated a series of topics dealing with radiation dose calculations in heterogeneous tissues. This last chapter summarizes and presents conclusions of this work. The first topic was an investigation of the limitations of several current treatment planning algorithms for dose calculations in heterogeneous phantoms with air cavities. The second topic is a description of an analytical approach to the calculation of primary Compton dose distribution in both homogeneous and heterogeneous phantoms, and the derivation of an inhomogeneity correction factor. Finally, in the pursuit of treatment planning based on Monte Carlo simulation we explored the potential of GEANT3 for dose calculation in clinically relevant cases.

## 5.1 Summary of work

The perturbation of dose distributions by air cavities was investigated as a function of photon energy, field size, size and shape of the cavity and depth of the point of measurement for varying geometries. Data presented in this report show alteration in the dose at air/polystyrene interfaces for different air gap thickness as determined by commercial treatment planning systems using the Batho, modified Batho and ETAR methods compared to experiments. The latter demonstrated a significant underdosing down to a relative dose at the interface of 0.45 for a 5 cm air gap for 6 MV and 5x5 cm<sup>2</sup> field size while the treatment planning systems over-predicted the relative dose (0.9). These differences are due to the fact that electronic disequilibrium is not accounted for by the algorithms used in the treatment planning systems.

Geometries of air gap widths ranging from 2x2 cm<sup>2</sup> to 20x20 cm<sup>2</sup> demonstrated the effect of the scatter component of the dose from the walls and its magnitude at interfaces. The underdosing observed may be significant at depths of several centimeters from the interface for smaller field sizes and air gaps approaching the field size in their lateral dimensions. These findings point to the need for proper inclusion of electron disequilibrium effects at interfaces as would be possible with Monte Carlo simulation and superposition/convolution algorithms [68]. This is an area of active investigation [82, 103].

The concept of separating the primary and scatter components of dose was applied to the derivation of an inhomogeneity correction factor (*ICF*). *ICF* was calculated as a weighted sum of primary and scatter components.

$ICF_p$  distribution in the presence of air cavities was calculated employing detailed electron transport. Primary Compton dose was calculated using the Fermi-Eyges multiple scattering theory as in the framework of the "photon-electron cascade" model [110]. The steps that were taken involve determining the primary photon fluence distribution incident to every layer of the medium, calculating from the photon fluence the Compton electron distribution exiting the given layer, transporting the electrons to the downstream layers to obtain electron planar fluence distribution and converting it to dose, and summing the dose contributions over all electron energy intervals to obtain the primary Compton dose. A comprehensive study of the different assumptions made, i.e. neglecting delta-ray ( $\delta$ -ray) production and forward directed secondary electrons was presented. The calculated primary Compton dose agreed with Monte Carlo simulation over the range of energies investigated for monoenergetic photons (1-20 MeV) and polyenergetic (6-18 MV) photon beams considering the statistical fluctuations of the simulation results.

Since electron transport in scatter dose calculation is not as crucial as in the primary case, a semi-empirical method for  $ICF_s$  calculation is proposed. A relationship to the *ETAR* correction method was established and depth dose curves in inhomogeneous phantom with air cavities were derived. The total  $ICF$  was calculated and found to be in agreement to within 4% with Monte Carlo simulations and experiments in the second buildup region seen beyond the distal water/air interface. Our primary correction model as it stands would be an ideal method for inhomogeneity correction in radiosurgery where photon irradiations with field size smaller than  $5 \times 5 \text{ cm}^2$  are employed and more electronic disequilibrium effects are seen. However, for the larger field sizes the scatter correction method ( $ICF_s$ ) needs to be incorporated as

discussed.

A method for minimizing computation time was devised. For obtaining an *ICF* distribution, it was found that the choice of parameters of integration does affect the absolute dose distribution but not the *ICF* distribution. The latter parameters were investigated and timings of calculation were within a few minutes even for the high energy limit (20 *MeV* photons). Furthermore, a numerical technique was devised for the accurate and fast calculation of primary Compton dose. An optimization formula, which relates the different integration differential variables, was derived and the dose function can now be accurately evaluated with a minimal number of intervals for the variables.

Proper modeling of photon and electron transport in photon and electron beams in the low megavoltage energy range can be done using GEANT3. Comparisons to EGS4 calculated photon and electron depth dose curves in clinically relevant cases gave results within 2%. The three electron transport modes in GEANT3 give it diversity and more options in which accuracy can be traded with speed. Extra care should be taken while calculating electron depth dose curves when using fluctuation modes in GEANT3. In these modes delta rays are not produced below a parameter DCUTE and energy loss straggling is employed instead based on the Landau/Vavilov/Gaussian models. Under this option it is recommended to use large voxel size for dose scoring (around 0.5x0.5x0.5 *cm*<sup>3</sup>) that can accommodate the range of the large number of delta rays produced under 1 *MeV*. Timing comparisons between GEANT3 and EGS4 show that significant saving in computation time can be achieved under the "full fluctuations" mode in GEANT3 version 96a.

## 5.2 Future directions

Much work is presented in this thesis on several topics of dose calculation in inhomogeneous phantoms. Nevertheless, there are still many avenues of investigation which could be followed to continue this work and improve accuracy of calculations. In the process of calculating primary Compton dose distribution numerical integration techniques used to evaluate integrals were fairly basic ones, improvements in accuracy and computation time should be possible when using more specialized techniques like the Gaussian quadrature method. In the same light, optimization of the code (Appendix B) would also increase the speed of this implementation.

There is also more work that could be done validating the clinical usefulness of our method with regards to other inhomogeneity correction for instance lungs. The present approach was used for semi-infinite slab geometry. This approach is applicable to dose calculations for cases with three dimensional inhomogeneities. It is worthwhile to point out that a number of cases were investigated but were too few to be included in this thesis.

On the calculation of a total inhomogeneity correction factor other ways can be considered such as detailed electron transport at areas of interest and semi-empirical calculations (using Batho or ETAR corrections) elsewhere. In inhomogeneous phantoms it is sufficient to do the calculation only at the inhomogeneity site and at the second buildup region beyond the distal interface of water/air. Hence electrons generated inside the inhomogeneity area and around it within a margin of  $d_{max}$  (maximum distance for electron travel at the given energy) need only to be transported which can further reduce the

computation time. This approach was adopted with the Monte Carlo and the convolution/superposition methods [108] and found promising in clinically relevant cases.

## Bibliography

- [1] A. Ahnesjo. Collapsed cone convolution of radiant energy for photon dose calculation in heterogeneous media. *Med. Phys.*, 16:577 – 592, 1989.
- [2] A. Ahnesjo and M. M. Aspradakis. Dose calculations for external photon beams in radiotherapy. *Phys. Med. Biol.*, 44:R99–R155, 1999.
- [3] P. Andreo and A. Brahme. Restricted energy loss straggling and multiple scattering of electrons in mixed Monte Carlo procedures. *Radiat. Res.*, 100:16 – 29, 1984.
- [4] F. H. Attix. *Introduction to radiological physics and radiation dosimetry*. New York: Wiley, 1986.
- [5] F. H. Attix and W. C. Roesch. *Radiation Dosimetry*. Academic Press, New York and London, second edition, 1968.
- [6] H. F. Batho. Lung corrections in cobalt 60 beam therapy. *J. Can. Assn. Radiol.*, 15:39 – 83, 1964.
- [7] J. J. Battista, T. R. Mackie, E. El-Khatib, and J. W. Scrimger. Lung dose corrections for 6 MV and 15 MV X-rays: anomalies. In *Proceedings of the 8th International Conference on the Use of Computers in Radiation Therapy*, 1984.

- [8] J. L. Beach, M. S. Mendiondo, and O. A. Mendiondo. A comparison of air-cavity inhomogeneity effects for cobalt-60, 6 and 10 MV x-ray beams. *Med. Phys.*, 14:140 – 144, 1987.
- [9] R. Bellman and G. M. Wing. *An introduction to Invariant Embedding*. New York: Wiley, 1975.
- [10] M. J. Berger. Monte Carlo calculation of the penetration and diffusion of fast charged particles. *Methods Comput. Phys.*, 1, 1963.
- [11] H. A. Bethe. *Ann. Phys.*, 5:325, 1930.
- [12] H. A. Bethe. *Phys. Rev.*, 89:1256, 1953.
- [13] H. J. Bhabha. The scattering of positrons by electrons with exchange on Dirac's theory of the positron. *Proc. Roy. Soc. (London)*, A154:195, 1936.
- [14] A. F. Bielajew, A. E. Nahum, W. R. Nelson, and D. W. O. Rogers. "A course on Radiation Transport Calculations using EGS4". *National Research Council of Canada, Ottawa*.
- [15] A. F. Bielajew and D. W. O. Rogers. PRESTA: the parameter reduced electron-step transport algorithm for electron Monte Carlo transport. *Nucl. Instr. Methods*, B 18:165 – 181, 1987.
- [16] A. F. Bielajew and D. W. O. Rogers. A standard timing benchmark for EGS4 Monte Carlo calculations. *Med. Phys.*, 19:303 – 313, 1992.
- [17] F. Bloch. *Z. fur Phys.*, 81:363, 1933.
- [18] C. Bogers. Complexity of Monte Carlo and deterministic dose-calculation methods. *Phys. Med. Biol.*, 43:517 – 528, 1998.

- [19] A. L. Boyer and E. C. Mok. A photon dose distribution model employing convolution calculations. *Med. Phys.*, 12:169 – 177, 1985.
- [20] A. L. Boyer and E. C. Mok. Calculation of photon dose distributions in an inhomogeneous medium using convolutions. *Med. Phys.*, 13:503 – 509, 1986.
- [21] A. Brahme, J. Chavaudra, T. Landberg, E. C. McCullough, F. Nusslin, J. A. Rawlinson, G. Svensson, and H. Svensson. Accuracy requirements and quality assurance of external beam therapy with photons and electrons. *Acta Oncol., Suppl. 1*, pages 1 – 76, 1988.
- [22] J. F. Briesmeister. *MCNP–A general Monte Carlo N-particle transport code, Version 4A*. Los Alamos National Laboratory Report, LA-12625, 1993.
- [23] R. Brun, F. B. Ruyant, M. Maire, A. C. McPherson, and P. Zanarnit. *GEANT3-Detector description and simulation tool (Reference Manual)*. March 1994.
- [24] K. J. Cassell, P. A. Hobday, and R. P. Parker. The implementation of a generalised Batho inhomogeneity correction for radiotherapy planning with direct use of CT numbers. *Phys. Med. Biol.*, 26:835 – 833, 1981.
- [25] A. Clouvas, S. Xanthos, M. Antonopoulos-Domis, and J. Silva. Monte Carlo based method for conversion of in-situ gamma ray spectra obtained with a portable Ge detector to an incident photon flux energy distribution. *Health Phys.*, 2:208 – 210, 1998.

- [26] J. R. Cunningham. *Current and future development of tissue inhomogeneity corrections for photon beam clinical dosimetry with the use of CT*. Raven Press, 1983.
- [27] J. Cygler, J. J. Battista, J. W. Scrimger, E. Mah, and J. Antolak. Electron dose distributions in experimental phantoms: A comparison with 2D pencil beam calculations. *Phys. Med. Biol.*, 32:1073, 1987.
- [28] J. J. DeMarco, T. D. Solberg, and J. B. Smathers. A CT-based Monte Carlo simulation tool for dosimetry planning and analysis. *Med. Phys.*, 25:1 – 11, 1997.
- [29] M. Dollinger, E. H. Rosenbaum, and G. Cable. *Everyone's guide to Cancer Therapy*. Somerville House publishing, Toronto, second edition, 1995.
- [30] J. Van Dyk, R. B. Barnett, J. E. Cygler, and P. C. Shragge. Commissioning and quality assurance of treatment planning computers. *Int. J. Radiat. Oncol. Biol. Phys.*, 26:261 – 273, 1993.
- [31] E. El-Khatib. The present status of lung dosimetry in radiation treatment planning. *AAMD J.*, 10:9 – 15, 1985.
- [32] E. El-Khatib and J. J. Battista. Improved lung dose calculation using tissue-maximum ratios in the Batho correction. *Med. Phys.*, 11:279 – 286, 1984.
- [33] E. R. Epp, A. L. Boyer, and K. P. Doppke. Underdosing of lesions resulting from lack of electronic equilibrium in upper respiratory air cavities irradiated by 10 MV x-ray beams. *Int. J. Radiat. Oncol. Biol. Phys.*, 2:613 – 619, 1977.

- [34] R. D. Evans. *The Atomic Nucleus*. New York: McGraw-Hill, 1952.
- [35] L. Egyes. Multiple scattering with energy loss. *Phys. Rev.*, 74:1534, 1948.
- [36] U. Fano. Note on the Bragg-Gray cavity principle for measuring energy dissipation. *Radiat. Res.*, 1:237 – 240, 1954.
- [37] A. Ferlito. *Cancer of the Larynx*. CRC Press, Inc., 1985.
- [38] M. Fippel. Fast Monte Carlo dose calculation for photon beams based on the VMC electron algorithm. *Med. Phys.*, 26:1466 – 1475, 1999.
- [39] B. Gottschalk, R. Platais, and H. Pagenetti. Nuclear interactions of 160 MeV protons stopping in copper: A test of Monte Carlo nuclear models. *Med. Phys.*, 26:2597 – 2601, 1999.
- [40] D. Harder. *Spectra of primary and secondary electrons in material irradiated by fast electrons*. Biophysical Aspects of Radiation Quality, IAEA Technical Report Ser. No.58 (International Atomic Energy Agency, Vienna), 1966.
- [41] D. Harder. On electron dosimetry. In A. Zupinger and G. Poretti, editors, *Symposium on High Energy Electronics*, page 260. Springer, Berlin, 1970.
- [42] C. L. Hartmann-Siantar, W. P. Chandler, N. W. Albright, L. J. Verhey, S. M. Hornstein, L. J. Cox, J. A. Rathkopf, and M. M. Svatos. Validation and performance assessment of the PEREGRINE all-particle Monte Carlo code for photon beam therapy. *Med. Phys.*, 23:1128, 1996.
- [43] C. L. Hartmann-Siantar, W. P. Chandler, M. B. Chadwick, H. M. Blann, L. J. Cox, D. A. Resler, J. A. Rathkopf, T. R. Mackie, J. V. Siebers,

- M. A. Ross, P. M. DeLuca, K. A. Weaver, and R. M. White. Dose distributions calculated with the PEREGRINE all-particle Monte Carlo code. *Med. Phys.*, 22:994, 1995.
- [44] K. R. Hogstrom, M. D. Mills, and P. R. Almond. Electron beam dose calculations. *Phys. Med. Biol.*, 26:445 – 459, 1981.
- [45] T. M. Jenkins, W. R. Nelson, and A. Rindi (editors). *Monte Carlo transport of electrons and photons*. Plenum Press, New York, 1988.
- [46] R. Jeraj, P. J. Keall, and P. M. Ostwald. Comparisons between MCNP, EGS4 and experiment for clinical electron beams. *Phys. Med. Biol.*, 44:705 – 717, 1999.
- [47] D. Jette. The application of multiple scattering theory to therapeutic electron dosimetry. *Med. Phys.*, 10:141 – 146, 1983.
- [48] D. Jette. Electron dose calculation using multiple-scattering theory. A. Gaussian multiple-scattering theory. *Med. Phys.*, 15:123 – 137, 1988.
- [49] D. Jette. Photon dose calculation based on electron multiple-scattering theory: practical representation of dose and particle transport integrals. *Med. Phys.*, 26:924 – 930, 1999.
- [50] H. E. Johns and J. R. Cunningham. *The Physics of Radiology*. Charles C Thomas, fourth edition, 1983.
- [51] C. J. Karzmark, C. S. Numan, and E. Tanaba. *Medical Electron Accelerators*. McGraw-Hill, Inc., 1993.
- [52] K. R. Kase, B. E. Bjarngard, and F. H. Attix (editors). *The dosimetry of ionizing radiation*, volume III. New York: Academic, 1968.

- [53] I Kawrakow and A. F. Bielajew. On the condensed history technique for electron transport. *Nucl. Instr. Methods*, 13:253 – 280, 1998.
- [54] P. J. Keall and P. H. Hoban. Superposition dose calculation incorporating Monte Carlo generated electron track kernels. *Med. Phys.*, 23:479 – 485, 1996.
- [55] E. Keil, E. Zeitler, and W. Zinn. Zur Einfach- und Mehrfachstreuung geladener Teilchen. *Z. Naturforsch*, 15a:1031, 1960.
- [56] F. M. Khan. *The physics of radiation therapy*. Williams and Wilkins, second edition, 1994.
- [57] E. E. Klein, L. M. Chin, R. K. Rice, and B. J. Mijnheer. The influence of air cavities on interface doses for photon beams. *Int. J. Radiat. Oncol. Biol. Phys.*, 27:419 – 427, 1993.
- [58] T. Knoos, C. Ceberg, L. Weber, and P. Nilsson. The dosimetric verification of a pencil beam treatment planning system. *Phys. Med. Biol.*, 39:1609 – 1628, 1994.
- [59] R. O. Kornelsen and M. E. J. Young. Empirical equations for the representation of depth dose data for computerized treatment planning. *Med. Phys.*, 48:739 – 748, 1975.
- [60] W. Kwa. *Asymmetric Collimation: Dosimetric Characteristics, Treatment Planning Algorithm, and Clinical Applications*. The University of British Columbia (Ph.D. thesis), 1998.
- [61] L. Landau. On the energy loss of fast particles by ionization. *J. Phys. USSR*, 8:201 – 205, 1944.

- [62] A. Likar, T. Vidmar, and B. Pucelj. Monte Carlo determination of gamma-ray dose rate with the GEANT system. *Health. Phys.*, 2:165 – 169, 1998.
- [63] P. A. Love, D. G. Lewis, A. M. Al-Affan, and C. W. Smith. Comparison of EGS4 and MCNP Monte Carlo codes when calculating radiotherapy depth doses. *Phys. Med. Biol.*, 43:1351 – 1357, 1998.
- [64] C. M. Ma, E. Mok, A. Kapur, T. Pawlicki, D. Findley, S. Brain, K. Forster, and A. L. Boyer. Clinical implementation of a Monte Carlo treatment planning system. *Med. Phys.*, 26:2133 – 2143, 1999.
- [65] C. M. Ma, P. J. Reckwerdt, M. Holmes, D. W. O. Rogers, and B. Geiser. *DOSXYZ Users Manual*. National Research Council of Canada Report No. PIRS-509B, (NRCC, Ottawa, Canada 1995).
- [66] T. R. Mackie, E. El-Khatib, J. J. Battista, J. Scrimger, J. Van Dyk, and J. R. Cunningham. Lung dose corrections for 6 MV and 15 MV X-rays. *Med. Phys.*, 12:327 – 332, 1985.
- [67] T. R. Mackie, J. Scrimger, and J. J. Battista. A convolution method of calculating dose for 15 MV x-rays. *Med. Phys.*, 12:188 – 196, 1985.
- [68] T. R. Mackie, J. Scrimger, J. J. Battista, and E. El-Khatib. A convolution method for calculating dose in situations of lateral electronic disequilibrium. *Med. Phys.*, 11:397, 1984.
- [69] P. Metcalfe, T. Kron, and P. Hoban. *The Physics of Radiotherapy X-Rays from Linear Accelerators*. Medical Physics Publishing, Madison, Wisconsin, 1997.

- [70] R. R. Million. The larynx ... so to speak: Everything I wanted to know about laryngeal cancer I learned in the last 32 years. *Int. J. Radiat. Oncol. Biol. Phys.*, 23:691 – 704, 1992.
- [71] R. Mohan and C. Chui. Energy and angular distributions of photons from medical linear accelerators. *Med. Phys.*, 12:592 – 597, 1985.
- [72] R. Mohan and C. Chui. Differential pencil beam dose computation model for photons. *Med. Phys.*, 13:64 – 73, 1986.
- [73] G. Z. Moliere. Theorie der Streuung schneller geladener Teilchen I: Einzelstreuung am abgeschirmten Coulomb-Feld. *Z. Naturforsch.*, 2a:133, 1947.
- [74] G. Z. Moliere. Theorie der Streuung schneller geladener Teilchen II: Mehrfach- und Vielfachstreuung. *Z. Naturforsch.*, 3a:78, 1948.
- [75] C. Moller. Zur Theorie des Durchgangs schneller Electronen durch Materie. *Ann. Phys.*, 14:568, 1932.
- [76] R. Nelson, H. Hirayama, and D. W. O. Rogers. *The EGS4 Code System*. Stanford Linear Accelerator Center Report, No. SLAC-265, (SLAC, Stanford, CA, 1985).
- [77] A. Niroomand-Rad, K. W. Harter, S. Thobejane, and K. Bertrand. Air cavity effects on the radiation dose to the larynx using Co-60, 6 MV, and 10 MV photon beams. *Int. J. Radiat. Oncol. Biol. Phys.*, 29:1139 – 1146, 1994.
- [78] J. E. O'Connor. The variation of scattered x-rays with density in an irradiated body. *Phys. Med. Biol.*, 1:352 – 369, 1957.

- [79] International Commission on Radiation Units and Measurements (ICRU). *Radiation dosimetry: Electron beams with energies between 1 and 50 MeV*. Report No. 35, (ICRU Washington, DC, 1984).
- [80] P. M. Ostwald, T Kron, and C. Hamilton. Assessment of mucosal under-dosing in larynx irradiation. *Int. J. Radiat. Oncol. Biol. Phys.*, 36:181 – 187, 1996.
- [81] S. Ozard and E. El-Khatib. Portal detector scatter dose calculation: Comparison of Convolution/Superposition with Monte Carlo. *Med. Phys.*, 26:1431, 1999.
- [82] N. Papanikolaou, T. R. Mackie, C. Merger-Wells, M. Gehring, and P. Reckwerdt. Investigation of the convolution method for polyenergetic spectra. *Med. Phys.*, 20:1327 – 1336, 1993.
- [83] D. J. Perry and J. G. Holt. A model for calculating the effects of small inhomogeneities on electron beam dose distributions. *Med. Phys.*, 7:207 – 212, 1980.
- [84] W. H. Press, W. T. Vetterling, S. A. Teukolsky, and B. P. Flannery. *Numerical Recipes in C: The Art of Scientific Computing*. Cambridge University Press, second edition, 1992.
- [85] D. W. O. Rogers. Low energy electron transport with EGS. *Nucl. Instr. Meth.*, A227:535 – 548, 1984.
- [86] D. W. O. Rogers and A. F. Bielajew. Differences in electron depth-dose curves calculated with EGS and ETRAN and improved energy-range relationships. *Med. Phys.*, 13:687 – 694, 1986.

- [87] D. W. O. Rogers, B. A. Faddegon, G. X. Ding, C. M. Ma, J. We, and T. R. Mackie. BEAM: a Monte Carlo code to simulate radiotherapy treatment units. *Med. Phys.*, 22:503 – 524, 1995.
- [88] B. Rossi and K. Greisen. *Rev. Mod. Phys.*, 13:240, 1941.
- [89] H. H. Rossi and W. C. Roesch. Field equations in dosimetry. *Radiat. Res.*, 16:783 – 795, 1962.
- [90] B. Schorr. Programs for the Landau and the Vavilov distributions and the corresponding random numbers. *Comp. Phys. Comm.*, 7:216, 1974.
- [91] S. M. Seltzer and M. J. Berger. Technical Report SP 3012, NASA, 1964.
- [92] S. M. Seltzer and M. J. Berger. *Energy loss straggling of protons and mesons. In studies in Penetration of Charged Particles in Matter*. Nuclear Science Series 39, Nat. Academy of Sciences, Washington DC, 1964.
- [93] B. H. Shahine and E. El-Khatib. Experimental evaluation of interface doses in the presence of air cavities compared with treatment planning algorithms. *Med. Phys.*, 26:350 – 355, 1999.
- [94] M. R. Sontag and J. R. Cunningham. Corrections to absorbed dose calculations for tissue inhomogeneities. *Med. Phys.*, 4:431 – 436, 1977.
- [95] M. R. Sontag and J. R. Cunningham. The equivalent tissue-air ratio method for making absorbed dose calculations in a heterogeneous medium. *Radiology*, 129:787 – 794, 1978.
- [96] G. Taccini, F. Cavagnetto, G. Coscia, S. Garelli, and A. Pilot. The determination of dose characteristics of ruthenium ophthalmic applicators using radiochromic film. *Med. Phys.*, 24:2034 – 2037, 1997.

- [97] S. J. Thomas. A modified power-law formula for inhomogeneity correction in beams of high-energy x-rays. *Med. Phys.*, 18:719 – 723, 1991.
- [98] P. V. Vavilov. Ionisation losses of high energy heavy particles. *Soviet Physics JETP*, 5:749, 1957.
- [99] R. G. Waggener, M. M. Blough, J. A. Terry, D. Chen, N. E. Lee, S. Zhang, and W. D. McDavid. X-ray spectra estimation using attenuation measurements from 25 kVp to 18 MV. *Med. Phys.*, 26:1269 – 1278, 1999.
- [100] L. Wang and D. Jette. Photon dose calculation based on electron multiple-scattering theory: primary dose deposition kernels. *Med. Phys.*, 26:1454 – 1465, 1999.
- [101] L. Wang, M. Lovelock, and C. S. Chui. Experimental verification of a ct-based monte carlo dose-calculation method in heterogeneous phantoms. *Med. Phys.*, 26:2626 – 2634, 1999.
- [102] S. Webb and R. A. Fox. Verification by Monte Carlo methods of a power law tissue-air ratio algorithm for inhomogeneity corrections in photon beam dose calculations. *Phys. Med. Biol.*, 25:225 – 40, 1980.
- [103] C. M. Wells, T. R. Mackie, M. B. Podgorsak, M. A. Holmes, N. Pananikolaou, P. J. Reckwerdt, J. Cygler, D. W. O. Rogers, A. F. Bielajew, and D. G. Schmidt. Measurements of the electron dose distribution near inhomogeneities using a plastic scintillation detector. *Int. J. Radiat. Oncol. Biol. Phys.*, 29:1157 – 1165, 1994.

- [104] B. L. Werner, F. M. Khan, and F. C. Deibel. A model for calculating electron beam scattering in treatment planning. *Med. Phys.*, 9:180 – 187, 1982.
- [105] J. W. Wong and J. A. Purdy. On methods of inhomogeneity corrections for photon transport. *Med. Phys.*, 17:807 – 814, 1990.
- [106] M. K. Woo and J. R. Cunningham. The validity of the scaling method in primary electron transport for photon and electron beams. *Med. Phys.*, 17:187 – 194, 1990.
- [107] M. K. Woo, J. R. Cunningham, and J. J. Jeziorski. Extending the concept of primary and scatter separation to the condition of electronic disequilibrium. *Med. Phys.*, 17:588 – 595, 1990.
- [108] M. K. Woo, D. J. Scora, and E. Wong. The regional monte carlo method: a dose calculation method based on accuracy requirement. *Med. Phys.*, 25:1866 – 1871, 1998.
- [109] M. E. J. Young and R. O. Kornelsen. Dose corrections for low-density tissue inhomogeneities and air channels for 10 MV x-rays. *Med. Phys.*, 10:450 – 455, 1983.
- [110] C. X. Yu, T. R. Mackie, and J. W. Wong. Photon dose calculation incorporating electron transport. *Med. Phys.*, 22:1157 – 1165, 1995.

## Appendix A

### Derivation of generalized scattering moments for $n$ layers

#### A. Scattering moments in homogeneous phantom

The  $i$ th scattering moment at a given depth  $z$  in a medium having a scattering power  $k(z)$  is defined as

$$A_i(z) = \int_0^z k(z')(z - z')^i dz'. \quad (1)$$

Tables of scattering power and stopping power as a function of electron energy are listed in ICRU Report No 35 [79]. To convert from energy to depth, we use Harder's equation [41] which assumes that the energy of an electron decreases linearly with depth as it travels down the medium. This relationship is given by

$$E = E_o(1 - z/R_p) \quad (2)$$

where  $E_o$  is the energy of the incident electrons,  $R_p$  is the practical range of the electrons.  $R_p$  can also be represented as an analytical formula as a function of  $E_o$ :

$$R_p = C_o + C_1 E_o + C_2 E_o^2, \quad (3)$$

where the constants are given by ICRU35.

In order to evaluate the above integral ( $A_i(z)$ ), numerical techniques can be employed. However, if we can evaluate  $A_i(z)$  explicitly (analytically), a great saving in computation time can be achieved. To do that, we need to convert the table values of the scattering power into an analytical function. An appropriate parametric function would be

$$k(E) = AE^{-B}, \quad (4)$$

where  $A$  and  $B$  can be estimated by using the least squares method. Best estimates derived for water are  $3.2 \text{ radian}^2 \text{ cm}^2/\text{g}$  and 1.6 for  $A$  and  $B$  respectively. In this thesis, scattering moments up to the second order are of interest and their expressions were derived using Mathematica<sup>TM</sup> Version 3 as

$$A_0(z) = A \left( \frac{E_o}{R_p} \right)^{-B} \left( \frac{R_p^{1-B}}{1-B} - \frac{R_p - z^{1-B}}{1-B} \right) \quad (5)$$

$$A_1(z) = A \left( \frac{E_o}{R_p} \right)^{-B} \left( \frac{R_p - z^{2-B}}{(1-B)(2-B)} - \frac{R_p^{1-B}(R_p + (B-2)z)}{(1-B)(2-B)} \right) \quad (6)$$

$$A_2(z) = A \left( \frac{E_o}{R_p} \right)^{-B} \left( \frac{-2(R_p - z)^{3-B}}{(1-B)(2-B)(3-B)} + \frac{R_p^{1-B}(2R_p^2 - 2(3-B)R_p z + (6-5B+B^2)z^2)}{(1-B)(2-B)(3-B)} \right). \quad (7)$$

## B. Scattering moments in inhomogeneous phantom

For a multilayered geometry, Equation 1 cannot be evaluated explicitly; a solution in a series form is sought. Since  $z$  can be expressed as

$$z = t_1 + t_2 + \cdots + t_n \quad (8)$$

the  $i$ th moment will be the sum of  $n$  integrals, hence

$$A_i(z) = \int_0^{t_1} k(z')(z - z')^i dz' + \int_{t_1}^{t_1+t_2} k(z')(z - z')^i dz' +$$

$$\cdots + \int_{z-t_n}^z k(z')(z-z')^i dz'. \quad (9)$$

Making the following substitution for scattering moment of a given layer  $n$  as

$$A_i(t_n) = \int_{t_1+t_2+\dots+t_{n-1}}^{t_1+t_2+\dots+t_n} k(z')(z-z')^i dz' \quad (10)$$

and using recursion we arrive at a general form for  $A_i(z)$  at the depth  $z$  in terms of the lower order moments of the overlying layers. Hence

$$A_i(z) = \sum_{l=1}^n \left( \sum_{j=0}^i A_j(t_l) \right) \cdot \left( \sum_{m=0}^i a_m \left( \sum_{h=l+1}^n t_h \right)^m \right) \cdot \delta_{i,j+m}, \quad (11)$$

where we have set the  $i$ th power factor as follows,

$$\left( 1 + \sum_{h=l+1}^n t_h \right)^i = \sum_{m=0}^i a_m \left( \sum_{h=l+1}^n t_h \right)^m, \quad (12)$$

$a_m$  is the contant factor in the power expansion and  $\delta_{i,j+m}$  is the Kronecker delta, defined by

$$\delta_{pq} = \begin{cases} 1 & p = q \\ 0 & p \neq q \end{cases} \quad (13)$$

For example, the second moment at a depth  $z = t_1 + t_2 + t_3 + t_4$  in a four layer phantom can be expressed as

$$\begin{aligned} A_2(z) = & A_0(t_1)(t_2 + t_3 + t_4)^2 + 2A_1(t_1)(t_2 + t_3 + t_4) + A_2(t_1) + \\ & + A_0(t_2)(t_3 + t_4)^2 + 2A_1(t_2)(t_3 + t_4) + A_2(t_2) + \\ & + A_0(t_3)(t_4)^2 + 2A_1(t_3)t_4 + A_2(t_3) + A_2(t_4), \end{aligned} \quad (14)$$

where  $a_1 = 1$ ,  $a_2 = 2$ , and  $a_3 = 1$  for  $i = 2$ . For  $i = 3$ ,  $a_1 = 1$ ,  $a_2 = 3$ ,  $a_3 = 3$ , and  $a_4 = 1$ .

## **Appendix B**

### **The primary Compton dose calculation code BATOUL.c**

```
*****
```

This code calculates primary Compton dose in a homogeneous and  
heterogeneous phantoms.

It is selfsufficient, requiring only stopping powers and scattering powers of  
materials presently drawn from ICRU 35.

It outputs two 3D dose grids written to two ASCII text files.

It requires a "C" compiler with a math library at time of linking.

```
*****
```

```

#include <stdio.h>
#include <stdlib.h>
#include <string.h>
#include <math.h>
#define pi 3.141592
#define twopi 6.2831853
#define sqrt2pi 2.5066283
#define eps 0.001
#define n3 150
#define s1 50
#define n 1
#define M 1.6022e-10          /* MeV/g = 1.6022e-10 Gy */
#define cso 66.525e-26        /* cm2/el */
#define data 28
#define dwater 1.00            /* g/cm3 */
#define dair 1.205e-3
#define New 3.343e23           /* e/g */
#define Neair 3.006e23
#define Zw 7.51
#define Zair 7.78
#define Aw 3.2004
#define Bw 1.62655
#define Aair 0.0038604464
#define Bair 1.62704
#define xphan 4.0
#define x1phan -3.9901          /* ex -3.9901, 4.101 or 0.0001, 0.001 */
#define x2phan 4.101
#define yphan 4.0
#define y1phan -3.9901
#define y2phan 4.101
#define z1phan 4.1
#define z2phan 4.2
#define x1cut -2.499
#define x2cut 2.501
#define y1cut -2.499
#define y2cut 2.501
#define dslab 3.0
#define gap 5.0
#define dx 0.2

```

```

#define dY 0.2
#define dZ 0.2
#define Nx 41
#define Ny 41
#define Nz 90
#define div 10.0
#define lamda1 0.85          /* 0.8,0.7 - 0.7 - 0.9      */
#define lamda2 1.0           /* 0.7 - 0.7 - 0.9      */
#define Event 1e6
#define Eflag 1               /* 1=mono , 2=poly      */
#define Ihnu 5
#define Ecum 0.01             /* 1.0 - 0.04,0.1 - 0.1 - 0.02 */
#define dEo  0.793993          /* 0.503997-11.3002-0.793993-0.493169-0.527274|
                                         0.326 -0.3056 - 0.207 */

/*-----PROTOTYPES-----*/
extern float      dcسدE (float e);
extern float      dcسدEspt (float e,float hn);
extern float      Rcsda (float eo);
extern int        intenergy (float e);
extern float      energyair (float z, float eo);
extern float      energyw (float z, float eo);
extern float      Aow (float z, float eo);
extern float      A1w (float z, float eo);
extern float      A2w (float z, float eo);
extern float      Aoair (float z, float eo);
extern float      A1air (float z, float eo);
extern float      A2air (float z, float eo);
extern float      sigmainh (float z, float eo);
extern float      A2airC (float z, float eo);
extern float      A2wC (float z, float eo);
extern float      erfcc (float x);
extern float      erfs (float x, float y, float sigma,float wt);
extern float      exps (float x, float y, float sigma,float wt);
extern float      scolairC (float e);
extern float      scolwC (float e);

/*-----DATA-----*/
/* Ihnu          0 1 2 3 4 5 6 7 8 9 10 11 12      */
/*           | | | | | | | | | | | | | | | | */
static float hnu[]={1,2,4,6,10,20,30,4,6,10,15,18,24};

```

```

/* hn > 30 -> spectrum */
static float Muair[]={0.0636,0.0445,0.0308,0.0251,0.0205,0.0171,0.0163,
                      0.051393,0.045026,0.034811,0.028347,0.022477,0.021286};
static float Muw[]={0.0707,0.0494,0.0340,0.0276,0.0222,0.0182,0.0171,
                     0.057154,0.050074,0.038714,0.031525,0.024997,0.031472}; ,
static float CS[]={2.112e-25,1.464e-25,9.598e-26,7.323e-26,5.099e-26};
static float E[]={0.01,0.015,0.02,0.03,0.04,0.05,0.06,0.08,
                  0.1,0.15,0.2,0.3,0.4,0.5,0.6,0.8,
                  1.0,1.5,2.0,3.0,4.0,5.0,6.0,8.0,
                  10.0,15.0,20.0,30.0,40.0};
static float scolw[]={22.56,16.47,13.17,9.653,7.777,6.603,
                     5.797,4.757,4.115,3.238,2.793,2.355,
                     2.148,2.034,1.963,1.886,1.849,1.823,
                     1.824,1.846,1.870,1.892,1.911,1.943,
                     1.968,2.014,2.046,2.089};
static float scolair[]={19.75,14.45,11.57,8.492,6.848,5.819,
                      5.111,4.198,3.633,2.861,2.470,2.084,
                      1.902,1.802,1.743,1.683,1.661,1.661,
                      1.684,1.740,1.790,1.833,1.870,1.931,
                      1.979,2.069,2.134,2.226};
static float sradw[]={3.898e-3,3.944e-3,3.963e-3,3.984e-3,
                     4.005e-3,4.031e-3,4.062e-3,4.138e-3,
                     4.228e-3,4.494e-3,4.801e-3,5.514e-3,
                     6.339e-3,7.257e-3,8.254e-3,1.043e-2,
                     1.280e-2,1.942e-2,2.678e-2,4.299e-2,
                     6.058e-2,7.917e-2,9.854e-2,1.391e-1,
                     1.814e-1,2.926e-1,4.086e-1,6.489e-1};
static float sradair[]={3.897e-3,3.937e-3,3.954e-3,3.976e-3,
                      3.998e-3,4.025e-3,4.057e-3,4.133e-3,
                      4.222e-3,4.485e-3,4.789e-3,5.495e-3,
                      6.311e-3,7.223e-3,8.210e-3,1.036e-2,
                      1.271e-2,1.927e-2,2.656e-2,4.260e-2,
                      5.999e-2,7.838e-2,9.754e-2,1.376e-1,
                      1.795e-1,2.895e-1,4.042e-1,6.417e-1};
static float Tw[]={5.91e3,2.92e3,1.77e3,8.69e2,5.16e2,3.57e2,
                  2.61e2,1.59e2,1.09e2,5.57e1,3.50e1,1.84e1,
                  1.18e1,8.45,6.42,4.17,2.99,1.61,1.03,5.40e-1,
                  3.36e-1,2.31e-1,1.69e-1,1.03e-1,6.95e-2,3.37e-2,
                  2.00e-2,9.54e-3};
static float Tair[]={5.94e3,2.93e3,1.77e3,8.73e2,5.28e2,3.59e2,

```

```

2.62e2,1.60e2,1.10e2,5.60e1,3.51e1,1.85e1,
1.19e1,8.48,6.45,4.19,3.00,1.62,1.04,5.42e-1,
3.37e-1,2.32e-1,1.70e-1,1.03e-1,6.98e-2,
3.38e-2,2.01e-2,9.57e-3};
/*-----*/
float alpha,Emax,Z,EG[5][3],wtG[5][3],dp,Wtair,Wtw,Mu,arrspect[2][100],
dcsdEarr[100];
/*-----*/
main()
{
    int i,j,k,I,J,Jo,intXc,intYc,intZ,IE,IEmax,maxbin;
    float l,c,x,y,dy,nx,ny,nz,nbv,A,C,Ei,EN,ENair,ENw,CF,Fw,Fair,S,
          sigma,Xc,Yc,Scolw,Scolair,Scol,DOSE[Nx][Ny][Nz],DOSEinh[Nx][Ny][Nz],
          dcs,Nem2w,Nem2air,Constw,Constair,pfluence,dE,nb,bin,sumwt,hn,emax;
    char m,s[s1],s1[s1],s2[s1],s3[s1],s4[s1],s5[s1];
    FILE *fin,*finspt,*fdata,*foutair,*foutw,*fCF;

    printf("Enter the name of the 3ddose file: ");
    scanf("%s",&s);
    strcpy(s1,s);
    strcpy(s2,s);
    strcpy(s3,s);
    strcpy(s4,s);
    strcpy(s5,s);
    strcat(s1,".3ddose");
    strcat(s2,".csdat");
    strcat(s3,".inh3ddose");
    strcat(s4,".w3ddose");
    strcat(s5,"TCF.3ddose");

    fin= fopen (s1,"r");
    fdata= fopen (s2,"w");
    foutair=fopen (s3,"w");
    foutw= fopen (s4,"w");
    fCF= fopen (s5,"w");
    finspt=fopen ("/home/bilal/egs4/ensrc_spectra/mohan4.spectrum","r");

    Nem2w= New*dwater*dZ;                                /* e/cm2 */
    Nem2air= Neair*dair*dZ;
    pfluence=Event/((x2cut-x1cut)*(y2cut-y1cut));      /* photons/c

```

```

Constw =pfluence*M*Nem2w;
Constair=pfluence*M*Nem2air;
alpha= hnu[Ihnu]/0.511;
Emax = hnu[Ihnu]*2*alpha/(1+2*alpha);

for(i=0;i<100;i++)
    dcsdEarr[i]=arrspect[0][i]=arrspect[1][i]=0.0;
if (Eflag==1)
{
    IE=0;
    for (Ei=dEo/2.0;Ei<=Emax;Ei=Ei+dEo)
    {
        dcsdEarr[IE]=dcsdE(Ei);
        fprintf(fdata," %g      %g\n",Ei,dcsdE(Ei));
        IE++;
    }
    IEmax=IE-1;
}
if (Eflag==2)
{
    j=0;
    sumwt=0.0;
    while((nb=fscanf(finspt,"%f, %f",&x,&y))==2)
    {
        arrspect[0][j]=x;
        arrspect[1][j]=y;
        sumwt=sumwt+y;
        j++;
    }
    bin=arrspect[0][1]-arrspect[0][0];
    maxbin=j-1;
    IE=0;
    for(Ei=dEo/2.0;Ei<=Emax;Ei=Ei+dEo)
    {
        for (k=0;k<=maxbin;k++)
        {
            if (k>0)
                bin=arrspect[0][k]-arrspect[0][k-1];
            hn=arrspect[0][k]-bin/2.0;
            emax=(2*hn*hn/0.511)/(1+2*hn/0.511);

```

```

        if (emax>Ei)
            dcsdEarr[IE]=dcsdEarr[IE]+dcsdEspt(Ei,hn)*arrspect[1][k]
/sumwt;
    }
    fprintf(fdata,"%f      %g\n",Ei,dcsdEarr[IE]);
    IE++;
}
IEmax=IE-1;
printf("%d %f %f %g %g MV Spectrum\n",maxbin,bin,sumwt,
dcsdEarr[IEmax],arrspect[0][maxbin]);
}

/*-----GAUSSIAN QUADRATURE DATA-----*/
/*  1 MeV photons Ihnu=0 */
EG[0][0]=0.08979; EG[0][1]=0.4109; EG[0][2]=0.7283;
wtG[0][0]=0.2572; wtG[0][1]=0.3908; wtG[0][2]=0.352;

/*  2 MeV photons Ihnu=1 */
EG[1][0]=0.2091; EG[1][1]=0.9471; EG[1][2]=1.636;
wtG[1][0]=0.2208; wtG[1][1]=0.3762; wtG[1][2]=0.403;

/*  4 MeV photons Ihnu=2 */
EG[2][0]=0.4603; EG[2][1]=2.073; EG[2][2]=3.503;
wtG[2][0]=0.1879; wtG[2][1]=0.3519; wtG[2][2]=0.4602;

/*  6 MeV photons Ihnu=3 */
EG[3][0]=0.717; EG[3][1]=3.223; EG[3][2]=5.393;
wtG[3][0]=0.1714; wtG[3][1]=0.3352; wtG[3][2]=0.4934;

/*  10 MeV photons Ihnu=4 */
EG[4][0]=1.237; EG[4][1]=5.552; EG[4][2]=9.205;
wtG[4][0]=0.1537; wtG[4][1]=0.3133; wtG[4][2]=0.533;
/*-----*/
fscanf(fin, " %g %g %g",&nx,&ny,&nz);
fprintf(foutw," %g %g %g\n",nx,ny,nz);
fprintf(foutair," %g %g %g\n",nx,ny,nz);
fprintf(fCF," %g %g %g\n",nx,ny,nz);
for (i=0;i<=nx;i++)
{

```

```

        fscanf(fin," %g",&x);
        fprintf(foutw," %g",x);
        fprintf(foutair," %g",x);
        fprintf(fCF," %g",x);
    }
    fprintf(foutw,"\n");
    fprintf(foutair,"\n");
    fprintf(fCF,"\n");
    for (i=0;i<=ny;i++)
    {
        fscanf(fin," %g",&x);
        fprintf(foutw," %g",x);
        fprintf(foutair," %g",x);
        fprintf(fCF," %g",x);
    }
    fprintf(foutw,"\n");
    fprintf(foutair,"\n");
    fprintf(fCF,"\n");
    for (i=0;i<=nz;i++)
    {
        fscanf(fin," %g",&x);
        fprintf(foutw," %g",x);
        fprintf(foutair," %g",x);
        fprintf(fCF," %g",x);
    }
    fprintf(foutw,"\n");
    fprintf(foutair,"\n");
    fprintf(fCF,"\n");

/*
    for (i=0;i<Nx;i++)
        for (j=0;j<Ny;j++)
            for (k=0;k<Nz;k++)
            {
                fscanf(fin," %g",&y);
                DDOSE[i][j][k]=y;
            }
    for (i=0;i<Nx;i++)
        for (j=0;j<Ny;j++)
            for (k=0;k<Nz;k++)

```

```

    {
        fscanf(fin, " %g", &dy);
    }
/*
for (i=0;i<Nx;i++)
    for (j=0;j<Ny;j++)
        for (k=0;k<Nz;k++)
            DOSE[i][j][k]=DOSEinh[i][j][k]=0.0;
for (Z=z1phan;Z<z2phan;Z=Z+dZ)
{
    intZ=Z/dZ;
/*-----*/
Ei=-dEo/2.0;
for(IE=0;IE<=IEmax;IE++)
{
    Ei=Ei+dEo;
    dcs=dcsdEarr[IE]*dEo;
/*-----*/
/*
    for(IE=0;IE<3;IE++)
    {
        Ei=EG[Ihnu][IE];
        dcs=CS[Ihnu]*wtG[Ihnu][IE];
    */
/*-----*/
Wtw=Consttw*dcs;
Wtair=Consttair*dcs;
Scolw=scolwC(Ei);
Scolair=scolairC(Ei);
for (dp=dZ;dp<=Z;dp=dp+dZ)
{
    ENw=energyw(dp,Ei);
    if (ENw<Ecut)
        break;
    Mu=exp(-dwater*Muw[Ihnu]*(Z-dp));
    sigma=sqrt(A2w(dp,Ei));
    Scol=scolwC(ENw);
    for (Xc=x1phan;Xc<=x2phan;Xc=Xc+dX)
    {
        intXc=(Xc+xphan)/dX;

```

```

        for (Yc=y1phan;Yc<=y2phan;Yc=Yc+dY)
        {
            intYc=(Yc+yphan)/dY;
DOSE[intXc][intYc][intZ]=DOSE[intXc][intYc][intZ]
+Scol*Mu*erfs(Xc,Yc,sigma,Wtw);
        }
    }
C=Scolw*exp(-dwater*Muw[Ihnu]*Z)*Wtw;
for (Xc=x1cut;Xc<=x2cut;Xc=Xc+dX)
{
    intXc=(Xc+xphan)/dX;
    for (Yc=y1cut;Yc<=y2cut;Yc=Yc+dY)
    {
        intYc=(Yc+yphan)/dY;
        DOSE[intXc][intYc][intZ]=DOSE[intXc][intYc][intZ]
+C;
    }
}

if (Z<dslab)
    for (i=0;i<Nx;i++)
        for (j=0;j<Ny;j++)
            DOSEinh[i][j][intZ]=DOSE[i][j][intZ];
else
    if(Z<dslab+gap)
    {
        for (dp=dZ;dp<=Z;dp=dp+dZ)
            if (dp<(Z-dlab))
            {
/*
    Electron originating in air      */
        ENair=energyair(dp,Ei);
        if (ENair<Ecut)
            break;
        Mu=exp(-dair*Muair[Ihnu]*(Z-dlab-dp)-
dwater*Muw[Ihnu]*dlab);
        sigma=sqrt(A2air(dp,Ei));
        Scol=scolairC(ENair);
        for (Xc=x1phan;Xc<=x2phan;Xc=Xc+dX)
        {

```

```

intXc=(Xc+xphan)/dX;
for (Yc=y1phan;Yc<=y2phan;Yc=Yc+dY)
{
    intYc=(Yc+yphan)/dY;
DOSEinh[intXc][intYc][intZ]=DOSEinh[intXc][intYc][intZ]
+Scol*Mu*erfs(Xc,Yc,sigma,Wtair);
}
}
else
{
/*
Electron originating in water */
EN=energyw(dp-Z+dslab,Ei);
if (EN<Ecut)
    break;
ENair=energyair(Z-dslab,EN);
if (ENair<Ecut)
    break;
Mu=exp(-dwater*Muw[Ihnu]*(Z-dp));
sigma=sigmainh(dp,Ei);
Scol=scolairC(ENair);
for (Xc=x1phan;Xc<=x2phan;Xc=Xc+dX)
{
    intXc=(Xc+xphan)/dX;
    for (Yc=y1phan;Yc<=y2phan;Yc=Yc+dY)
    {
        intYc=(Yc+yphan)/dY;
DOSEinh[intXc][intYc][intZ]=DOSEinh[intXc][intYc][intZ]
+Scol*Mu*erfs(Xc,Yc,sigma,Wtw)*lamda1;
    }
}
A=Scolair*exp(-dair*Muair[Ihnu]*(Z-dslab)-
dwater*Muw[Ihnu]*dslab)*Wtair;
for (Xc=x1cut;Xc<=x2cut;Xc=Xc+dX)
{
    intXc=(Xc+xphan)/dX;
    for (Yc=y1cut;Yc<=y2cut;Yc=Yc+dY)
    {
        intYc=(Yc+yphan)/dY;
}
}
}
}

```



```

        for (Xc=x1phan;Xc<=x2phan;Xc=Xc+dX)
        {
            intXc=(Xc+xphan)/dX;
            for (Yc=y1phan;Yc<=y2phan;Yc=Yc+dY)
            {
                intYc=(Yc+yphan)/dY;
DOSEinh[intXc][intYc][intZ]=DOSEinh[intXc][intYc][intZ]
+Scol*Mu*erfs(Xc,Yc,sigma,Wtair);
            }
        }
    }
    else
    {
/* Electron originating in water I */
        EN=energyw(dp-Z+dslab,Ei);
        if (EN<Ecut)
            break;
        ENair=energyair(gap,EN);
        if (ENair<Ecut)
            break;
        ENw=energyw(Z-dslab-gap,ENair);
        if (ENw<Ecut)
            break;
        Mu=exp(-dwater*Muw[Ihnu]*(Z-dp));
        sigma=sigmainh(dp,Ei);
        Scol=scolwC(ENw);
        for (Xc=x1phan;Xc<=x2phan;Xc=Xc+dX)
        {
            intXc=(Xc+xphan)/dX;
            for (Yc=y1phan;Yc<=y2phan;Yc=Yc+dY)
            {
                intYc=(Yc+yphan)/dY;
DOSEinh[intXc][intYc][intZ]=DOSEinh[intXc][intYc][intZ]
+Scol*Mu*erfs(Xc,Yc,sigma,Wtw)*lamda2;
            }
        }
    }
    A=Scolw*exp(-dair*Muair[Ihnu]*(gap)-
dwater*Muw[Ihnu]*(Z-gap))*Wtw;
    for (Xc=x1cut;Xc<=x2cut;Xc=Xc+dX)

```

```

        {
            intXc=(Xc+xphan)/dX;
            for (Yc=y1cut;Yc<=y2cut;Yc=Yc+dY)
            {
                intYc=(Yc+yphan)/dY;
                DOSEinh[intXc][intYc][intZ]=
DOSEinh[intXc][intYc][intZ]+A;
            }
        }
    }

/*-----OUTPUT-----*/
    for (k=0;k<Nz;k++)
        for (j=0;j<Ny;j++)
            for (i=0;i<Nx;i++)
            {
                fprintf(foutw," %g",DOSE[i][j][k]/pfluence);
                if ((i % 5)==0)
                    fprintf(foutw,"\n");
                fprintf(foutair," %g",DOSEinh[i][j][k]/pfluence);
                if ((i % 5)==0)
                    fprintf(foutair,"\n");
                fprintf(fCF," %g", (DOSEinh[i][j][k]+1e-30)/
(DOSE[i][j][k]+1e-30));
                if ((i % 5)==0)
                    fprintf(fCF,"\n");
            }
/*-----*/
    return EXIT_SUCCESS;
}
***** FUNCTIONS *****
int intenergy (float e)
{
    int i,j;
    for (i=0;i<data;i++)
        if (e>=E[i] && e<E[i+1])
            j=i;
    return j;
}

```

```

/*****************************************/
float dcsdE (float e)
{
    float hn,t1,t2,t3;
    hn    = hnu[Ihnu];
    t1    = e/(alpha*(hn-e));
    t2    = t1*t1;
    t3    = e*e/(hn*(hn-e));
    return (3/8.0)*(cso/(alpha*hn))*(2-2*t1+t2+t3);
}
/*****************************************/
float dcsdEspt (float e,float hn)
{
    float t1,t2,t3,alp;
    alp   = hn/0.511;
    t1    = e/(alp*(hn-e));
    t2    = t1*t1;
    t3    = e*e/(hn*(hn-e));
    return (3/8.0)*(cso/(alp*hn))*(2-2*t1+t2+t3);
}
/*****************************************/
float Rcsda (float eo)
{
    int i,j;
    float sum,de;
    sum=0;
    j=intenergy(eo);
    de=E[0];
    for (i=0;i<=j;i++)
    {
        sum=sum+de/((scolw[i]+sradw[i])*dwater);
        de=E[i+1]-E[i];
    }
    return sum;
}
/*****************************************/
float energyair (float z, float eo)
{
    int j;
    float zeff,i,dz,sum,Rp,e;

```

```

sum=0;
dz=z/div;
j=intenergy(eo);
for (i=0;i<z;i=i+dz)
    sum=sum+dz*(scolair[j]+sradair[j])*dair/((scolw[j]+sradow[j])*dwater);
zeff=sum;
Rp=-0.11+0.505*eo-0.0003*eo*eo;
if (eo<1)
    Rp=Rcsda(eo);
e=eo*(1-zeff/Rp);
return e;
}
/*********************************************
float energyw (float z, float eo)
{
    float Rp,e;
    Rp=-0.11+0.505*eo-0.0003*eo*eo;
    if (eo<1)
        Rp=Rcsda(eo);
    e=eo*(1-z/Rp);
    return e;
}
/*********************************************
float Aow (float z, float eo)
{
    int j;
    float i,sum,dz,e;
    sum=0;
    dz=z/div;
    for (i=0;i<z;i=i+dz)
    {
        e=energyw(i,eo);
        sum=sum+dz*Aow*pow(e,-Bw);
    }
    return sum;
}
/*********************************************
float A1w (float z, float eo)
{
    int j;

```

```

float i,sum,dz,e;
sum=0;
dz=z/div;
for (i=0;i<z;i=i+dz)
{
    e=energyw(i,eo);
    sum=sum+dz*Aw*pow(e,-Bw)*(z-i);
}
return sum;
}
/*********************************************
float A2w (float z, float eo)
{
    int j;
    float i,sum,dz,e;
    sum=0;
    dz=z/div;
    for (i=0;i<z;i=i+dz)
    {
        e=energyw(i,eo);
        sum=sum+dz*Aw*pow(e,-Bw)*(z-i)*(z-i);
    }
    return sum;
}
/*********************************************
float Aoair (float z, float eo)
{
    int j;
    float i,sum,dz,e;
    sum=0;
    dz=z/div;
    for (i=0;i<z;i=i+dz)
    {
        e=energyair(i,eo);
        sum=sum+dz*Aair*pow(e,-Bair);
    }
    return sum;
}
/*********************************************
float A1air (float z, float eo)

```

```

{
    int j;
    float i,sum,dz,e;
    sum=0;
    dz=z/div;
    for (i=0;i<z;i=i+dz)
    {
        e=energyair(i,eo);
        sum=sum+dz*Aair*pow(e,-Bair)*(z-i);
    }
    return sum;
}
/*********************************************************/
float A2air (float z, float eo)
{
    int j;
    float i,sum,dz,e;
    sum=0;
    dz=z/div;
    for (i=0;i<z;i=i+dz)
    {
        e=energyair(i,eo);
        sum=sum+dz*Aair*pow(e,-Bair)*(z-i)*(z-i);
    }
    return sum;
}
/*********************************************************/
float sigmainh ( float dpt, float eo)
{
    float t1,t2,t3,g,ew1,ew2,eair,A2,K,L;
    t1=dpt+dslab-Z;
    ew1 = energyw(t1,eo);
    if (Z>=dslab && Z<(dslab+gap))
    {
        t2=Z-dslab;
        A2=Aow(t1,eo)*t2*t2+A1w(t1,eo)*2*t2+A2w(t1,eo)+A2air(t2,ew1);
    }
    if (Z>=dslab+gap)
    {
        t3=Z-dslab-gap;
    }
}

```

```

if (dpt<(t3+gap))
{
    t2=dpt-t3;
    eair=energyair(t2,eo);
    A2=Aoair(t2,eo)*t3*t3+A1air(t2,eo)*2*t3+A2air(t2,eo)+A2w(t3,ew1);
}
else
{
    t2=gap;
    eair= energyair(gap,ew1);
    K = Aow(t1,eo)*(t2+t3)*(t2+t3)+Aoair(t2,ew1)*t3*t3;
    L = A1w(t1,eo)*2*(t2+t3) + A1air(t2,ew1)*2*t3;
    A2=K+L+ A2w(t1,eo) + A2air(t2,ew1) + A2w(t3,eair);
}
}
return sqrt(A2);
}
/*********************************************
float erfs(float x,float y, float sigma, float wt)
{
    double Ixgauss,Iygauss;
    Ixgauss=2-erfcc((-x1cut+x)/sigma)-erfc((x2cut-x)/sigma);
    Iygauss=2-erfcc((-y1cut+y)/sigma)-erfc((y2cut-y)/sigma);
    return 0.25*wt*Ixgauss*Iygauss;
}
/*********************************************
float erfcc(float x)
{
    float t,z,ans;

    z=fabs(x);
    t=1.0/(1.0+0.5*z);
    ans=t*exp(-z*z-1.26551223+t*(1.00002368+t*(0.37409196+t*(0.09678418+
        t*(-0.18628806+t*(0.27886807+t*(-1.13520398+t*(1.48851587+
        t*(-0.82215223+t*0.17087277)))))));
    return x >= 0.0 ? ans : 2.0-ans;
}
/*********************************************
float exps(float x,float y, float sigma,float wt)
{

```

```

float I,i,j,dx,dy;
I=0.0;
dx=dy=0.01;
for (i=x1cut+dx/2.0;i<=x2cut-dx/2.0+eps;i=i+dx)
    for (j=y1cut+dy/2.0;j<=y2cut-dy/2.0+eps;j=j+dy)
        I=I+exp(-((x-i)*(x-i)+(y-j)*(y-j))/(sigma*sigma))*dx*dy*wt;
return I/(twopi*sigma*sigma/2.0);
}
/*****************************************/
float A2airC (float z,float eo)
{
    int j;
    float i,dz,zeff,Rp,e,sig2,t1,t2,t3,t4,sum,Zp,dZp;
    sum=0;
    dZp=z/div;
    for (Zp=0;Zp<z;Zp=Zp+dZp)
        sum=sum+pow(energyair(Zp,eo),-Bair)*(z-Zp)*(z-Zp)*dZp;
    return Aair*sum;
}
/*****************************************/
float A2wC (float z, float eo)
{
    float Rp,e,sig2,t1,t2,t3,t4,sum,Zp,dZp;

    if (eo>=1)
        Rp=-0.11+0.505*eo-0.0003*eo*eo;
    else
        Rp=Rcsda(eo);
    e=eo*(1-z/Rp);
    sum=0;
    dZp=0.01;
    for (Zp=0;Zp<=z;Zp=Zp+dZp)
        sum=sum+pow(1-Zp/Rp,-Bw)*(z-Zp)*(z-Zp)*dZp;
    return Aw*pow(eo,-Bw)*sum;
}
/*****************************************/
float scolairC (float e)
{
    int i;
    float a,b,y;

```

```

for (i=0;i<data;i++)
    if (e>E[i] && e<=E[i+1])
    {
        a=(scolair[i]-scolair[i+1])/(E[i]-E[i+1]);
        b=scolair[i]-a*E[i];
        return a*e+b;
    }
}
//*********************************************************************
float scolwC (float e)
{
    int i;
    float a,b,y;
    for (i=0;i<data;i++)
        if (e>E[i] && e<=E[i+1])
        {
            a=(scolw[i]-scolw[i+1])/(E[i]-E[i+1]);
            b=scolw[i]-a*E[i];
            return a*e+b;
        }
}
//*********************************************************************

```

## **Appendix C**

### **The GEANT Monte Carlo usercode DOSE.f**

\*\*\*\*\*

This program simulates the dose distribution in a water tank.

Instruction to run the program:

'nohup rundose < dose.input'

Put originally by: D. Axen

In present form by: B. Shahine

\*\*\*\*\*

```

program dose
*
PARAMETER (NMEMOR=6000000)
COMMON/PAWC/H(NMEMOR)
COMMON/GCBANK/Q(8000000)
*
* -----
*
CALL TIMEST(1E6)
*
CALL GZEBRA(8000000)
CALL HLIMIT(-NMEMOR)
call hplint(0)
*      Geant initialization
CALL UGINIT
*      Test printings.
*      CALL GPRINT('PART',0)
*      CALL GPRINT('MATE',0)
*      CALL GPRINT('TMED',0)
*      CALL GPRINT('VOLU',0)
*      Start events processing
CALL GRUN
*      End of run
CALL UGLAST
*
END
C
SUBROUTINE GUHADR
C.
C. ****
C. *
C. *      User routine to generate one hadronic interaction *
C. *
C. * ==>Called by : GTHADR,GTNEUT *
C. *
C. ****
C.
CALL GHEISH

```

```

    END
CDECK  ID>, GUKINE.
      SUBROUTINE GUKINE
*
***** ****
*
*          GEANT3 user routine to generate Kinematics
*          for primary tracks
*
***** ****
*
      COMMON/GCFLAG/IDEBUG, IDEMIN, IDEMAX, ITEST, IDRUN, IDEVT, IEORUN
      +           ,IEOTRI, IEVENT, ISWIT(10), IFINIT(20), NEVENT, NRNDM(2)
C
      COMMON/GCKINE/IKINE, PKINE(10), ITRA, ISTAK, IVERT, IPART, ITRTYP
      +           ,NAPART(5), AMASS, CHARGE, TLIFE, VERT(3), PVERT(4), IPAOLD
C
      common	flags/flword(20)
      common/even/nev,ide,ipoint
      common/source/einc,bin,enflag
      Common/runpar/iaxis,matcav,igeom
      common/posit/xpos,ypos,zpos,xcut,ycut
      common/tank/xtank,ytank,ztank
      common/phan/iphant,ilung,zphan,rotang
      common/cavi/cavpos,xcav,ycav,zcav
      common/tumor/itumor,rtumor,xtumor,ytumor,ztumor,tratio
      DIMENSION VERTEX(6),PLAB(3),RNDM(6)
*
-----  

C      reset the flagwords
      call vzero(flword,20)
C      set the incident particle type
      IK=IKINE
C      calculate the incident gamma energy
      if(enflag.eq. 0) then
      egamma=einc
          else if(einc.eq. 0.006) then
          call mohan6(egamma)
              else if(einc.eq. 0.004) then
          call mohan4(egamma)
      else if(einc.eq. 0.010) then

```

```

call mohan10(egamma)
else if(einc.eq. 0.015) then
call mohan15(egamma)
else if(einc.eq. 0.018) then
call wag18(egamma)
else if(einc.eq. 0.024) then
call mohan24(egamma)
end if
call hfill(1,egamma,0.,1.)
CALL VZERO(VERTEX,6)
C determine if point source or parallel or pencil source
C ipoint=1 --> point source chosen

if(ipoint.eq.1) then
vertex(1) = xpos
vertex(2) = ypos
vertex(3) = -1.* (zpos - cavpos - zcav)
thmax = atan(sqrt( xcut**2 + ycut**2)/zpos)
29 continue
CALL GRNDM(RNDM,2)
ar = 1. - cos(thmax)
theta = acos(1. - ar*rndm(1))
trakln = zpos/cos(theta)
phi = rndm(2)*2.*3.14159
x = trakln*sin(theta)*cos(phi)
if(abs(x).gt.xcut) go to 29
y = trakln*sin(theta)*sin(phi)
if(abs(y).gt.ycut) go to 29
z = zpos
flen = sqrt( x**2 + y**2 + z**2 )
end if
if(ipoint.eq.2) then
CALL GRNDM(RNDM,2)
x=2*xcut*(rndm(1)-0.5)
y=2*ycut*(rndm(2)-0.5)
z = zpos
flen = z
vertex(1) = x
vertex(2) = y
vertex(3) = -1.* (zpos - cavpos - zcav)

```

```

        x=0
        y=0
    end if
    if(ipoint.eq.3) then
        x = xpos
        y = ypos
        z = zpos
        flen = z
        vertex(1) = x
        vertex(2) = y
        vertex(3) = -1.* (zpos - cavpos - zcav)
    end if
*
PLAB(1) = egamma*x/flen
PLAB(2) = egamma*y/flen
PLAB(3) = egamma*z/flen
*
CALL GSVERT(VERTEX,0,0,0,0,NVERT)
CALL GSKINE(PLAB,IK,NVERT,0,0,NT)
*
*           Kinematic debug (controled by ISWIT(1))
*
IF(IDEBUG.EQ.1.AND.ISWIT(1).EQ.1) THEN
    CALL GPRINT('VERT',0)
    CALL GPRINT('KINE',0)
ENDIF
*
END
CDECK ID>, GUOUT.
SUBROUTINE GUOUT
*
*****
*
*           GEANT3 user routine called at the end of each event.
*
*****
*
COMMON/GCUNIT/LIN,LOUT,NUNITS,LUNITS(5)
INTEGER LIN,LOUT,NUNITS,LUNITS

```

```

COMMON/GCMAIL/CHMAIL
CHARACTER*132 CHMAIL
C
COMMON/GCFLAG/IDEBUG, IDEMIN, IDEMAX, ITEST, IDRUN, IDEVT, IEORUN
+      ,IEOTRI, IEVENT, ISWIT(10), IFINIT(20), NEVENT, NRNDM(2)
C
C
COMMON/GCKINE/IKINE,PKINE(10),ITRA,ISTAK,IVERT,IPART,ITRTYP
+      ,NAPART(5),AMASS,CHARGE,TLIFE,VERT(3),PVERT(4),IPAOLD
C
*
common/flags/flword(20)
common/runpar/iaxis,matcav,geom
common/posit/xpos,ypos,zpos,xcut,ycut
common/phan/iphant,ilung,zphan,rotang
dimension rndm(4)
* Logic for displaying the event
IF(IDEBUG.EQ.1) THEN
  IF(ISWIT(2).EQ.1) CALL GPRINT('JXYZ', 0)
  IF(ISWIT(3).EQ.1) THEN
    CALL GDSHOW(1)
    CALL GDXYZ (0)
  *
  *      print *, ' print any key to show event'
  *      read (5,'(a1)')
    CALL ICLRWK(0,0)
  ENDIF
ENDIF
40  continue
30  continue
* end of display logic
END
*
CDECK ID>, GUPHAD.
      SUBROUTINE GUPHAD
C.
C. ****
C. *
C. *      User routine to compute Hadron. inter. probabilities *
C. * *
C. * ==>Called by : GTHADR,GTNEUT *

```

```

C.      *
C. ****
C.
C. -----
C.
COMMON/GCPHYS/IPAIR,SPAIR,SLPAIR,ZINTPA,STEPPA
+           ,ICOMP,SCOMP,SLCOMP,ZINTCO,STEPCO
+           ,IPHOT,SPHOT,SLPHOT,ZINTPH,STEPPH
+           ,IPFIS,SPFIS,SLPFIS,ZINTPF,STEPPF
+           ,IDRAY,SDRAY,SLDRAY,ZINTDR,STEPDR
+           ,IANNI,SANNI,SLANNI,ZINTAN,STEPAN
+           ,IBREM,SBREM,SLBREM,ZINTBR,STEPBR
+           ,IHADR,SHADR,SLHADR,ZINTHA,STEPHA
+           ,IMUNU,SMUNU,SLMUNU,ZINTMU,STEPMU
+           ,IDCAY,SDCAY,SLIFE ,SUMLIF,DPHYS1
+           ,ILOSS,SLOSS,SOLOSS,STLOSS,DPHYS2
+           ,IMULS,SMULS,SOMULS,STMULS,DPHYS3
+           ,IRAYL,SRAYL,SLRAYL,ZINTRAL,STEPRA
COMMON/GCPHLT/ILABS,SLABS,SLLABS,ZINTLA,STEPLA
+           ,ISYNC
+           ,ISTRA
*
C
      IF (IHADR.NE.4) THEN
          CALL GPGHEI
      ELSE
          CALL FLDIST
      ENDIF
      END
CDECK  ID>, GUSTEP.
      SUBROUTINE GUSTEP
*
***** ****
*
*           GEANT3 user routine called at the end of each tracking step *
*
***** ****
*
      PARAMETER (KWBANK=69000,KWWORK=5200)

```

```

COMMON/GCBANK/NZEBRA,GVERSN,ZVERSN,IXSTOR,IXDIV,IXCONS,FENDQ(16)
+           ,LMAIN,LR1,WS(KWBANK)
DIMENSION IQ(2),Q(2),LQ(8000),IWS(2)
EQUIVALENCE (Q(1),IQ(1),LQ(9)),(LQ(1),LMAIN),(IWS(1),WS(1))
EQUIVALENCE (JCG,JGSTAT)
COMMON/GCLINK/JDIGI ,JDRAW ,JHEAD ,JHITS ,JKINE ,JMATE ,JPART
+           ,JROTM ,JRUNG ,JSET ,JSTAK ,JGSTAT,JTMED ,JTRACK,JVERTX
+           ,JVOLUM,JXYZ ,JGPAR ,JGPAR2,JSKLT
C
COMMON/GCTMED/NUMED,NATMED(5),ISVOL,IFIELD,FIELDM,TMAXFD,STEMAX
+           ,DEEMAX,EPSIL,STMIN,CFIELD,PREC,IUPD,ISTPAR,NUMOLD
COMMON/GCTLIT/THRIND,PMIN,DP,DNDL,JMIN,ITCKOV,IMCKOV,NPCKOV
C
INTEGER MXGKIN
PARAMETER (MXGKIN=100)
COMMON/GCKING/KCASE,NGKINE,GKIN(5,MXGKIN),
+           TOFD(MXGKIN),IFLGK(MXGKIN)
INTEGER      KCASE,NGKINE ,IFLGK,MXPHT,NGPHOT
REAL         GKIN,TOFD,XPHOT
C
PARAMETER (MXPHT=800)
COMMON/GCKIN2/NGPHOT,XPHOT(11,MXPHT)
C
COMMON/GCKIN3/GPOS(3,MXGKIN)
REAL          GPOS
C
COMMON/GCFLAG/IDEBUG,IDEWIN,IDEWMAX,ITEST,IDRUN,IDEVT,IEORUN
+           ,IEOTRI,IEVENT,ISWIT(10),IFINIT(20),NEVENT,NRNDM(2)
C
COMMON/GCKINE/IKINE,PKINE(10),ITRA,ISTAK,IVERT,IPART,ITRTYP
+           ,NAPART(5),AMASS,CHARGE,TLIFE,VERT(3),PVERT(4),IPAOLD
C
PARAMETER (MAXMEC=30)
COMMON/GCTRACK/VECT(7),GETOT,GEKIN,VOUT(7),NMEC,LMEC(MAXMEC)
+           ,NAMEC(MAXMEC),NSTEP ,MAXNST,DESTEP,DESTEL,SAFETY,SLENG
+           ,STEP ,SNEXT ,SFIELD,TOFG ,GEKRAT,UPWGHT,IGNEXT,INWVOL
+           ,ISTOP ,IGAUTO,IEKBIN, ILOSL, IMULL,INGOTO,NLDOWN,NLEVIN
+           ,NLVS,ISTORY
PARAMETER (MAXME1=30)
COMMON/GCTPOL/POLAR(3), NAMEC1(MAXME1)

```

```

C
COMMON/GCVOLU/NLEVEL,NAMES(15),NUMBER(15),
+LVOLUM(15),LINDEX(15),INFROM,NLEVMAX,NLDEV(15),LINMX(15),
+GTRAN(3,15),GRMAT(10,15),GONLY(15),GLX(3)
character*4 names
*
common/flags/flword(20)
common/phan/iphany,ilung,zphan,rotang
common/slice/slipo,slithk,nx,nz
common/tank/xtank,ytank,ztank
common/posit/xpos,ypos,zpos,xcut,ycut
common/cavi/cavpos,xca,ycav,zca
common/even/nev,ide,ioint
* 3Dhistogram
common/xyzv/nbx,nby,nbz,fbinx,fbiny,fbinz
common/xyzdos/xyzdose(90,90,100)
common/count/counter
* -----
*           Something generated ?
IF(NGKINE.GT.0) THEN
    DO 5 I=1,NGKINE
        ITYPA = GKIN(5,I)
        IF(ITYPA.LE.4) CALL GSKING(I)
5      CONTINUE
* histogram the number of mechanism at this step
        ENDIF
* is the tracking medium water tank?
* 3D energy grid
        if(abs(vect(1)).le.xtank) then
            if(abs(vect(2)).le.ytank) then
                if(abs(vect(3)).le.ztank) then
                    wt = 1000.*destep
                    i=INT((vect(1)+xtank)*fbinx+1)
                    j=INT((vect(2)+ytank)*fbiny+1)
                    k=INT((vect(3)+ztank)*fbinz+1)
                    xyzdose(i,j,k)=xyzdose(i,j,k)+wt
                end if
            end if
        end if
*           Debug/plot event

```

```

        CALL GDEBUG
*
        END
CDECK  ID>, GUTREV.
        SUBROUTINE GUTREV
*
*****
*          GEANT3 user routine to control tracking of one event
*
*          Called by GRUN
*
*****
*          COMMON/GCFLAG/IDEBUG, IDEMIN, IDEMAX, ITEST, IDRUN, IDEVT, IEORUN
+          , IEOTRI, IEVENT, ISWIT(10), IFINIT(20), NEVENT, NRNDM(2)
COMMON/GCFLAX/BATCH, NOLOG
LOGICAL BATCH, NOLOG
*
-----  

*          character*1,input
CALL GTREVE
        Debug and plot tracks.
*
*          IF(IDEBUG.EQ.1) THEN
*          if(ninter1.gt.0) then
*              IF(ISWIT(2).EQ.1) CALL GPRINT('JXYZ', 0)
*              IF(ISWIT(3).EQ.1) THEN
*                  CALL GDSHOW(1)
*                  CALL GDXYZ (0)
*                  print *, ' print any key to show event'
*                  read (5,'(a1)')
*                  CALL ICLRWK(0,0)
*              ENDIF
*          end if
*      ENDIF
*
        END
CDECK  ID>, UFILES.
        SUBROUTINE UFILES
*****

```

```

*
*          to open files
*
***** ****
*
*          To open FFREAD and HBOOK files
*
CHARACTER*(*) FILNAM, FSTAT
dimension r(2)
PARAMETER (FILNAM='dose.dat')
*
PARAMETER (FSTAT='OLD')
OPEN(UNIT=4,FILE=FILNAM,STATUS=FSTAT,
+      FORM='FORMATTED')
*
*      open postscript file
open(unit = 20,file='dose.ps',form='formatted',status='unknown')
call igmeta(20,-112)
call igrng(20.,15.)
*      open output data file
open(unit=6,File='dose.out',form='formatted',status='unknown')
*          Open a HBOOK direct access file
*
CALL HOPEN(34,'HBOOK','dose.hbook','N',1024,ISTAT)
END
SUBROUTINE UGEOM
*
***** ****
*
*          Routine to define the geometry of the set-up.
*
***** ****
C
COMMON/GCKINE/IKINE,PKINE(10),ITRA,ISTAK,IVERT,IPART,ITRTYP
+      ,NAPART(5),AMASS,CHARGE,TLIFE,VERT(3),PVERT(4),IPAOLD
C
COMMON/GCFLAG/IDEBUG,IDELEM,IDELEM,ITEST,IDRUN,IDEVT,IEORUN
+      ,IEOTRI,IEVENT,ISWIT(10),IFINIT(20),NEVENT,NRNDM(2)
COMMON/GCFLAX/BATCH, NOLOG

```

```

LOGICAL BATCH, NOLOG
C
    common/runpar/iaxis,matcav,igeom
    common/posit/xpos,ypos,zpos,xcut,ycut
    common/phan/iphan,ilung,zphan,rotang
    common/tank/xtank,ytank,ztank
    common/cavi/cavpos,xcav,ycav,zcav
    common/tmedia/fieldp,ifieldp,tmaxfp,dmaxmp,deemap,epsip,stmpip
        character*1,input
* material paramters
* water paramters
    dimension awater(2),zwater(2),wwater(2)
* muscle paramters
    dimension amusc(10),zmusc(10),wmusc(10)
* fat paramters
    dimension afat(5) , zfat(5),wfat(5)
* bone paramters
    dimension abone(8),zbone(8),wbone(8)
* polystrene parmaters
    dimension apoly(2),zpoly(2),wpoly(2)
* parmaters for physical dimensions of objects
    dimension areapr(3),cstlpr(3)
    dimension phanpr(3)
* water phantom par
    dimension watepr(3)
* the back bone paramters
    dimension bonepr(3)
* the water tank parameters
    dimension slabpr(3)
* the davity paramters
    dimension cav1pr(3)
*
*      basic parameters
    data awater/1.01, 16./
    data zwater/1., 8. /
    data wwater/2.,1./
C
* muscle see johns page 720
*
    data amusc/1.008,12.011,14.007,16.994,22.99,24.305,30.974,

```

```

+ 32.066,39.098,40.078/
data zmusc/1.,6.,7.,8.,11.,12.,15.,16.,19.,20./
data wmmusc/.102,.123,.035,.7289,.0008,.0002,.002,
+ .005,.003,.00007/
*
data afat/1.008,12.011,14.007,16.994,32.066/
data zfat/1.,6.,7.,8.,16./
data wfat/.112,.5732,.011,.3031,.00006/
*
data abone/1.008,12.011,14.007,16.994,24.305,30.974,
+ 32.066,40.078/
data zbone/1.,6.,7.,8.,12.,15.,16.,20./
data wbone/.064,.278,.027,.410,.002,.070,.002,.147/
*
data apoly/1.008,12.001/
data zpoly/1.,6./
data wpoly/.0774,.9226/
*
* vacuum parameters
VAC = 10**(-16)
RVAC = 10**16

* scattering area parameters
data areapr/ 40., 40., 40./
data cstlpr/ 25., 20., .625 /
data phanpr/ 15., 11.,15./
data watepr/ 0.,10.7,15./
data bonepr/0.,1.25,15./
data cav1pr/2.5,2.5,15./
* the slab of water
data slabpr/15.,20.,.5/
*
* point source geometry
areapr(1) = xtank
areapr(2) = ytank
areapr(3) = zpos+ztank
slabpr(1) = xtank
slabpr(2) = ytank
slabpr(3) = ztank
cav1pr(1) = xcav

```

```

* BUGS      cav1pr(2) = ycav
            cav1pr(2) = zcav
* BUGS      cav1pr(3) = zcav
            cav1pr(3) = ycav
*
*           defines materials
call gsmate( 1,'air      $', 14.6,7.3,0.0012,30423.0,67500.0,0,0)
call gsmate( 2,'vacum    $', VAC,VAC,VAC,RVAC,0.,0,0)
call gsmate( 3,'aluminum$', 26.98, 13., 2.70, 8.9, 0., 0,0)
call gsmate( 4,'lead     $', 207.19, 82., 11.35, .56, 0., 0, 0)
call gsmixt( 6,'water   $', awater,zwater,1.00,-2,wwater)
call gsmixt( 7,'muscle  $', amusc,zmusc,1.04,10,wmusc)
call gsmixt( 8,'bone    $', abone,zbone,1.65,8,wbone)
call gsmixt( 9,'fat     $', afat ,zfat ,.916,5,wfat )
call gsmixt(11,'polystr $', apoly,zpoly,1.044,2,wpoly)
*
*           defines user tracking media parameters
fieldm = filedpm
ifield = ifieldp
tmaxfd = tmaxfp
dmaxms = dmaxmp
deemax = deemap
epsil = epsip
stmin = stmip
*
*           defines tracking media parameters.
call gstmed( 1, 'air          $ ', 1, 1, ifield , fieldm,tmaxfd,
*                  dmaxms, deemax, epsil, stmin, 0, 0)
call gstmed( 2, 'vacum        $ ', 2, 0, 0, 0., 0., 500., 0.,
*                  500., 500., 0, 0)
call gstmed( 3, 'aluminum $ ', 3, 1, ifield , fieldm,tmaxfd,
*                  dmaxms, deemax, epsil, stmin, 0, 0)
call gstmed( 4, 'lead         $ ', 4, 1, ifield , fieldm,tmaxfd,
*                  dmaxms, deemax, epsil, stmin, 0, 0)
call gstmed( 6, 'water        $ ', 6, 1, ifield , fieldm,tmaxfd,
*                  dmaxms, deemax, epsil, stmin, 0, 0)
call gstmed( 7, 'musc         $ ', 7, 1, ifield , fieldm,tmaxfd,
*                  dmaxms, deemax, epsil, stmin, 0, 0)
call gstmed( 8, 'bone         $ ', 8, 1, ifield , fieldm,tmaxfd,
*                  dmaxms, deemax, epsil, stmin, 0, 0)
call gstmed( 9, 'fat          $ ', 9, 1, ifield , fieldm,tmaxfd,
*                  dmaxms, deemax, epsil, stmin, 0, 0)

```

```

    call gstmed(11, 'polystr      $ ', 11, 1, ifield , fieldm,tmaxfd,
*                      dmaxms, deemax, epsil, stmin, 0, 0)
* define the rotation matrix for the phantom
    xang = 90. + rotang
    yang = 180. + rotang
*    call gsrotm(100,xang,90.,yang,270.,90.,0.)
    call gsrotm(100,xang,0.,yang,0.,90.,90.)
*          defines geometry of the set-up
*          define the overall area
    call gsvolu('area', 'BOX ', 2, areapr, 3, ivolu)
* Cavity in the water tank
    call gsvolu('cav1', 'BOX ',matcav, cavipr ,3, ivolu)
* set defaults for igeom=1
    zphan = 0.
    xcol1 = 0.
    xcstl1 = 0.
    xcol2 = 32.5 - 1.6
    xcstl2 = 32.5 + .625
    zcol2 = zphan
    zcstl2 = zphan
* the water slab
    if(iphan.eq.5) then
* define the rotation angle for the water slab
    xang = 90. + rotang
    zang = rotang
    call gsrotm(102,xang,0.,90.,90.,rotang,0.)
    call gsvolu('slab', 'BOX ', 6, slabpr, 3, ivolu)
* position the water slab
    call gspos('slab',1,'area', 0., 0., 0., 102, 'ONLY')
    call gspos('cav1',1,'slab', 0., 0.,cavpos, 100, 'ONLY')
    end if
*          define geometry optimization
    call gsord('area',3)
*          close geometry banks. mandatory system routine.
    call ggclos
*
*          if(iswit(3).eq.1) then
*              call gdrawc('coll',3,0.0,10.,10.,15.00,15.)
*              print *,'print any key to continue'
*              read (5, '(a1)')

```

```

*      call iclrwk(0,0)
fmag = .15
call gdraw('area',135.,135.,0., 10.,10.,fmag,fmag)
call iclrwk(0,0)
*
* plot a section
call gdrawc('area',1,0.0,10.,10.,.200,.2)
call iclrwk(0,0)
* plot a section
call gdrawc('area',2,0.0,10.,10.,.200,.2)
*      print *,'print any key to continue'
*      read (5, '(a1)')
call iclrwk(0,0)
end if
END
CDECK ID>, UGINIT.
SUBROUTINE UGINIT
*
*****
* To initialise GEANT3 program and read data cards
*
*****
*
PARAMETER (KWBANK=69000,KWWORK=5200)
COMMON/GCBANK/NZEBRA,GVERSN,ZVERSN,IXSTOR,IXDIV,IXCONS,FENDQ(16)
+           ,LMAIN,LR1,WS(KWBANK)
DIMENSION IQ(2),Q(2),LQ(8000),IWS(2)
EQUIVALENCE (Q(1),IQ(1),LQ(9)),(LQ(1),LMAIN),(IWS(1),WS(1))
EQUIVALENCE (JCG,JGSTAT)
COMMON/GCLINK/JDIGI ,JDRAW ,JHEAD ,JHITS ,JKINE ,JMATE ,JPART
+           ,JRDTM ,JRUNG ,JSET  ,JSTAK ,JGSTAT,JTMED ,JTRACK,JVERTX
+           ,JVOLUM,JXYZ  ,JGPAR ,JGPAR2,JSKLT
C
COMMON/GCFLAG/IDEBUG,IDEMIN,IDEMAX,ITEST,IDRUN,IDEVT,IEORUN
+           ,IEOTRI,IEVENT,ISWIT(10),IFINIT(20),NEVENT,NRNDM(2)
COMMON/GCFLAX/BATCH, NOLOG
LOGICAL BATCH, NOLOG
C
COMMON/GCUNIT/LIN,LOUT,NUNITS,LUNITS(5)

```

```

INTEGER LIN,LOUT,NUNITS,LUNITS
COMMON/GCMAIL/CHMAIL
CHARACTER*132 CHMAIL
common/even/nev,ide,ipoint
common/tank/xtank,ytank,ztank
common/xyzv/nbx,nby,nbz,fbinx,fbiny,fbinz
common/xyzdos/xyzdose(90,90,100)
common/count/counter
C
* -----
*          Open user files
CALL UFILES
*      read the run parmeters from file 1
call readin

*          Initialize GEANT
CALL GINIT
*
*          Prints version number
WRITE(LOUT,1000)
*
*          Define a data card 'GAST' to change gas type
*
CALL GFFGO
*
*      number of events and number of events to debug
nevent = nev
idemax = ide
itest = nev/10
*          Initialize GEANT/ZBOOK data structures
CALL GZINIT
*          Initialize drawing package
IF(ISWIT(7).EQ.0)THEN
    CALL GDINIT
ENDIF
*
*          Geometry and materials description.
CALL UGEOM
*          Particle table definition and energy loss initialization.
CALL GPART

```

```

CALL GPHYSI
*
      Create a view bank
      IF(ISWIT(7).EQ.0)CALL VIEWYZ(1)
      CALL UHINIT
*
      1000 FORMAT(/, ' DOSE VERSION 2.00.00 ( 02 December 1999 ) ',/)
*
*Initializing arrays
      do 97 i = 1,nbx
      do 98 j = 1,nby
      do 99 k = 1,nbz
         xyzdose(i,j,k)=0.
99      continue
98      continue
97      continue
*
      counter=0
*
      fbinx=nbx/(2*xtank)
      fbiny=nby/(2*ytank)
      fbinz=nbz/(2*ztank)
*
      END
CDECK  ID>, UGLAST.
      SUBROUTINE UGLAST
*
*****
*
*      Termination routine to print histograms and statistics
*
*****
C
*
-----  

common/source/einc,bin,enflag
common/phan/iphant,ilung,zphan,rotang
common/tank/xtank,ytank,ztank
common/voxel/dx,dy,dz
common/voxel1/dx1,dy1,dz1
common/voxel2/dx2,dy2,dz2
common/voxel3/dx3,dy3,dz3

```

```

common/slice/slipo$,slithk,nx,nz
common/xyzv/nbx,nby,nbz
common/xyzdos/xyzdose(90,90,100)

*
      CALL GLAST
C
*
      Print HBOOK histograms
      CALL HPRINT(0)
C      Save histograms
      call hplot(0,' ',' ',' ',0)
C      Save histograms
      CALL HROUT(0,ICYCLE,' ')
      CALL HREND('HBOOK')
*
      Close GKS display file
      close the postscript files
      call igmeta(0,0)
      call iclwk(2)
      CALL IGEND
      open(unit=43,File='xyzdose',form='formatted',status='unknown')
      write(43,*) nbx, nby, nbz
      do 15 i = 1, 1
         write(43,*) (-xtank+j*(2*xtank/nbx), j=0,nbx)
15    continue
      do 16 i = 1, 1
         write(43,*) (-ytank+j*(2*ytank/nby), j=0,nby)
16    continue
      do 17 i = 1, 1
         write(43,*) (j*(2*ztank/nbz), j=0,nbz)
17    continue
      do 18 k = 1,nbz
         do 19 j = 1,nby
            write(43,*) (xyzdose(i,j,k),i=1,nbx)
19    continue
18    continue
      close(43)
      END
CDECK ID>, UHINIT.
      SUBROUTINE UHINIT
*
*****
```

```

*
*           To book the user's histograms
*
***** ****
C
    common/source/einc,bin,enflag
    common/runpar/iaxis,matcav,geom
    common/phan/iphant,ilung,zphan,rotang
    common/tank/xtank,ytank,ztank
    common/posit/xpos,ypos,zpos,xcut,ycut
    common/cavi/cavpos,xcav,ycav,zcav
*
    emaxp=1.1*einc
    CALL HBOOK1(1,'Bremsstrahlung spectrum$',bin,0.,emaxp,0.)
    END
CDECK  ID>, VIEWYZ.
      SUBROUTINE VIEWYZ (IVIEW)
C.
C. ****
C. *
C. *      Draw full set up in 'view bank' mode.
C. *
C. ****
C.
    Common/runpar/iaxis,matcav,geom
    common/posit/xpos,ypos,zpos,xcut,ycut
    common/phan/iphant,ilung,zphan,rotang
*
    CALL GSATT('*', 'SEEN', 1)
C
C      Create bank for view YZ.
    CALL GDOPEN(IVIEW)
    fmag = .15
C
    if((iaxis.eq.1).or.(iaxis.eq.2))then
    CALL GDRAWC('area',iaxis , 0.0, 10.,10.,fmag,fmag)
    end if
    if(iaxis.eq.3) then
    call gdraw('area',120.,150.,0., 10.,10.,.15,.15)
    end if

```

```

C
    CALL GDCLOS
    END
*
* subroutine readin

C. ****
C. *
C. *      To read in runparams for this run
C. *
C. ****
*
common/source/einc,bin,enflag
common/runpar/iaxis,matcav,igeom
common/posit/xpos,ypos,zpos,xcut,ycut
common/phan/iphant,ilung,zphan,rotang
common/tank/xtank,ytank,ztank
common/cavi/cavpos,xcav,ycav,zcav
common/tumor/itumor,rtumor,xtumor,ytumor,ztumor,tratio
common/even/nev,ide,ipoint
common/tmedia/fieldp,ifieldp,tmaxfp,dmaxmp,deemap,epsip,stmip
common/xyzv/nbx,nby,nbz
*
* data card 1
    open(1,file='runparams',status='OLD')
*
    write(6,*) ''
    write(6,*) 'Parameters for this run:'
    write(6,*) ''
    irunpr = 0
    read(1,*) icard,nev,ide,ipoint
    write(6,*) ' data card ', icard
    write(6,*) ' number of events for this run ', nev
    write(6,*) ' number of events plotted ', ide
    write(6,*) ' point, parallel or pencilsource ', ipoint
    write(6,*) ''
*
* data card 2
    read(1,*) icard, einc, bin, enflag
    write(6,*) ''

```

```

        write(6,*), data card ', icard
        write(6,*), incident energy in Gev for photons = ', einc
        write(6,*), number of bins in energy spectrum = ', bin
*
        write(6,*), atomic number of production target = ', ztar
        write(6,*), energy flag (0 for monoenergetic else Mohan)=',enflag
        write(6,*), '
*
* data card 3
        read(1,*),icard, xtank,ytank,ztank
        write(6,*), '
        write(6,*), data card ', icard
        write(6,*), water tank dimensions'
        write(6,*), x half length = ',xtank
        write(6,*), y half length = ',ytank
        write(6,*), z half length = ',ztank
        write(6,*), '
*
* data card 4
        read(1,*),icard, cavpos,xcav,ycav,zcav
        write(6,*), '
        write(6,*), data card ', icard
        write(6,*), cavity position and cavity half lengths'
        write(6,*), cavity position = ', cavpos
        write(6,*), cavity x half length = ', xcab
        write(6,*), cavity y half length = ', ycab
        write(6,*), cavity z half length = ', zcab
        write(6,*), '
*
* data card 5
        read(1,*),icard,fieldp,ifieldp,tmaxfp,dmaxmp,deemap,epsip,stmip
        write(6,*), '
        write(6,*), data card ', icard
        write(6,*), tracking media parameters '
        write(6,*), fieldm = ', fieldp
        write(6,*), ifield = ', ifieldp
        write(6,*), tmaxfd = ', tmaxfp
        write(6,*), dmaxms = ', dmaxmp
        write(6,*), deemax = ', deemap
        write(6,*), epsil = ', epsip
        write(6,*), stmin = ', stmip
        write(6,*), '

```

```

*
* data card 6
    read(1,*)icard, xpos,ypos,zpos
    write(6,*) ''
    write(6,*) ' data card ', icard
    write(6,*) ' x and y position of the point source ',xpos,ypos
    write(6,*) ''

*
* data card 7
    read(1,*)icard,xcut,ycut
    write(6,*) ''
    write(6,*) ' data card ', icard
    write(6,*) ' +ve x and y acceptance for point source',xcut,ycut
    write(6,*) ''

*
* data card 8
    read(1,*)icard,nbx,nby,nbz
    write(6,*) ''
    write(6,*) ' data card ', icard
    write(6,*) '# of cells along X, Y & Z',nbx,nby,nbz
    write(6,*) ''

*
* data card 10
    read(1,*) icard, matcav
    write(6,*) ''
    write(6,*) ' data card ', icard
    write(6,*) ' idenfification number for material in the cavity '
    write(6,*) ' 1           air      '
    write(6,*) ' 2           NaI      '
    write(6,*) ' 3           Aluminum '
    write(6,*) ' 4           lead     '
    write(6,*) ' 5           glass    '
    write(6,*) ' 6           water   '
    write(6,*) ' 7           muscle   '
    write(6,*) ' 8           bone    '
    write(6,*) ' 9           fat     '
    write(6,*) '10          lucite   '
    write(6,*) '11          polystyrene '
    write(6,*) 'cavity material number used = ', matcav
    write(6,*) ''

```

```

*
* data card 15
    read(1,*) icard, iphan ,ilung,rotang
    write(6,*) ' '
    write(6,*) ' data card ', icard
    write(6,*) ' 5 = water tank '
    write(6,*) 'phantom number = ',iphan
    write(6,*) 'ilung = ', ilung, ' ( 1 for lungs in phantom 4)'
    write(6,*) 'rotation angle = ', rotang
    write(6,*) ' '
*
* data card 20
    read(1,*) icard, iaxis,igeom
    write(6,*) ' '
    write(6,*) ' data card ', icard
    write(6,*) ' 1 = area viewed from positive x axis'
    write(6,*) ' 2 = area viewd from postive y axis'
    write(6,*) ' 3 = isometric view '
    write(6,*) 'axis ',iaxis , ' chosen'
    write(6,*) ' '
*
* data card 21
    read(1,*) icard,itumor,rtumor,xtumor,ytumor,ztumor,tratio
    write(6,*) ' '
    write(6,*) ' data card ', icard
    write(6,*) ' itumor = 1, if tumor is included '
    write(6,*) ' tumor radius ', rtumor
    write(6,*) ' tumor position ', xtumor, ytumor, ztumor
    write(6,*) ' relative strenth of tumor ', tratio
    write(6,*) ' '
    close(1)
    write(6,*) ' '
    write(6,*) 'End of reading run paramters card.'
    write(6,*) ' '
* check that both collimator and simulation are not specified
* simultaneously
    end
*****
*                                         *
*          Varian linac spectra (Mohan)      *

```

```

*
*****
*
* subroutine mohan4(egamma)

dimension area(16),x(17),sumar(16)
dimension rndm(2)

data x/
+ 0.0,0.25,0.5,0.75,1.,1.25,1.5,1.75,2.,2.25,2.5,2.75,3.,3.25,
+ 3.5,3.75,4./

data area/
+ 0.0000273753,0.0446637,0.177792,0.133375,0.132117,0.138924,
+ 0.0855541,0.0646403,0.0614342,0.0418522,0.0345028,0.0173501,
+ 0.0217844,0.0217252,0.0217967,0.00246181/

data sumar/
+ 0.00002738,0.04469112,0.22248290,0.35585757,0.48797445,
+ 0.62689818,0.71245231,0.77709265,0.83852688,0.88037910,
+ 0.91488190,0.93223195,0.95401632,0.97574149,0.99753819,1./

call grndm(rndm,2)

do 10 i = 1,16
    if(rndm(1).le.sumar(i)) then
        egamma = rndm(2)*(x(i+1)-x(i))+x(i)
        egamma = egamma*.001
        return
    end if
10   continue

end
*****
*
* subroutine mohan6(egamma)

dimension area(24),x(25),sumar(24)
dimension rndm(2)

```

```

    data x/
+ 0.0,0.25,0.5,0.75,1,1.25,1.5,1.75,2,2.25,2.5,2.75,
+ 3,3.25,3.5,3.75,4,4.25,4.5,4.75,5,5.25,5.5,5.75,6./

    data area/
+ 0.00102054,0.03217721,0.11450595,0.11450595,0.11020442,
+ 0.10148627,0.10148627,0.06202282,0.05882261,0.04638703,
+ 0.03435115,0.03240995,0.03687929,0.02359230,0.03096995,
+ 0.02428053,0.02209113,0.01280682,0.01039471,0.01193327,
+ 0.00403651,0.00674605,0.00297958,0.00390971/

    data sumar/
+ 0.00102054,0.03319775,0.14770370,0.26220965,0.37241407,
+ 0.47390034,0.57538660,0.63740943,0.69623203,0.74261907,
+ 0.77697021,0.80938016,0.84625944,0.86985175,0.90082169,
+ 0.92510222,0.94719335,0.96000017,0.97039488,0.98232815,
+ 0.98636466,0.99311070,0.99609029,1./

call rndm(rndm,2)

do 10 i = 1,24
  if(rndm(1).le.sumar(i)) then
    egamma = rndm(2)*(x(i+1)-x(i))+x(i)
    egamma = egamma*.001
    return
  end if
10   continue

  end
*****
*
subroutine mohan10(egamma)

dimension area(20),x(21),sumar(20)
dimension rndm(2)

    data x/
+ 0.0,0.5,1,1.5,2,2.5,3,3.5,4,4.5,5,5.5,
+ 6,6.5,7,7.5,8,8.5,9,9.5,10./

```

```

    data area/
+ 0.10898780,0.11349740,0.09533682,0.11917857,0.09407601,
+ 0.09597514,0.06894617,0.05077439,0.04720343,0.04002970,
+ 0.04509900,0.02095725,0.02748013,0.01950877,0.01950877,
+ 0.01103236,0.01103236,0.00733260,0.00358300,0.00046034/

    data sumar/
+ 0.10898780,0.22248520,0.31782202,0.43700059,0.53107660,
+ 0.62705174,0.69599791,0.74677229,0.79397572,0.83400542,
+ 0.87910441,0.90006167,0.92754180,0.94705056,0.96655933,
+ 0.97759169,0.98862406,0.99595666,0.99953966,1./

    call rndm(rndm,2)

    do 10 i = 1,20
        if(rndm(1).le.sumar(i)) then
            egamma = rndm(2)*(x(i+1)-x(i))+x(i)
            egamma = egamma*.001
            return
        end if
10      continue

        end
*****
*
    subroutine mohan15(egamma)

    dimension area(58),x(59),sumar(58)
    dimension rndm(2)

    data x/
+ 0.0,0.25,0.5,0.75,1,1.25,1.5,1.75,2,2.25,2.5,2.75,
+ 3,3.25,3.5,3.75,4,4.25,4.5,4.75,5,5.25,
+ 5.5,5.75,6,6.25,6.5,6.75,7,7.25,7.5,7.75,
+ 8,8.25,8.5,8.75,9,9.25,9.5,9.75,10,10.25,
+ 10.5,10.75,11,11.25,11.5,11.75,12,12.25,12.5,12.75,
+ 13,13.25,13.5,13.75,14,14.25,14.5/

    data area/
+ 0.00279546,0.00330203,0.02583623,0.05108165,0.06093008,

```

```

+ 0.06093008,0.05641301,0.05641301,0.05020961,0.05020961,
+ 0.03801635,0.03801635,0.03533825,0.03533825,0.02552386,
+ 0.02552386,0.02552386,0.02552386,0.01929309,0.01929309,
+ 0.01929309,0.01929309,0.01279252,0.01279252,0.01279252,
+ 0.01279252,0.01279252,0.01279252,0.01279252,0.01484022,
+ 0.01142497,0.01142497,0.01142497,0.00945127,0.00945127,
+ 0.00945127,0.00945127,0.00466090,0.00466090,0.00706059,
+ 0.00706059,0.00489676,0.00489676,0.00401299,0.00401299,
+ 0.00295336,0.00295336,0.00295336,0.00271848,0.00472148,
+ 0.00472148,0.00472148,0.00472148,0.00270465,0.00270465,
+ 0.00100643,0.00100643,0.00028533/

      data summar/
+ 0.00279546,0.00609749,0.03193372,0.08301537,0.14394545,
+ 0.20487552,0.26128853,0.31770153,0.36791114,0.41812074,
+ 0.45613710,0.49415345,0.52949169,0.56482994,0.59035380,
+ 0.61587766,0.64140152,0.66692538,0.68621848,0.70551157,
+ 0.72480466,0.74409775,0.75689027,0.76968279,0.78247531,
+ 0.79526783,0.80806035,0.82085287,0.83364539,0.84848561,
+ 0.85991058,0.87133555,0.88276052,0.89221179,0.90166306,
+ 0.91111432,0.92056559,0.92522649,0.92988739,0.93694798,
+ 0.94400858,0.94890534,0.95380210,0.95781508,0.96182807,
+ 0.96478142,0.96773478,0.97068814,0.97340662,0.97812809,
+ 0.98284957,0.98757104,0.99229252,0.99499717,0.99770182,
+ 0.99870824,0.99971467,1./

      call rndm(rndm,2)

      do 10 i = 1,58
          if(rndm(1).le.sumar(i)) then
              egamma = rndm(2)*(x(i+1)-x(i))+x(i)
              egamma = egamma*.001
              return
          end if
10      continue

      end
*****
*
```

```

subroutine wag18(egamma)

dimension area(90),x(91),sumar(90)
dimension rndm(2)

data x/
+ 0.0,0.2,0.4,0.6,0.8,1,1.2,1.4,1.6,1.8,2,2.2,
+ 2.4,2.6,2.8,3,3.2,3.4,3.6,3.8,4,4.2,4.4,4.6,4.8,5,5.2,
+ 5.4,5.6,5.8,6,6.2,6.4,6.6,6.8,7,7.2,7.4,7.6,7.8,8,8.2,
+ 8.4,8.6,8.8,9,9.2,9.4,9.6,9.8,10,10.2,
+ 10.4,10.6,10.8,11,11.2,11.4,11.6,11.8,12,12.2,
+ 12.4,12.6,12.8,13,13.2,13.4,13.6,13.8,14,14.2,
+ 14.4,14.6,14.8,15,15.2,15.4,15.6,15.8,16,16.2,
+ 16.4,16.6,16.8,17,17.2,17.4,17.6,17.8,18./

data area/
+ 0.00250000,0.00560000,0.00680000,0.00820000,
+ 0.01000000,0.01175000,0.01385000,0.01600000,
+ 0.01825000,0.02075000,0.02290000,0.02510000,
+ 0.02670000,0.02830000,0.02900000,0.02960000,
+ 0.02820000,0.02570000,0.02460000,0.02350000,
+ 0.02310000,0.02150000,0.02130000,0.02110000,
+ 0.02075000,0.02060000,0.02050000,0.02040000,
+ 0.01940000,0.01875000,0.01860000,0.01860000,
+ 0.01825000,0.01670000,0.01650000,0.01640000,
+ 0.01475000,0.01470000,0.01375000,0.01375000,
+ 0.01350000,0.01325000,0.01320000,0.01260000,
+ 0.01190000,0.01180000,0.01060000,0.01050000,
+ 0.00950000,0.00925000,0.00825000,0.00800000,
+ 0.00750000,0.00700000,0.00650000,0.00640000,
+ 0.00625000,0.00580000,0.00560000,0.00550000,
+ 0.00510000,0.00480000,0.00460000,0.00450000,
+ 0.00440000,0.00430000,0.00425000,0.00380000,
+ 0.00370000,0.00330000,0.00330000,0.00310000,
+ 0.00270000,0.00260000,0.00230000,0.00200000,
+ 0.00180000,0.00160000,0.00140000,0.00120000,
+ 0.00100000,0.00090000,0.00080000,0.00070000,
+ 0.00060000,0.00050000,0.00040000,0.00030000,
+ 0.00025000,0.00020000/

```

```

data sumar/
+ 0.00250000,0.00810000,0.01490000,0.02310000,0.03310000,
+ 0.04485000,0.05870000,0.07470000,0.09295000,0.11370000,
+ 0.13660000,0.16170000,0.18840000,0.21670000,0.24570000,
+ 0.27530000,0.30350000,0.32920000,0.35380000,0.37730000,
+ 0.40040000,0.42190000,0.44320000,0.46430000,0.48505000,
+ 0.50565000,0.52615000,0.54655000,0.56595000,0.58470000,
+ 0.60330000,0.62190000,0.64015000,0.65685000,0.67335000,
+ 0.68975000,0.70450000,0.71920000,0.73295000,0.74670000,
+ 0.76020000,0.77345000,0.78665000,0.79925000,0.81115000,
+ 0.82295000,0.83355000,0.84405000,0.85355000,0.86280000,
+ 0.87105000,0.87905000,0.88655000,0.89355000,0.90005000,
+ 0.90645000,0.91270000,0.91850000,0.92410000,0.92960000,
+ 0.93470000,0.93950000,0.94410000,0.94860000,0.95300000,
+ 0.95730000,0.96155000,0.96535000,0.96905000,0.97235000,
+ 0.97565000,0.97875000,0.98145000,0.98405000,0.98635000,
+ 0.98835000,0.99015000,0.99175000,0.99315000,0.99435000,
+ 0.99535000,0.99625000,0.99705000,0.99775000,0.99835000,
+ 0.99885000,0.99925000,0.99955000,0.99980000,1./

call grndm(rndm,2)

do 10 i = 1,90
  if(rndm(1).le.sumar(i)) then
    egamma = rndm(2)*(x(i+1)-x(i))+x(i)
    egamma = egamma*.001
    return
  end if
10   continue

end
*****
*
subroutine mohan24(egamma)

dimension area(48),x(49),sumar(48)
dimension rndm(2)

data x/
+ 0.0,0.5,1,1.5,2,2.5,3,3.5,4,4.5,5,5.5,
```

```

+ 6,6.5,7,7.5,8,8.5,9,9.5,10,10.5,11,11.5,12,12.5,13,
+ 13.5,14,14.5,15,15.5,16,16.5,17,17.5,18,
+ 18.5,19,19.5,20,20.5,21,21.5,22,22.5,23,23.5,24./

data area/
+ 0.03397082,0.03400165,0.04259799,0.05822012,0.06330694,
+ 0.06949286,0.06012567,0.04966026,0.04966026,0.04966026,
+ 0.04012049,0.03495509,0.03495509,0.03122967,0.02335256,
+ 0.02204429,0.02429327,0.02479524,0.02494953,0.01956055,
+ 0.01956055,0.01602799,0.01465543,0.01714823,0.01472746,
+ 0.01472746,0.01051517,0.01015987,0.01060481,0.00849799,
+ 0.00898573,0.00615922,0.00727301,0.00546521,0.00636704,
+ 0.00600969,0.00328375,0.00234633,0.00488280,0.00396287,
+ 0.00204737,0.00497451,0.00361919,0.00297819,0.00100143,
+ 0.00195447,0.00047097,0.00064068/

data sumar/
+ 0.03397082,0.06797246,0.11057045,0.16879057,0.23209751,
+ 0.30159037,0.36171604,0.41137630,0.46103656,0.51069682,
+ 0.55081731,0.58577239,0.62072748,0.65195715,0.67530971,
+ 0.69735400,0.72164727,0.74644251,0.77139204,0.79095259,
+ 0.81051313,0.82654112,0.84119656,0.85834478,0.87307224,
+ 0.88779970,0.89831487,0.90847475,0.91907956,0.92757755,
+ 0.93656328,0.94272249,0.94999550,0.95546071,0.96182775,
+ 0.96783744,0.97112120,0.97346752,0.97835032,0.98231319,
+ 0.98436056,0.98933506,0.99295426,0.99593245,0.99693388,
+ 0.99888835,0.99935932,1./

call grndm(rndm,2)

do 10 i = 1,48
  if(rndm(1).le.sumar(i)) then
    egamma = rndm(2)*(x(i+1)-x(i))+x(i)
    egamma = egamma*.001
    return
  end if
10   continue

end
*****

```

```

*
subroutine moh24(egamma)

dimension fac(47),area(47),fk1(47),x(48),sumar(47)
dimension rndm(2)
  data area/
+   0.0345847,0.0389743,0.0512968,0.0618336,0.0675692,
+ 0.0659506,0.0558597,
+  0.0505348,0.0505348,0.0456809,0.0381988,0.0355707,
+  0.0336752,0.0277717,
+  0.0230982,0.0235768,0.0249765,0.0253104,0.022647,
+ 0.019905,0.0181076,
+  0.0156119,0.0161819,0.0162185,0.0149868,0.0128436,
+ 0.0105196,0.0105652,
+  0.00971961,0.00889581,0.00770583,0.00683439,
+ 0.00648127,0.00602031,
+  0.00629735,0.00472855,0.00286461,0.00367822,
+ 0.00450072,0.00305804,
+  0.00357277,0.00437252,0.00335678,0.00202485,
+ 0.00150398,0.00123407,
+  0.000565614/

  data fk1/
+ 7968.53,28.5789,15.726,48.2961,39.715,-26.227,-23.4748,1.,
+ 1.,-25.7526,-47.5614,1.,-65.9453,-31.1883,-187.786,
+ 109.238,489.42,
+ 1592.25,-45.5881,1.,-69.5456,-178.99,98.5534,-101.486,
+ 1.,-58.3231,-691.454,
+ 552.153,-116.609,503.697,-86.9175,220.574,-135.896,
+ 272.418,-687.502,-90.1243,-262.074,96.8566,-267.057,
+ -128.256,
+ 83.9296,-181.267,-383.265,-124.281,257.781,-165.604,
+ 1447.56/

  data fac/
+ 550.429,0.977682,-0.136615,3.72265,
+ 2.61702,-6.70938,-6.37259,-3.89226,-4.39226,-7.6028,-9.38358,
+ -5.92416,-11.1914,-8.9823,-16.425,-3.09904,15.698,
+ 71.3512,-11.8149,-9.95756,-13.2686,-16.8387,-8.56044,
+ -15.5419,-12.468,-14.7482,-28.2976,-2.58281,-17.0168,
```

```

+ -6.28841,-17.0895,-13.235,-18.5116,-13.9699,-26.4089,
+ -19.1023,-20.2515,-18.5375,-22.1539,-21.0344,-20.1503,
+ -22.8352,-24.3231,-22.7533,-21.9746,-23.6587,-22.1125/

    data x/
+ 0.5,1.,1.5,2.,2.5,3.,3.5,4.,4.5,5.,5.5,6.,6.5,7.,7.5,
+ 8.,8.5,9.,9.5,10.,10.5,
+ 11.,11.5,12.,12.5,13.,13.5,14.,14.5,15.,15.5,16.,
+ 16.5,17.,17.5,18.,18.5,19.,
+ 19.5,20.,20.5,21.,21.5,22.,22.5,23.,23.5,24./

    data summar/
+ 0.0345847,0.073559,0.124856,0.186689,0.254259,0.320209,
+ 0.376069,0.426604,
+ 0.477139,0.522819,0.561018,0.596589,0.630264,0.658036,0.681134,
+ 0.704711,
+ 0.729687,0.754998,0.777645,0.79755,0.815657,0.831269,0.847451,
+ 0.86367,
+ 0.878656,0.8915,0.90202,0.912585,0.922304,0.9312,0.938906,
+ 0.94574,0.952222,
+ 0.958242,0.964539,0.969268,0.972132,0.975811,0.980311,
+ 0.983369,0.986942,
+ 0.991315,0.994671,0.996696,0.9982,0.999434,1./

call grndm(rndm,2)

do 10 i = 1,47

if(rndm(1).le.sumar(i)) then
if(fk1(i).ne.1.)then
si = 1.
s = sign(si,fk1(i))
egamma = -fac(i) + s *sqrt( (fac(i) + x(i))**2 +
+ 2.*fk1(i)*area(i)*rndm(2) )
egamma = egamma*.001
return
else
egamma = (x(i) + .5*rndm(2))* .001
return
end if

```

```

        end if
10      continue

        end
*****
*
SUBROUTINE GTGAMA
C.
C. ****
C. *
C. * Photon track. Computes step size and propagates particle *
C. * through step. *
C. *
C. * ==>Called by : GTRACK *
C. * Authors R.Brun, F.Bruyant L.Urban ****
C. *
C. ****
C. *
PARAMETER (KWBANK=69000,KWWORK=5200)
COMMON/GCBANK/NZEBRA,GVERSN,ZVERSN,IXSTOR,IXDIV,IXCONS,FENDQ(16)
+           ,LMAIN,LR1,WS(KWBANK)
DIMENSION IQ(2),Q(2),LQ(8000),IWS(2)
EQUIVALENCE (Q(1),IQ(1),LQ(9)),(LQ(1),LMAIN),(IWS(1),WS(1))
EQUIVALENCE (JCG,JGSTAT)
COMMON/GCLINK/JDIGI ,JDRAW ,JHEAD ,JHITS ,JKINE ,JMATE ,JPART
+           ,JROTM ,JRUNG ,JSET ,JSTAK ,JGSTAT,JTMED ,JTRACK,JVERTX
+           ,JVOLUM,JXYZ ,JGPAR ,JGPAR2,JSKLT
C
COMMON/GCCUTS/CUTGAM,CUTELE,CUTNEU,CUTHAD,CUTMUO,BCUTE,BCUTM
+           ,DCUTE ,DCUTM ,PPCUTM,TOFMAX,GCUTS(5)
C
COMMON/GCJLOC/NJLOC(2),JTM,JMA,JLOSS,JPROB,JMIXT,JPHOT,JANNI
+           ,JCOMP ,JBREM,JPAIR,JDRAY,JPFIS,JMUNU,JRAYL
+           ,JMULOF,JCOEF,JRANG
C
INTEGER      NJLOC   ,JTM,JMA,JLOSS,JPROB,JMIXT,JPHOT,JANNI
+           ,JCOMP ,JBREM,JPAIR,JDRAY,JPFIS,JMUNU,JRAYL
+           ,JMULOF,JCOEF,JRANG
C
COMMON/GCJLCK/NJLCK(2),JTCKOV,JABSCO,JEFFIC,JINDEX,JCURIN

```

```

+ ,JPOLAR,JTSTRA,JTSTCO,JTSTEN,JTASHO
C
C EQUIVALENCE (JLASTV,JTSTEN)
C
C INTEGER NJLCK,JTCKOV,JABSCO,JEFFIC,JINDEX,JCURIN
+ ,JPOLAR,JLASTV,JTSTRA,JTSTCO,JTSTEN
+ ,JTASHO
C
C DOUBLE PRECISION PI,TWOPI,PIBY2,DEGRAD,RADDEG,CLIGHT,BIG,EMASS
C DOUBLE PRECISION EMMU,PMASS,AVO
*
PARAMETER (PI=3.14159265358979324D0)
PARAMETER (TWOPI=6.28318530717958648D0)
PARAMETER (PIBY2=1.57079632679489662D0)
PARAMETER (DEGRAD=0.0174532925199432958D0)
PARAMETER (RADDEG=57.2957795130823209D0)
PARAMETER (CLIGHT=29979245800.D0)
PARAMETER (BIG=10000000000.D0)
PARAMETER (EMASS=0.0005109990615D0)
PARAMETER (EMMU=0.105658387D0)
PARAMETER (PMASS=0.9382723128D0)
PARAMETER (AVO=0.60221367D0)
*
COMMON/GCPHYS/IPAIR,SPAIR,SLPAIR,ZINTPA,STEPPA
+ ,ICOMP,SCOMP,SLCOMP,ZINTCO,STEPCO
+ ,IPHOT,SPHOT,SLPHOT,ZINTPH,STEPPH
+ ,IPFIS,SPFIS,SLPFIS,ZINTPF,STEPPF
+ ,IDRAY,SDRAY,SLDRAY,ZINTDR,STEPDR
+ ,IANNI,SANNI,SLANNI,ZINTAN,STEPAN
+ ,IBREM,SBREM,SLBREM,ZINTBR,STEPBR
+ ,IHADR,SHADR,SLHADR,ZINTHA,STEPHA
+ ,IMUNU,SMUNU,SLMUNU,ZINTMU,STEPMU
+ ,IDCAY,SDCAY,SLIFE ,SUMLIF,DPHYS1
+ ,ILOSS,SLOSS,SOLOSS,STLOSS,DPHYS2
+ ,IMULS,SMULS,SOMULS,STMULS,DPHYS3
+ ,IRAYL,SRAYL,SLRAYL,ZINTRAL,STEPRA
COMMON/GCPHLT/ILABS,SLABS,SLLABS,ZINTLA,STEPLA
+ ,ISYNC
+ ,ISTR
*
```

```

PARAMETER (NWSTAK=12,NWINT=11,NWREAL=12,NWTRAC=NWINT+NWREAL+5)
COMMON /GCSTAK/ NJTMAX, NJTMIN, NTSTKP, NTSTKS, NDBOOK, NDPUSH,
+           NJFREE, NJGARB, NJINVO, LINSAV(15), LMXSAV(15)
EQUIVALENCE (ISTORD,NJTMIN)

C
COMMON/GCTMED/NUMED,NATMED(5),ISVOL,IFIELD,FIELDM,TMAXFD,STEMAX
+           ,DEEMAX,EPSIL,STMIN,CFIELD,PREC,IUPD,ISTPAR,NUMOLD
COMMON/GCTLIT/THRIND,PMIN,DP,DNDL,JMIN,ITCKOV,IMCKOV,NPCKOV

C
COMMON/GCMULO/SINMUL(101),COSMUL(101),SQRMUL(101),OMCMOL,CHCMOL
+           ,EKMIN,EKMAX,NEKBIN,NEK1,EKINV,GEKA,GEKB,EKBIN(200),ELOW(200)

C
REAL SINMUL,COSMUL,SQRMUL,OMCMOL,CHCMOL,EKMIN,EKMAX,ELOW,EKINV
REAL GEKA,GEKB,EKBIN
INTEGER NEKBIN,NEK1

C
PARAMETER (MAXMEC=30)
COMMON/GCTRACK/VECT(7),GETOT,GEKIN,VOUT(7),NMEC,LMEC(MAXMEC)
+           ,NAMEC(MAXMEC),NSTEP,MAXNST,DESTEP,DESTEL,SAFETY,SLENG
+           ,STEP,SNEXT,SFIELD,TOFG,GEKRAT,UPWGHT,IGNEXT,INWVOL
+           ,ISTOP,IGAUTO,IEKBIN,ILOSL,IMULL,INGOTO,NLDOWN,NLEVIN
+           ,NLVS,ISTORY
PARAMETER (MAXME1=30)
COMMON/GCTPOL/POLAR(3),NAMEC1(MAXME1)

C
PARAMETER (EPSMAC=1.E-6)
DOUBLE PRECISION ONE,XCOEF1,XCOEF2,XCOEF3,ZERO
PARAMETER (ONE=1,ZERO=0)
PARAMETER (EPCUT=1.022E-3)

C.
C. -----
*
* *** Particle below energy threshold ? Short circuit
*
*
*           IF (GEKIN.LE.CUTGAM) GOTO 998
*
* *** Update local pointers if medium has changed
*
*           IF(IUPD.EQ.0)THEN

```

```

IUPD = 1
JPHTOT = LQ(JMA-6)
JCOMP = LQ(JMA-8)
JPAIR = LQ(JMA-10)
JPFIS = LQ(JMA-12)
JRAYL = LQ(JMA-13)
ENDIF
*
* *** Compute current step size
*
IPROC = 103
STEP = STEMAX
GEKRT1 = 1 .-GEKRAT
*
* ** Step limitation due to pair devuction ?
*
IF (GETOT.GT.EPCUT) THEN
  IF (IPAIR.GT.0) THEN
    STEPPA = GEKRT1*Q(JPAIR+IEKBIN) +GEKRAT*Q(JPAIR+IEKBIN+1)
    SPAIR = STEPPA*ZINTPA
    IF (SPAIR.LT.STEP) THEN
      STEP = SPAIR
      IPROC = 6
    ENDIF
  ENDIF
ENDIF
*
* ** Step limitation due to Compton scattering ?
*
IF (ICOMP.GT.0) THEN
  STEPCO = GEKRT1*Q(JCOMP+IEKBIN) +GEKRAT*Q(JCOMP+IEKBIN+1)
  SCOMP = STEPCO*ZINTCO
  IF (SCOMP.LT.STEP) THEN
    STEP = SCOMP
    IPROC = 7
  ENDIF
ENDIF
*
* ** Step limitation due to photo-electric effect ?
*

```

```

IF (GEKIN.LT.0.4) THEN
  IF (IPHOT.GT.0) THEN
    STEPPH = GEKRT1*Q(JPHOT+IEKBIN) +GEKRAT*Q(JPHOT+IEKBIN+1)
    SPHOT  = STEPPH*ZINTPH
    IF (SPHOT.LT.STEP) THEN
      STEP  = SPHOT
      IPROC = 8
    ENDIF
  ENDIF
ENDIF
*
*  ** Step limitation due to photo-fission ?
*
IF (JPFIS.GT.0) THEN
  STEPPF = GEKRT1*Q(JPFIS+IEKBIN) +GEKRAT*Q(JPFIS+IEKBIN+1)
  SPFIS  = STEPPF*ZINTPF
  IF (SPFIS.LT.STEP) THEN
    STEP  = SPFIS
    IPROC = 23
  ENDIF
ENDIF
*
*  ** Step limitation due to Rayleigh scattering ?
*
IF (IRAYL.GT.0) THEN
  IF (GEKIN.LT.0.01) THEN
    STEPRA = GEKRT1*Q(JRAYL+IEKBIN) +GEKRAT*Q(JRAYL+IEKBIN+1)
    SRAYL  = STEPRA*ZINTR
    IF (SRAYL.LT.STEP) THEN
      STEP  = SRAYL
      IPROC = 25
    ENDIF
  ENDIF
ENDIF
*
IF (STEP.LT.0.) STEP = 0.
*
*  ** Step limitation due to geometry ?
*
IF (STEP.GE.SAFETY) THEN

```

```

CALL GTNEXT
IF (IGNEXT.NE.0) THEN
    STEP = SNEXT + PREC
    INWVOL= 2
    IPROC = 0
    NMEC = 1
    LMEC(1)=1
ENDIF
*
*      Update SAFETY in stack companions, if any
IF (IQ(JSTAK+3).NE.0) THEN
    DO 10 IST = IQ(JSTAK+3),IQ(JSTAK+1)
        JST = JSTAK +3 +(IST-1)*NWSTAK
        Q(JST+11) = SAFETY
10     CONTINUE
        IQ(JSTAK+3) = 0
ENDIF
*
ELSE
    IQ(JSTAK+3) = 0
ENDIF
*
* *** Linear transport
*
IF (INWVOL.EQ.2) THEN
    DO 20 I = 1,3
        VECTMP = VECT(I) +STEP*VECT(I+3)
        IF(VECTMP.EQ.VECT(I)) THEN
*
* *** Correct for machine precision
*
        IF(VECT(I+3).NE.0.) THEN
            VECTMP = VECT(I)+ABS(VECT(I))*SIGN(1.,VECT(I+3))*
+
            EPSMAC
            IF(NMEC.GT.0) THEN
                IF(LMEC(NMEC).EQ.104) NMEC=NMEC-1
            ENDIF
            NMEC=NMEC+1
            LMEC(NMEC)=104
        ENDIF
    ENDIF

```

```

        ENDIF
        VECT(I) = VECTMP
20     CONTINUE
        ELSE
            DO 30 I = 1,3
                VECT(I) = VECT(I) +STEP*VECT(I+3)
30     CONTINUE
        ENDIF
*
*           SLENG = SLENG +STEP
*
* *** Update time of flight
*
*           TOFG = TOFG +STEP/CLIGHT
*
* *** Update interaction probabilities
*
        IF (GETOT.GT.EPCUT) THEN
            IF (IPAIR.GT.0) ZINTPA = ZINTPA -STEP/STEPPA
        ENDIF
        IF (ICOMP.GT.0)      ZINTCO = ZINTCO -STEP/STEPCO
        IF (GEKIN.LT.0.4) THEN
            IF (IPHOT.GT.0) ZINTPH = ZINTPH -STEP/STEPH
        ENDIF
        IF (JPFIS.GT.0)      ZINTPF = ZINTPF -STEP/STEPF
        IF (IRAYL.GT.0) THEN
            IF (GEKIN.LT.0.01) ZINTRA = ZINTRA -STEP/STEPRA
        ENDIF
*
        IF (IPROC.EQ.0) GO TO 999
        NMEC = 1
        LMEC(1) = IPROC
*
*   ** Pair devuction ?
*
        IF (IPROC.EQ.6) THEN
            CALL GPAIRG
*
*   ** Compton scattering ?
*

```

```

ELSE IF (IPROC.EQ.7) THEN
    CALL GCOMP
*
*  ** Photo-electric effect ?
*
        ELSE IF (IPROC.EQ.8) THEN
*      Calculate range of the photoelectron ( with kin. energy Ephot)
*
CDA    IF(GEKIN.LE.0.001)  THEN
        IF(GEKIN.LE.0.00001)  THEN
            JCOEF = LQ(JMA-17)
            IF(GEKRAT.LT.0.7) THEN
                I1 = MAX(IEKBIN-1,1)
            ELSE
                I1 = MIN(IEKBIN,NEKBIN-1)
            ENDIF
            I1 = 3*(I1-1)+1
            XCOEF1 = Q(JCOEF+I1)
            XCOEF2 = Q(JCOEF+I1+1)
            XCOEF3 = Q(JCOEF+I1+2)
            IF(XCOEF1.NE.0.) THEN
                STOPMX = -XCOEF2+SIGN(ONE,XCOEF1)*SQRT(XCOEF2**2 - (XCOEF3-
+               GEKIN/XCOEF1))
            ELSE
                STOPMX = - (XCOEF3-GEKIN)/XCOEF2
            ENDIF
*
*      DO NOT call GPHOT if this (overestimated) range is smaller
*      than SAFETY
*
        IF (STOPMX.LE.SAFETY) GOTO 998
    ENDIF

        CALL GPHOT
*
*  ** Rayleigh effect ?
*
        ELSE IF (IPROC.EQ.25) THEN
            CALL GRAYL
*

```

```
*  ** Photo-fission ?  
*  
*      ELSE IF (IPROC.EQ.23) THEN  
*          CALL GPFIS  
*  
*      ENDIF  
*  
*      GOTO 999  
998      DESTEP = GEKIN  
*998      continue  
        GEKIN  = 0.  
        GETOT  = 0.  
        VECT(7)= 0.  
        ISTOP   = 2  
        NMEC    = 1  
        LMEC(1)= 30  
999 END
```

```
*****
```